



STRUCTURAL AND OPTICAL STUDIES

*Of*

CERIUM DOPED LEAD TUNGSTATE NANO PHOSPHOR

A THESIS

*Submitted by*

DHARMENDRA V. TAWDE

*For the award of the degree*

*Of*

DOCTOR OF PHILOSOPHY

*Under the guidance of*

Dr. M.SRINIVAS

PHYSICS DEPARTMENT, FACULTY OF SCIENCE

THE MAHARAJA SAYAJIRAO UNIVERSITY OF BARODA

OCTOBER 2012

## Chapter 1

# Introduction

## Chapter 2

### Experimental Technique

### Hydrothermal Method

## Chapter 3

### Structural Studies

# X-ray Diffraction Analysis

Chapter 4

Structural Studies

Transmission Electron Microscopy

&

Scanning Electron Microscopy

Chapter 5

Optical Studies

**Photoluminescence Analysis**

## Chapter 6

# Summary & Conclusions

## DECLARATION

I hereby declare that the research work presented in this thesis entitled “**Structural And Optical Studies of Cerium Doped Lead Tungstate Nano Phosphor**” is original and carried out by me under the supervision and guidance of **Dr.M.Srinivas**, Associate Professor, Department of Physics, The Maharaja Sayajirao University of Baroda, Vadodara, for the award of the degree of *Doctor of Philosophy*.

The work has not been submitted in part or in full to any other University or Organization for the award of any degree or diploma.

**Dharmendra V.Tawde**

**(Ph.D. student)**

## CERTIFICATE

This is to certify that the thesis entitled “**Structural And Optical Studies of Cerium Doped Lead Tungstate Nano Phosphor**” that is being submitted by **Mr. Dharmendra V. Tawde** in partial fulfillment for the award of *Doctor of Philosophy* in Physics to the The Maharaja Sayajirao University of Baroda, Vadodara is a record of bonafide work carried out by him under my guidance and supervision.

The work presented in the thesis is original work of the candidate and is worth consideration for the award of above said degree. The results embodied in this thesis have not been submitted to any other University or Institute for the award of any degree or diploma.

### **Signature of Supervisor**

**Dr. M. Srinivas**

Associate Professor,

Physics Department,

Faculty of Science,

The Maharaja Sayajirao University of Baroda,

Vadodara, Gujarat, India.

## CERTIFICATE

This is to certify that the thesis entitled “**Structural And Optical Studies of Cerium Doped Lead Tungstate Nano Phosphor**” that is being submitted by **Mr. Dharmendra V. Tawde** in partial fulfilment for the award of *Doctor of Philosophy* in Physics to the The Maharaja Sayajirao University of Baroda, Vadodara is a record of bonafide work carried out by him in Physics Department, The Maharaja Sayajirao University of Baroda.

The work presented in the thesis is original work of the candidate and is worth consideration for the award of above said degree. The results embodied in this thesis have not been submitted to any other University or Institute for the award of any degree or diploma.

### **Signature of Head of Institution**

**Prof. A. C. Sharma**

Professor & Head,

Physics Department,

Faculty of Science,

The Maharaja Sayajirao University of Baroda,

Vadodara, Gujarat, India.

*Dedicated*

*to*

**My God, Family & Teachers**

Without their blessing, love and encouragement this could not be possible.....

## ACKNOWLEDGEMENTS

First and foremost I offer my sincerest gratitude to my Ph.D. supervisor, Dr. M. Srinivas, Physics Department, The M. S. University of Baroda, who has supported/ guided me throughout my Ph.D. work with his patience, sympathetic and encouraging attitude whilst allowing me to work in my own way.

It gives me great pleasure in expressing my indebtedness and deep sense of gratitude to Dr. K.V.R. Murthy, Applied Physics Department, Faculty of Technology, The M.S.University of Baroda. I have immensely benefited from the discussion with him and his critical evaluations for which I shall always be obliged to him.

My warm and grateful acknowledgements are extended to Prof. A. C. Sharma, Professor & Head of Physics Department, The M.S.University of Baroda, for his valuable support and cooperation.

I am grateful to University Grants Commission, New Delhi, India for the award of 'Research Fellowship in Sciences for Meritorious Students' and UGC-CSR, Indore Center for providing XRD and TEM characterization facilities.

I am also grateful to The Maharaja Sayajirao University of Baroda for providing me infrastructure and research facility.

I express my sincere obligations to the entire teaching and nonteaching staff of Physics Department for providing me an affable and healthy atmosphere during my Ph.D. work at the department.

I also put on record my thankfulness to my colleagues Manish Jayswal, Devang Shah, Sagar Ambawle, Naveen Agrawal, Poonam Sharma, Chaitali Gavade Sangeetha, Digish Patel, Dhaval Modi and others for their immense support and sharing knowledge during my work.

I am extremely thankful to my colleagues from Chemistry department Harishbhai, Akilbhai, Nilesh Patel who helped me since starting of my Ph.D.

Lastly, and most importantly, I wish to thank my loving parents. Of course, I would not be who I am, without the love and support I have received from my family members. Their endless love, priceless perpetual, indispensable help, support and everything made all this possible.

Words fail me to express my appreciation for my wife Deepika, whose dedication, love and persistent confidence in me, have taken the load off my shoulder.

Above all, I express my profound gratitude to the almighty God for all His grace and light, which gave strength as well as inspired me throughout the work. Finally, I express my thanks, and I apologize, to anybody that provided any help to me and I could not remember at this moment.

Dharmendra V. Tawde

30<sup>th</sup> September 2012

## ABSTRACT

The controlled synthesis of inorganic nano- and microcrystals with specific size, shape and structure is of fundamental significance in modern material science and engineering because it could determine not only the relevant optical, electronic and magnetic properties of the material but also the performances of those material-based devices for applications. Recently, many efforts have been made to synthesize tungstate crystals with controlled morphologies because of their excellent luminescent properties and promising applications. Out of all tungstate,  $\text{PbWO}_4$  is the most attractive for high-energy physics applications because of its high density ( $8.3 \text{ g/cm}^3$ ), short decay time (less than 10 ns for the most part of light output), high-irradiation damage resistance ( $10^7$  rad for undoped and  $10^8$  rad for La-doped  $\text{PbWO}_4$ ), small molierie radius, fast decay time, non-hygroscopicity.  $\text{PbWO}_4$  become a subject of renewed interest about 15 years ago when its favourable characteristics as scintillation detector was reported. Though  $\text{PbWO}_4$  has low light yield (100 time smaller than  $\text{CaWO}_4$ ), it has very short decay time (ns) makes it strongest candidate for scintillation detector.

In the present work, we have reported a facile, an economical and green chemical route to synthesis  $\text{PbWO}_4$ . We have prepared undoped as well as Cerium doped  $\text{PbWO}_4$  phosphor with various morphologies using Low Temperature Hydrothermal method. We have divided our experiment in to two parts. In the first part of our experiment undoped as well as Cerium doped  $\text{PbWO}_4$  crystals were synthesized with different Lead sources (Lead Acetate, Lead Nitrate and Lead Chloride),  $\text{Na}_2\text{WO}_4$  as a metallic cation and distilled water as solvent. In the second part of our experiment  $\text{PbCl}_2$  was kept constant as a Lead source and undoped as well

as Cerium doped  $\text{PbWO}_4$  crystals were produced by varying reaction temperatures and pH of solution.

We have designed a Teflon lined stainless steel autoclave having 90ml capacity used to synthesize all  $\text{PbWO}_4$  samples. Powder X-ray diffraction (XRD) was performed to identify crystal structure and phase produced. Calculation of lattice parameters, unit cell volume and average crystallite size were performed for all  $\text{PbWO}_4$  samples using PowderX program. Structural studies of  $\text{PbWO}_4$  and  $\text{PbWO}_4$ :Ce sample reveals that all prepared samples are polycrystalline in nature and contains two phases of  $\text{PbWO}_4$ : stolzite and raspite. All X-ray diffraction peaks were indexed to a tetragonal stolzite phase with space group  $I4_1/a$  and monoclinic raspite phase with space group  $P2_1/a$ . At low temperature raspite phase is produced predominantly and with increase in temperature it transforms irreversibly into stolzite phase.

Cerium doping at different temperatures does not change the crystal structure of  $\text{PbWO}_4$  or induce a new phase. Cerium also acts as catalyst and helps raspite phase to convert into stolzite phase when Lead Chloride was used as Lead source. Cerium doping reduce the crystallite size in the case of  $\text{Pb}(\text{CH}_3\text{COO})_2$  or  $\text{Pb}(\text{NO}_3)_2$  while it is increased in the case of  $\text{PbCl}_2$  as a Lead source. Cerium increases the average crystallite size for more than 50% at all the temperatures. Lead Chloride proved to be better Lead source to produce high crystalline  $\text{PbWO}_4$  crystals over Lead Nitrate and Lead Acetate.

In order to study morphology, samples were characterized with Field Effect Scanning Electron Microscopy (FESEM) and Transmission Electron Microscopy (TEM). SEM and TEM images reveal that prepared samples have micrometer to nanometer in size and with different morphology such as single or multi branched dendrite (1-2  $\mu\text{m}$ ), bipyramidal octahedral microcrystals (1.5 $\mu\text{m}$ ), one dimensional

nanobelts 5 $\mu$ m x 1 $\mu$ m, nanoplates few  $\mu$ m, Spherical Hollow Nanoparticles (HNPs) (20-40 nm), Hollow Nano Tubes (HNTs) (12.37 nm x 80-170 nm) and nanorods (40nm x 2 $\mu$ m).

The photoluminescence (PL) of the samples was investigated using Spectrofluorophotometer at room temperature with 254 nm, 300 nm and 625 nm excitation wavelengths. Effect of different reaction parameters on PL emission was investigated. The shape of PL spectra of PbWO<sub>4</sub> synthesised using PbCl<sub>2</sub> has “*spread-eagle-shape*” with a central peak surrounded by two broad shoulder peaks. Emission spectrum reveals that it is composed of several sub-bands which are almost distributed throughout entire 350-550 nm region. PL emission spectra of PbWO<sub>4</sub> consists two components, a fast blue component around 450 nm which is an intrinsic feature of scheelite phase and a slow green one around 480– 520 nm which is an intrinsic feature of raspite phase. The emission spectra in blue range are occurring due to radiative transition of [WO<sub>4</sub><sup>2-</sup>] complex. The cerium-doped samples show weaker luminescence intensity than that of undoped samples. The reduction in PL intensity is due to the nonradiative *5d-4f* transition of the excited Ce<sup>3+</sup>. The green emission of undoped crystals was ascribed to the WO<sub>3</sub> oxygen-deficient complex anion in scheelite phase. The decomposition of PL spectra into individual Gaussian components results four Gaussians to achieve a good agreement with the experimental data. The presence of four Gaussian components indicates the excited states of emission center are relaxed and degenerated under the influence by some type of perturbation. We proposed that the Gaussian peak I (367 nm), the Gaussian peak II (392 nm) and the Gaussian peak III (452 nm) may correspond to the radiative transitions from <sup>3</sup>A<sub>1</sub> → <sup>1</sup>A<sub>1</sub>, <sup>3</sup>A<sub>2</sub> ≅ <sup>3</sup>E → <sup>1</sup>A<sub>1</sub> and <sup>3</sup>A<sub>2</sub> → <sup>1</sup>A<sub>1</sub>, respectively. Hence blue emission occurs from the lower lying triplet state split by Jahn-Teller interaction.

Cerium doped  $\text{PbWO}_4$  prepared at  $200^\circ\text{C}$  is enhance the green luminescence and give some contributions to the “slow” decay components which may be negative to the scintillating properties not preferable to use for scintillation detector purpose. PL intensity has direct relation with crystallinity. The better crystallinity, the higher PL emission peak is. PL spectra of nano-sized  $\text{PbWO}_4$  crystallites are strongly relied on their particle size and crystallinity. The PL intensity of blue emission peak is highest for sample prepared at 7pH (HNTs), it is intermediate for sample prepared at 11pH (Nanorods) and lowest for sample prepared at 3pH which indicates that  $\text{PbWO}_4$  HNTs have more regular lattice structure and uniform morphology compared to Nanorods. Sample prepared at 3pH has lowest regular lattice structure. We have proposed possible applications of  $\text{PbWO}_4$  nano phosphor as Green Emitting Lamp Phosphor, HNTs as Nano Fluidic devices in medical diaganosis.

# TABLE OF CONTENTS

<b>LIST OF TABLES</b> .....	v
<b>LIST OF FIGURES</b> .....	vii

## **Chapter 1 INTRODUCTION**

1.1 Tungstate – a general background.....	1
1.2 Lead Tungstate – PbWO <sub>4</sub> .....	4
1.3 History of synthesis.....	5
1.4 Crystal structure of PbWO <sub>4</sub> .....	9
1.4.1 Scheelite.....	9
1.4.2 Rospite.....	10
1.5 Doping with trivalent rare earth ions (RE <sup>3+</sup> ).....	11
1.5.1 Cerium.....	12
References.....	15

## **Chapter 2 EXPERIMENTAL TECHNIQUE: HYDROTHERMAL METHOD**

2.1 History.....	18
2.2 Definitions.....	19
2.3 Water as a Reaction Medium .....	20
2.4 Merits of Hydrothermal Synthesis.....	24
2.5 Autoclave.....	26
2.6 Liners.....	27
2.7 Effect of Hydrogen on Autoclave.....	29
2.7.1 Hydrogen embrittlement.....	29
2.8 Synthesis.....	30
2.8.1 Reagents and Solvents.....	30
2.8.2 Procedure.....	30
2.9 Summary of prepared samples.....	32
2.10 Characterization.....	34
References.....	35

## **Chapter 3 STRUCTURAL STUDIES: X-RAY DIFFRACTION ANALYSIS**

3.1 X-ray Diffraction Analysis (XRD).....	36
3.1.1 Introduction.....	36
3.1.2 X-ray source.....	37
3.1.3 Geometry of X-ray Diffractometer.....	37
3.1.4 Examination of X-ray diffraction pattern.....	38
3.2 Characterization.....	40
3.2.1 Instruments used to record X-ray spectra.....	40
3.2.2 Analysis of XRD data.....	42
3.2.3 Procedure to analysis XRD data with PowderX Program.....	42
3.3 X-ray diffraction analysis of PbWO <sub>4</sub> .....	43
3.3.1 Introduction.....	43
3.3.2 Literature survey.....	44
3.3.3 Synthesis of PbWO <sub>4</sub> with different Lead Sources.....	45
3.3.4 Effect of Lead Sources.....	49
3.4 Lead Chloride as a Lead Source.....	53
3.4.1 Reaction parameters.....	53
3.5 Effect of pH of reaction solution on PbWO <sub>4</sub> .....	55
3.6 Effect of synthesis Temperature on PbWO <sub>4</sub> .....	60
3.7 Effect of synthesis Temperature on PbWO <sub>4</sub> :Ce.....	66
3.8 Effect of Cerium doping on structural properties of PbWO <sub>4</sub> .....	73
References.....	79

## **Chapter 4 STRUCTURAL STUDIES: TEM & SEM**

4.1 Characterization Techniques.....	82
4.1.1 Transmission Electron Microscopy (TEM).....	82
4.1.2 Scanning Electron Microscopy (SEM).....	83
4.2 Introduction.....	85
4.3 Effect of Lead Source on Morphology of PbWO <sub>4</sub> .....	87
4.4 PbWO <sub>4</sub> prepared with Lead Acetate.....	88
4.4.1 Tetrahedron shaped microparticles of PbWO <sub>4</sub> .....	88
4.5 PbWO <sub>4</sub> : Ce prepared with Lead Acetate.....	90
4.5.1 Raspite Phase .....	92

4.5.2 Growth Mechanism of PbWO <sub>4</sub> microbelt.....	93
4.6 PbWO <sub>4</sub> prepared with Lead Nitrate.....	95
4.6.1 Explanation of formation of PbWO <sub>4</sub> 3-Dimensional dendrite.....	96
4.6.2 Explanation of formation of rhombic shaped PbWO <sub>4</sub> particles.....	97
4.7 PbWO <sub>4</sub> :Ce prepared with Lead Nitrate.....	100
4.8 PbWO <sub>4</sub> prepared with Lead Chloride.....	102
4.9 PbWO <sub>4</sub> :Ce prepared with Lead Chloride.....	103
4.10 Effect of reaction parameter on the morphology.....	106
4.11 Effect of pH of reaction solution on morphology of PbWO <sub>4</sub> .....	107
4.11.1 Formation Mechanism of Hollow Nanostructures of PbWO <sub>4</sub> .....	110
4.11.1.1 The Kirkendall Effect.....	110
4.11.1.2 Hollow Nanoparticles.....	110
4.11.1.3 Hollow Nanotubes.....	112
4.11.2 Formation Mechanism of 1-Dimensional PbWO <sub>4</sub> nanorods: Spherical Diffusion Model.....	114
4.12 Effect of Synthesis Temperature on Morphology of PbWO <sub>4</sub> .....	116
4.13 Effect of Synthesis Temperature on morphology of PbWO <sub>4</sub> : Ce.....	118
References.....	122

## **Chapter 5 OPTICAL STUDIES: PHOTOLUMINESCENCE**

5.1 Luminescence.....	124
5.2 General characteristics of Photoluminescence spectra of PbWO <sub>4</sub> .....	125
5.3 Electronic Structure of PbWO <sub>4</sub> .....	126
5.4 Self Trapped Exciton (STE).....	127
5.5 Crystal-field splitting and hybridization of the molecular orbital of tetrahedral WO <sub>4</sub> <sup>2-</sup> group.....	128
5.6 Cerium.....	130
5.7 Luminescence of PbWO <sub>4</sub> due to scheelite phase.....	132
5.7.1 Blue emission.....	132
5.7.2 Green emission.....	132
5.7.3 Two Green emission bands G(I) and G(II).....	132
5.7.4 G(I) emission band.....	132
5.7.5 G(II) emission band.....	133

5.8 Effect of Lead Source on PhotoLuminescence of PbWO <sub>4</sub> phosphor.....	134
5.8.1 Lead acetate and Lead Nitrate as Lead Sources.....	135
5.8.2 Lead Chloride as a lead source.....	140
5.9 Effect of synthesis parameters on Photoluminescence.....	146
5.10 Excitation spectra.....	147
5.11 Emission spectra.....	148
5.12 PL spectra of undoped and Cerium doped PbWO <sub>4</sub> synthesized at 200°C.....	150
5.13 Effect of pH on Photoluminescence of PbWO <sub>4</sub> nanophosphor.....	154
5.14 Effect of synthesis Temperature on Photoluminescence of PbWO <sub>4</sub> .....	159
5.15 Effect of synthesis Temperature on Photoluminescence of PbWO <sub>4</sub> :Ce.....	165
5.16 Up Conversion emission (anti-Stokes emission) in PbWO <sub>4</sub> .....	170
5.16.1 Red emission center.....	172
References.....	173
<b>Chapter 6 SUMMARY AND CONCLUSIONS.....</b>	<b>177</b>
<b>Publications.....</b>	<b>190</b>

## LIST OF TABLES

<b>Table 2.1</b> PbWO <sub>4</sub> and PbWO <sub>4</sub> :Ce prepared with different Lead Sources.....	32
<b>Table 2.2</b> PbWO <sub>4</sub> and PbWO <sub>4</sub> :Ce prepared at different reaction conditions using Lead Chloride as a Lead Source.....	33
<b>Table 3.1</b> Summary of reaction conditions to synthesize PbWO <sub>4</sub> and PbWO <sub>4</sub> : Ce using different Lead sources.....	46
<b>Table 3.2</b> Summary of phase, lattice parameters, unit cell volume and average crystallite size of undoped and Cerium doped PbWO <sub>4</sub> .....	48
<b>Table 3.3</b> PbWO <sub>4</sub> and PbWO <sub>4</sub> : Ce prepared at different reaction conditions using Lead chloride as a lead source.....	54
<b>Table 3.4</b> PbWO <sub>4</sub> prepared with different pH of reaction solution.....	55
<b>Table 3.5</b> Summary of phase identified, lattice parameters, unit cell volume and average crystallite size of PbWO <sub>4</sub> prepared at different pH.....	59
<b>Table 3.6</b> PbWO <sub>4</sub> synthesized at different reaction temperatures.....	60
<b>Table 3.7</b> Summary of phase identified, lattice parameters, unit cell volume and average crystallite size of PbWO <sub>4</sub> prepared at different Temperature.....	62
<b>Table 3.8</b> PbWO <sub>4</sub> :Ce synthesized at different reaction temperatures.....	66
<b>Table 3.9</b> Summary of phase identified, lattice parameters, unit cell volume and average crystallite size of PbWO <sub>4</sub> :Ce prepared at different Temperature.....	69
<b>Table 4.0</b> Summary of phase identified, lattice parameters, unit cell volume and average cystallite size of undoped and Cerium doped PbWO <sub>4</sub> prepared at different Temperature.....	76
<b>Table 4.1</b> Summary of lattice parameter and atomic packing density of different lead sources.....	93
<b>Table 4.2</b> Summary of morphologies and particle size of undoped and Cerium doped PbWO <sub>4</sub> prepared using different Lead sources.....	105
<b>Table 4.3</b> Summary of reaction conditions of undoped and Cerium doped PbWO <sub>4</sub> samples selected for TEM analysis.....	106
<b>Table 4.4</b> Summary of reaction conditions, phase, morphologies and particle size of undoped and Cerium doped PbWO <sub>4</sub> prepared using different Lead chloride...	121

<b>Table 5.1</b> Summary of Phase produced, Morphologies and Particle size of undoped and Cerium doped PbWO <sub>4</sub> prepared using different Lead sources.....	134
<b>Table 5.2</b> The locations and Intensity of Gaussian components of PL spectra of PbWO <sub>4</sub> and PbWO <sub>4</sub> : Ce prepared at 100°C.....	142
<b>Table 5.3</b> Summary of reaction conditions, phase, morphologies and particle size of undoped and Cerium doped PbWO <sub>4</sub> prepared using different Lead chloride...	146
<b>Table 5.4</b> The locations and intensity of Gaussian components of PL spectra of PbWO <sub>4</sub> and PbWO <sub>4</sub> : Ce prepared at 200°C.....	151
<b>Table 5.5</b> The locations and Intensity of Gaussian components of PL spectra of PbWO <sub>4</sub> samples prepared at different pH.....	157
<b>Table 5.6</b> The locations and Intensity of Gaussian components of PL spectra of PbWO <sub>4</sub> samples prepared at different temperatures.....	163
<b>Table 5.7</b> The locations and intensity of Gaussian components of PL spectra of PbWO <sub>4</sub> : Ce samples prepared at different temperatures.....	168

## LIST OF FIGURES

<b>Figure 2.1</b> Phase diagram of water.....	21
<b>Figure 2.2</b> Variation of dielectric constant of water with temperature and pressure [10].....	22
<b>Figure 2.3</b> Teflon-Lined Stainless Steel Autoclave.....	28
<b>Figure 2.4</b> Flow chart of Hydrothermal Synthesis.....	31
<b>Figure 3.2.1</b> Photograph of XRD instrument at UGC-CSR, Indore Centre.....	40
<b>Figure 3.2.2</b> Photograph of XRD instrument at ERDA, Vadodara.....	41
<b>Figure 3.3.1</b> Xrd reflections of undoped and Cerium doped $\text{PbWO}_4$ synthesized using Lead acetate (1, 2) and Lead nitrate (3, 4).....	47
<b>Figure 3.3.2</b> Xrd reflections of undoped and Cerium doped $\text{PbWO}_4$ synthesized using Lead chloride (5,6).....	47
<b>Figure 3.3.3</b> Magnified (112) reflection peak of (a) Sample 1-4 (b) Sample 5-6.....	52
<b>Figure 3.5.1</b> Indexed XRD reflections of $\text{PbWO}_4$ synthesized at (a) 3pH, (b) 7pH and (c) 11pH.....	56
<b>Figure 3.5.2</b> XRD pattern of $\text{PbWO}_4$ prepared at different pH.....	57
<b>Figure 3.5.3</b> Shift of (112) reflection peak of $\text{PbWO}_4$ prepared at different pH.....	58
<b>Figure 3.6.1</b> XRD pattern of $\text{PbWO}_4$ prepared at different temperature.....	62
<b>Figure 3.6.2</b> Effect of synthesis Temperature on Lattice Parameters of $\text{PbWO}_4$ .....	63
<b>Figure 3.6.3</b> Effect of synthesis Temperature on Volume and Average Crystallite size of $\text{PbWO}_4$ .....	64
<b>Figure 3.6.4</b> Shift of (112) peak of $\text{PbWO}_4$ synthesized at different temperature.....	65
<b>Figure 3.7.1</b> Indexed XRD spectra of $\text{PbWO}_4$ : Ce synthesized at (a) R.T. (b) 100°C (c) 150°C and (d) 200°C.....	68
<b>Figure 3.7.2</b> XRD pattern of $\text{PbWO}_4$ :Ce prepared at different Temperature.....	68
<b>Figure 3.7.3</b> Effect of synthesis Temperature on Lattice Parameters of $\text{PbWO}_4$ :Ce.....	70

<b>Figure 3.7.4</b> Effect of synthesis Temperature on Volume and Average Crystallite size of $\text{PbWO}_4\text{:Ce}$ .....	71
<b>Figure 3.7.5</b> Shift of (112) peak of $\text{PbWO}_4\text{:Ce}$ synthesized at different temperature.....	72
<b>Figure 3.8.1</b> Xrd spectra of $\text{PbWO}_4$ and $\text{PbWO}_4\text{:Ce}$ synthesized at $100^\circ\text{C}$ .....	74
<b>Figure 3.8.2</b> Xrd spectra of $\text{PbWO}_4$ and $\text{PbWO}_4\text{:Ce}$ synthesized at $150^\circ\text{C}$ .....	75
<b>Figure 3.8.3</b> Xrd spectra of $\text{PbWO}_4$ and $\text{PbWO}_4\text{:Ce}$ synthesized at $200^\circ\text{C}$ .....	75
<b>Figure 3.8.4</b> Shift of (112) peak of undoped and Cerium doped $\text{PbWO}_4$ prepared at different temperature.....	77
<b>Figure 4.1</b> Photograph of TEM (Model : Philips Tecnai 20 G2, FEI make) instrument at UGC-CSR, Indore Centre.....	82
<b>Figure 4.2</b> Photograph of TEM (Model : Philips Tecnai 20, Holland) instrument at SICART, Vidhyanagar, Anand.....	83
<b>Figure 4.3</b> Photograph of SEM (JEOL JSM-6380LV) instrument at ERDA, Vadodara.....	84
<b>Figure 4.4</b> SEM images of $\text{PbWO}_4$ (a) agglomeration of dendrite with single trunk reported in ref. [2]; (b) single trunk dendrite produced using Lead acetate as lead source; (c) tetrahedron microparticles reported in ref. [3]; (d) tetrahedron microparticles produced using Lead acetate as lead source.....	89
<b>Figure 4.5</b> SEM images of microbelts (left) and octahedron microparticles (right) of $\text{PbWO}_4\text{:Ce}$ produced using Lead acetate as lead source.....	90
<b>Figure 4.6</b> TEM images of $\text{PbWO}_4\text{:Ce}$ produced using Lead acetate as lead source.....	91
<b>Figure 4.7</b> Growth mechanism of $\text{PbWO}_4$ microbelt suggested by C. Zheng [7].....	93
<b>Figure 4.8</b> (a) SEM image of agglomerated microbelts and dendrites of $\text{PbWO}_4$ ; (b) High magnified SEM image of individual six branched/trunk dendrite (inset shows same dendrite with scale); (c) Three dimensional dendrite reported in [9] by Biao Liu et al. with CTAB surfactant.....	95

<b>Figure 4.9</b> TEM image of rhombic shaped $\text{PbWO}_4$ microparticles (a) synthesized by us without using any surfactant; (b) synthesized by using PVP [12] and (c) CTAB [13] surfactant; (d) nanoparticles prepared without surfactant.....	97
<b>Figure 4.10</b> TEM images of Cerium doped tetrahedron $\text{PbWO}_4$ prepared using Lead nitrate as a Lead source with different magnification.....	100
<b>Figure 4.11</b> TEM images of agglomerated octahedron microparticles and flat micro belts of $\text{PbWO}_4$ prepared with Lead Chloride (both images are of same sample).....	102
<b>Figure 4.12</b> TEM images of agglomerated tetrahedron microparticles of Cerium doped $\text{PbWO}_4$ prepared with Lead Chloride (both images are of same sample).....	103
<b>Figure 4.13</b> The high-magnification TEM images of (a) quasi-spherical hollow nano particles (HNPs) of $\text{PbWO}_4$ with scale (b) hollow nano tubes (HNTs) of $\text{PbWO}_4$ with scale (c) individual single HNT.....	109
<b>Figure 4.14</b> Schematic diagram showing formation of $\text{PbWO}_4$ Hollow Nano Particles by Process A.....	111
<b>Figure 4.15</b> Polycrystalline $\text{Ag}_2\text{Se}$ nanotubes [29].....	112
<b>Figure 4.16</b> TEM image of agglomerated $\text{PbWO}_4$ nanorods.....	113
<b>Figure 4.17</b> TEM images of $\text{PbWO}_4$ prepared at (a-b) $100^\circ\text{C}$ and (c-d) $125^\circ\text{C}$ temperatures.....	117
<b>Figure 4.18</b> TEM images of $\text{PbWO}_4:\text{Ce}$ prepared at (a-b) $100^\circ\text{C}$ and (c-d) $200^\circ\text{C}$ temperatures.....	118
<b>Figure 4.19</b> TEM image of $\text{PbWO}_4$ microparticle synthesized by hydrothermal method using Tripotassium citrate surfactant at $180^\circ\text{C}$ temperature by Wei Zhao.....	119

<b>Figure 5.1</b> Band Structure of $\text{PbWO}_4$ .....	126
<b>Figure 5.2</b> Schematic diagram of a crystal field splitting and hybridization $\text{WO}_4^{2-}$ group [4].....	128
<b>Figure 5.3(a)</b> PL spectra of $\text{PbWO}_4$ synthesized with different Lead Sources.....	137
<b>Figure 5.3(b)</b> PL spectra of $\text{PbWO}_4$ synthesized with Lead Acetate.....	137
<b>Figure 5.3(c)</b> PL spectra of $\text{PbWO}_4$ synthesized with Lead Nitrate.....	137
<b>Figure 5.4</b> PL spectra of $\text{PbWO}_4$ prepared with Lead Chloride at $100^\circ\text{C}$ .....	140
<b>Figure 5.5</b> Splitting of Triplet states due to Jahn-Teller effect [45].....	143
<b>Figure 5.6</b> Excitation spectra of $\text{PbWO}_4$ (sample 8).....	147
<b>Figure 5.7</b> Effect of Synthesis Parameters on PhotoLuminescence intensity.....	149
<b>Figure 5.8</b> PL spectra of $\text{PbWO}_4$ synthesized at $200^\circ\text{C}$ .....	150
<b>Figure 5.9</b> PL emission of $\text{PbWO}_4$ synthesized at different pH excited with 300nm.....	154
<b>Figure 5.10</b> PL emission of $\text{PbWO}_4$ synthesized at different pH excited with 254 nm.....	155
<b>Figure 5.11</b> PL spectra of $\text{PbWO}_4$ synthesized at different temperatures.....	159
<b>Figure 5.12</b> PL spectra of $\text{PbWO}_4$ prepared at different temperatures excited with 254nm.....	161
<b>Figure 5.13</b> PL spectra of $\text{PbWO}_4:\text{Ce}$ prepared at different temperatures excited with 300nm.....	165
<b>Figure 5.14</b> PL spectra of $\text{PbWO}_4:\text{Ce}$ prepared at different temperatures excited with 254nm.....	166
<b>Figure 5.15</b> Up-conversion luminescence in $\text{PbWO}_4$ synthesized at different pH.....	170
<b>Figure 5.16</b> Up-conversion luminescence in $\text{PbWO}_4$ synthesized at different Temperatures.....	171

## 1.1 Introduction of Tungstate – A General Background

It is known that tungstate is a very important family of inorganic materials that has wide applications in many fields, such as Photoluminescence, Microwave applications, Optical fibres, Scintillator materials, Humidity sensors, Catalysis, etc. As a self-activating phosphor, tungstate has some advantages, e.g. high chemical stability, high X-ray absorption coefficient, high Light Yield, and low afterglow to luminescence. Tungstate crystals can be divided in two groups: Scheelite ( $\text{CaWO}_4$ ,  $\text{BaWO}_4$  and  $\text{PbWO}_4$ ) and Wolframite ( $\text{MgWO}_4$ ,  $\text{ZnWO}_4$  and  $\text{CdWO}_4$ ).  $\text{BaWO}_4$  shows very weak luminescence at liquid helium temperature which vanishes at room temperature.  $\text{MgWO}_4$  is used as photoluminophor already for a long time [1].  $\text{ZnWO}_4$  and  $\text{CdWO}_4$  are perspective materials in the field of computer tomography [2].  $\text{CaWO}_4$  is an effective luminophor which is used for more than hundred years in medical purpose and in luminescence lamp but its slow luminescence decay (about  $100\mu\text{s}$ ) restricts its use in optical devices based on low time resolution.

Hence out of all tungstates,  $\text{PbWO}_4$  has become a subject of renewed interest about 15 years ago when its favorable characteristics as scintillation detector were reported. Though  $\text{PbWO}_4$  has a low light yield (100 times smaller than  $\text{CaWO}_4$ ), its very short decay time (ns) makes it the strongest candidate for scintillation detector. High density of  $\text{PbWO}_4$  also favors its use in high energy physics and medical applications. There are hundreds of papers already published on  $\text{PbWO}_4$  large single crystals but very few papers are reported on  $\text{PbWO}_4$  with nanometer range, particularly on Cerium doped  $\text{PbWO}_4$  nanophosphor. Large single crystals of  $\text{PbWO}_4$  are produced either via Czochralski or Bridgman methods which require highly expensive and specially designed equipments. These methods produce  $\text{PbO}$  and  $\text{WO}_3$  harmful gases during crystal growth due to higher synthesis temperature (i.e.  $1125^\circ\text{C}$ ). Moreover,  $\text{PbWO}_4$

crystals obtained from these methods presents several problems, such as: inhomogeneity, impurity contamination and powders with different sizes and non-uniform distribution. Products obtained by these methods are in bulk size which cannot be used for devices based on nano dimensions. These limitations lower the applicability of these methods for large scale production of  $\text{PbWO}_4$  crystals.

Since  $\text{PbWO}_4$  Phosphor has structure sensitivity and its luminescence properties remarkably affected by structure defects present in the crystal. We can improve its scintillating properties through changing and controlling its structure defects, such as appropriate doping and controlling synthesis temperature. Doping with rare earth ions adjust the defects in the Pure  $\text{PbWO}_4$  and eliminate some harmful defects. Earlier studies found that some related experimental parameters including the concentration of the anionic surfactant, the water content, and reaction temperature have great influences on the product morphology. By carefully controlling these experimental parameters,  $\text{PbWO}_4$  nanostructures with morphologies of bundles of rods, ellipsoids, spheres, bipyramids, and nanoparticles can be efficiently achieved. Cerium has been tried as a beneficial rare earth doping impurity recently. Cerium oxide ( $\text{CeO}_2$ ), one of the most important rare-earth oxides, has earned intensive interest in the past decades for its vital roles played in some emerging fields including environmental and energy related applications. Recent development in nanotechnology requires  $\text{PbWO}_4$  material having different morphologies and dimensions suitable for nano-devices. So it is important to study effect of different reaction parameters (Precursor, pH, Concentration, Time and Temperature) on morphology of the final product. Interesting applications of bulk sized  $\text{PbWO}_4$  and less reported properties of undoped and Cerium doped  $\text{PbWO}_4$  with nano dimensions motivate us to perform research work presented in this thesis.

To study the effect of different reactants, temperature and pH of reaction media on the structural and Optical properties of  $\text{PbWO}_4$  and Cerium doped  $\text{PbWO}_4$  phosphor.

### **OBJECTIVES AND SCOPE OF THE WORK**

In order to achieve this aim, following objectives have been set.

- To design and develop Teflon Lined Stainless Steel Autoclave which is efficiently able to synthesis  $\text{PbWO}_4$  phosphor.
- To synthesis undoped and Cerium doped  $\text{PbWO}_4$  phosphor with different Lead Sources, at reaction Temperature and pH of solution with Autoclave by Low temperature Hydrothermal Method.
- Characterization of as prepared samples with X-ray Diffraction (XRD), Transmission Electron Microscopy (TEM), Scanning Electron Microscopy (SEM) for structural studies.
- Characterization of as prepared samples with Photoluminescence (PL) for optical studies.

## 1.2 Lead Tungstate – $\text{PbWO}_4$

Lead Tungstate  $\text{PbWO}_4$  (PWO) occurs in the nature as tetragonal stolzite with scheelite type structure (space group  $I4_1/a$ ) and monoclinic raspite with wolframite type structure (space group  $P2_1/a$ ). Raspite phase transforms irreversibly to the stolzite one at about  $400^\circ\text{C}$  [3]. The first information on the emission properties of PWO is dated as early as the late 1940s [4]. Compared to other well-known scintillators such as  $\text{BaF}_2$ ,  $\text{CeF}_3$  and  $\text{CsI}$ ,  $\text{PbWO}_4$  phosphor is most attractive for its high-energy physics application because of its high density ( $8.3 \text{ g cm}^{-3}$ ), short decay time (less than 10 ns for a large light output), high irradiation damage resistance ( $10^7$  rad for undoped and  $10^8$  rad for La doped  $\text{PbWO}_4$ ), small moliere radius, fast decay time, non-hygroscopicity and low production cost [5-7].  $\text{PbWO}_4$  shows interesting excitonic luminescence, Thermoluminescence and stimulated Raman Scattering behavior [8, 9]. Lead tungstate crystals are fast and dense scintillators found an application for high energy electromagnetic calorimeter of Compact Muon Solenoid (CMS) detector at Large Hedron Collider (LHC) at Center of Europe for Research Nuclear (CERN).

### 1.3 History of Synthesis

Generally  $\text{PbWO}_4$  are grown from expensive methods, such as: high temperature solid-state reaction [10-12], flux method for whisker growth [13], from the melt using the Czochralski method [14–17], Bridgman method [18] and from the high temperature strain (HTS) [19]. Tungstate thin films have been prepared by reacting various metal oxide thin film with  $\text{WO}_3$  vapor [20]. Most of these methods require high temperature heating. At high temperature there is a tendency for the  $\text{WO}_3$  group to evaporate, resulting inhomogeneous composition of tungstates.

These methods require highly expensive and specially designed equipments for crystal growth. Evaporation of harmful gases such as  $\text{PbO}$  and  $\text{WO}_3$  during crystal growth due to higher synthesis temperature also lowers applicability of these methods for large scale production of  $\text{PbWO}_4$  crystals.  $\text{PbWO}_4$  crystals obtained from these methods presents several problems, such as: inhomogeneity, impurity contamination and powders with different sizes and nonuniform distribution. Moreover, products obtained by these methods are in bulk sized which cannot be used for devices which are based on nano dimensions.

To minimize these problems, soft chemical methods such as: sol–gel [21], sonochemical route [22, 23], microemulsion [23], microwave assisted route [24,25,26] and hydrothermal [27-30] have been employed to control with accuracy the chemical composition, homogeneity, microstructure, physical and chemical characteristics.

## SOME METHODS USED FOR NANOMATERIAL SYNTHESIS

### **Plasma arcing**

In Plasma arcing molecules and atoms are separated by vaporization and then allowed to deposit in a carefully controlled and orderly manner to form nanoparticles. Plasma is achieved by making inert gas conduct electricity by providing a potential difference across two electrodes. In arc discharge method, two high purity graphite electrodes as anode and cathode are held a short distance apart under a helium atmosphere. Carbon evaporated from the anode re-condensed at cathode and form carbon nanotubes.

### **Sol-gel synthesis**

The sol-gel process is a versatile solution process for making ceramic and glass materials. In general, the sol-gel process involves the transition of a system from a liquid "sol" into a solid "gel" phase. A sol is a dispersion of the solid particles (~ 0.1-1  $\mu$ m) in a liquid. The starting materials used in the preparation of the "sol" are usually inorganic metal salts or metal organic compounds such as metal alkoxides. In a typical sol-gel process, the precursor is subjected to a series of hydrolysis and polymerisation reactions to form a colloidal suspension, or a "sol".

### **Ion Sputtering**

In this method, accelerated ions such as  $\text{Ar}^+$  are directed toward the surface of a target to eject atoms and small clusters from its surface. The ions are carried to the substrate under a relatively high pressure (~1mTorr) of an inert gas, causing aggregation of the species. Nanoparticles of metals and alloys as well as semiconductors have been prepared using this method.

### **Solvothermal Synthesis**

The solvothermal method provides a means of using solvents at temperatures above their boiling points, by carrying out the reaction in a sealed vessel. The pressure

generated in the vessel due to the solvent vapors elevates the boiling point of the solvent. Typically, solvothermal methods make use of solvents such as ethanol, toluene, and water, and are widely used to synthesize zeolites, inorganic open-framework structures, and other solid materials.

### **Sonochemical Synthesis**

In order to carry out sonochemical reactions, a mix of reagents dissolved in a solvent is subjected to ultrasound radiation (20 kHz–10 MHz). Acoustic cavitation leads to the creation, growth, and collapse of bubbles in the liquid medium. The creation of bubbles is due to the suspended particulate matter and impurities in the solvent. The growth of a bubble by expansion leads to the creation of a vacuum that induces the diffusion of volatile reagents into the bubble. The growth step is followed by the collapse of the bubble which takes places rapidly accompanied by a temperature change of 5,000–25,000K in about a nanosecond.

### **Micelles and Microemulsions**

Reverse or inverted micelles formed by the dispersion of water in oil, stabilized by surfactants are useful templates to synthesize nanoscale particles of metals, semiconductors, and oxides [410–413]. This method relies on the ability of surfactants in the shape of truncated cones (like cork stopper), to trap spherical droplets of water in the oil medium, and thereby forming micelles. A micelle is designated inverse or reverses when the hydrophilic end of the surfactant points inward rather than outward as in a normal micelle.

Although these strategies are widespread demonstrated effective methods to fabricate  $\text{PbWO}_4$  nanostructures with various morphologies, large scale application of these methods has been limited due to some shortcomings, such as some methods

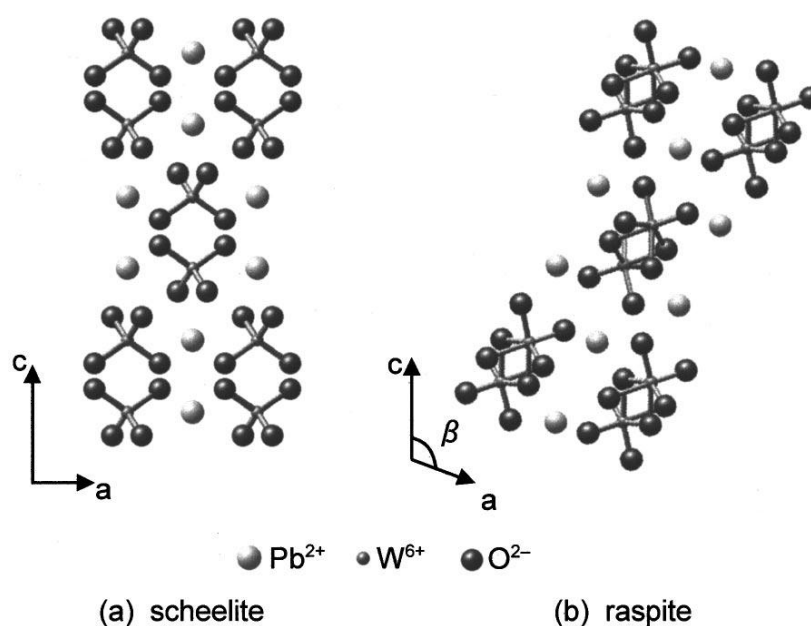
need expensive templates or surfactants, and others needing complicated process, or even tedious procedures.

Recently, significant efforts have been devoted to develop green method that take into account human and environmental impact in the selection of reactants and the reaction conditions for material fabrication. Many recent studies have demonstrated that hydrothermal process is an effective and versatile route for the synthesis of nanostructures having low-cost, high efficiency and good potential for high-quantity production [31]. A brief description of hydrothermal method is given in Chapter 2.

It is believable that controlling the morphology and architecture of  $\text{PbWO}_4$  crystals is expected to be effective in modifying their related properties for practical application. The shape, phase, and size of inorganic nanocrystals are important elements in varying their electrical, optical, and other properties, so control over these elements have become a hot research topic in recent years. The controlled synthesis of inorganic nano- and microcrystals with specific size, shape and structure is of fundamental significance in modern material science and engineering because the size, shape and structure could determine not only the relevant optical, electronic and magnetic properties of the materials but also the performances of those material-based devices for applications. Recently, many efforts have been made to synthesize tungstate crystals with controlled morphologies because of their excellent luminescent properties and promising applications.

## 1.4 Crystal Structure of $\text{PbWO}_4$

At room temperature,  $\text{PbWO}_4$  has two different possible polymorphs, tetragonal stolzite or scheelite structure with space group  $I4_1/a$  and monoclinic wolframite or raspite structure with space group  $P2_1/c$  [32]. Two different crystal structures of  $\text{PbWO}_4$  are shown in below image.



[Ref. M. Itoh and M. Fujita, Physical Review B, Vol. 62, Number 19]

### 1.4.1 Scheelite

In the scheelite structure, W ions are in tetrahedral O-ion cages and isolated from each other. Each  $\text{Pb}^{2+}$  cation is surrounded by eight oxygen ions. The connection between cation  $\text{Pb}^{2+}$  and anion  $\text{WO}_4^{-2}$  is ionic and the connection between  $\text{W}^{6+}$  and  $\text{O}^{2-}$  in the oxianion complex is covalent.

## 1.4.2 Raspite

In the raspite structure, the coordination number of W is six and  $\text{WO}_6^{-6}$  octahedra form a chain by edge sharing. Each  $\text{Pb}^{2+}$  cation is coordinated to seven oxygen ions. The monoclinic form of  $\text{PbWO}_4$  (raspite-type) can be treated as a distortion of the tetragonal form of  $\text{PbWO}_4$  (scheelite-type). It is known that the raspite phase is a metastable and minority form under normal conditions [33]. The raspite  $\text{PbWO}_4$  has not yet been successfully prepared in the laboratory and is obtained as a natural crystal except by C.Zheng [34].

From the structure point of view, in spite of the very small volume difference of 0.53% between the raspite and scheelite forms, the difference in the cation coordination is remarkable. As displayed in Fig.1, which gives the atomic structures of both raspite and scheelite, the W atoms in the scheelite structure are at the tetrahedral O-atom cages and isolated from one another, whereas in the raspite phase, two W atoms share two O ions to form a chain of edge-shared octahedra. Each Pb ion is surrounded by seven O ions in the raspite structure, whereas in the scheelite structure, the number of the surrounding O ions to each Pb ion is eight [35]. It was reported that displacement of O ions in such a phase transformation is considered small, while that of the cations is relatively large. The body-center primitive tetragonal ( $Z = 4$ ) of  $\text{PbWO}_4$  the total number of degrees of freedom for the atomic vibrations is  $3N = 72$ . In  $\text{PbWO}_4$ , the  $\text{Pb}^{2+}$  ions and the tetrahedral  $[\text{WO}_4]^{2-}$  ions are at the  $S_4$ -symmetry crystallographic positions [36].

## 1.5 Doping with Trivalent Rare Earth Ions ( $\text{RE}^{3+}$ )

In order to use  $\text{PbWO}_4$  crystal as scintillation detector its radiation hardness should have high value. The radiation damage in  $\text{PbWO}_4$  crystals is caused by host structural defects called color centers e.g. Oxygen vacancies ( $V_o$ ) and Lead vacancies ( $V_{Pb}$ ) [37]. Such vacancies are produced due to high synthesis temperature during crystal growth which introduces local charge imbalance. So to improve radiation hardness by decreasing concentration of these vacancies, low temperature hydrothermal method is preferable. To balance charge these vacancies act as charge traps centers.  $V_o$  and  $V_{Pb}$  act as electron and hole traps respectively. Out of these two,  $V_o$  is mainly responsible for radiation damage in  $\text{PbWO}_4$ . So in order to decrease  $V_o$ , post-growth annealing at high temperature is required.

Doping with trivalent rare earth ion is another approach which minimizes the charge imbalance produced by vacancies. In 1997, Kobayashi et al. first reported that  $\text{La}^{3+}$  doping into  $\text{PbWO}_4$  could improve both the radiation hardness and the transmittance in the short-wavelength region [38]. Since then, doping with different impurity ions, especially rare-earth ions ( $\text{RE}^{3+}$ ), has become the focus of studies to ameliorate its scintillating characteristics.

### 1.5.1 Cerium

Cerium is the most abundant member of the series of elements known as lanthanides or rare earths. Cerium is characterized chemically by having two stable valence states one is  $\text{Ce}^{4+}$ , *ceric*, and the other is  $\text{Ce}^{3+}$ , *cerous*. The ceric ion is a powerful oxidizing agent but when associated with the strongly coordinating ligand, oxygen, is completely stabilized and induced cerium oxide,  $\text{Ce}^{4+}\text{O}_2$ , (also called ceria) is the form of cerium most widely used. The ground state of all the Lanthanide atoms is probably either  $[\text{Xe}] 4f^n 5d^1$  or  $[\text{Xe}] 4f^{n+1}$  where the increase in n from 0 to 14 corresponds to the change from La ( $Z=57$ ) through to Lu ( $Z=71$ ).

Cerium is the second and most reactive member of the lanthanides series. It is electro-positive in nature and become predominantly chemically reactive due to the low ionization potential for the removal of the three most weakly bound electrons. For all lanthanides the most stable state is a trivalent one,  $\text{Ln}^{3+}$ , with  $[\text{Xe}]4f^n$ ; i.e. for  $\text{Ce}^{3+}$ ,  $[\text{Xe}]4f^1$ . Rare earth ions have unfilled optically active 4f electrons screened by outer electronic filled shells. Because of these unfilled shells, this kind of ion is usually called *paramagnetic ions*.

The rare earth (RE) ions most commonly used for applications as phosphors, lasers, and amplifiers. The cerium atom ( $Z=58$ ), which has an outer electronic configuration  $5s^2 5p^6 5d^1 4f^1 6s^2$ . These atoms are usually incorporated in crystals as divalent or trivalent cations. In trivalent ions 5d, 6s, and some 4f electrons are removed and so  $(\text{RE})^{3+}$  ions deal with transitions between electronic energy sublevels of the  $4f^n$  electronic configuration. Divalent lanthanide ions contain one more f electron (for instance, the  $\text{Eu}^{2+}$  ion has the same electronic configuration as the  $\text{Gd}^{3+}$  ion, the next element in the periodic table but, at variance with trivalent ions, they to

show  $f \rightarrow d$  inter-configurational optical transitions. This aspect leads to quite different spectroscopic properties between divalent and trivalent ions. The  $4f^n$  electrons are, in fact, the valence electrons that are responsible for the optical transitions.

**The number of 4f electrons (n) in trivalent lanthanide ions**

Ion	n
$Ce^{3+}$	1
$Pr^{3+}$	2
$Nd^{3+}$	3
$Pm^{3+}$	4
$Sm^{3+}$	5
$Eu^{3+}$	6
$Gd^{3+}$	7
$Tb^{3+}$	8
$Dy^{3+}$	9
$Ho^{3+}$	10
$Er^{3+}$	11
$Tm^{3+}$	12
$Yb^{3+}$	13

These valence electrons are shielded by the 5s and 5p outer electrons of the  $5s^2 5p^6$  less energetic configurations. Because of this shielding effect, the valence electrons of  $Ce^{3+}$  ion are weakly affected by the ligand ions in  $PbWO_4$  crystals; a situation results the case of a weak crystalline field. For Weak crystalline field:  $H_{CF} \leq H_{SO}, H_{ee}, H_o$ . Consequently, the spin-orbit interaction term of the free  $Ce^{3+}$  ion Hamiltonian is dominant over the crystalline field Hamiltonian term. In this case, the energy levels

of the free  $\text{Ce}^{3+}$  ion are only slightly perturbed (shifted and split) by the crystalline field. This causes the  $^{2S+1}L_J$  states of the  $(\text{RE})^{3+}$  ions to be slightly perturbed when these ions are incorporated in crystals. The effect of the crystal field is to produce a slight shift in the energy of these states and to cause additional level splitting. However, the amount of this shift and the splitting energy are much smaller than the spin-orbit splitting, and thus, the optical spectra of  $(\text{RE})^{3+}$  ions are fairly similar to those expected for free ions. The free ion wavefunctions are then used as basis functions to apply perturbation theory,  $H_{\text{CF}}$  being the perturbation Hamiltonian over the  $^{2S+1}L_J$  states (where  $S$  and  $L$  are the spin and orbital angular momenta and  $J = L + S$ ). This approach is generally applied to describe the energy levels of trivalent rare earth ions, since for these ions the 4f valence electrons are screened by the outer  $5s^2 5p^6$  electrons. These electrons partially shield the crystalline field created by the B ions.

## References

1. G. Blasse and B.C. Grabmaier “Luminescent Materials”, springer-verlag, 226p, 1994.
2. R. Deych, J. Dobbs, S. Marcovic and B. Tuval , Proc. of the int. conf. on Inorganic Scintillator and Their application, SCINT-95, Netherlands, Delft, 36, 1996.
3. R. Shaw and G.F. Claringull, Am. Mineral, 40, 933, 1955.
4. F.A. Kroger, Some Aspects of the Luminescence of Solids, Elsevier, Amsterdam, New York, 1948.
5. P. Lecoq, I. Dafinei , E. Auffray , M. Schneegans ,V. Korzhik , O.V. Missevitch, V.B. Pavlenko, A.A. Fedorov, A.N. Annenkov, V.L. Kostylev, Nucl. Instrum. Meth. A 365, 291, 1995.
6. M. Kobayashi, M. Ishii, Y. Usuki, Nucl. Instrum. Methods Phys. Res. A 406 442,1998.
7. K. Hara, M. Ishii, M. Kobayashi, M. Nikl, H. Takano, M. Tanaka, K. Tanji, Y. Usuki, Nucl. Instrum. Methods Phys. Res. A, 414, 325, 1998.
8. Kobayashi, M., Ishii, M.; Usuki, Y. Nucl. Instrum. Methods Phys. Res., Sect. A, 406, 442,1998.
9. Hara, K., Ishii, M., Kobayashi, M., Nikl, M., Takano, H., Tanaka, M., Tanji, K., Usuki, Y. Nucl. Instrum. Methods Phys. Res., Sect. A 414 (1998) 325.
10. G. Blasse, L.H. Brixner, Chem. Phys. Lett. 409 (1990) 173.
11. Y. Huang, Q. Feng, Y. Yang, H.J. Seo, Phys. Lett. A 336 (2005) 490– 497.
12. Z. Qi, C. Shi, D. Zhou, H. Tang, T. Liu, T. Hu, Phys. Rev. B: Condens. Matter 307 (2001) 45–50.
13. S. Oishi, M. Hirao, Bull. Chem. Soc. Jpn. 63 (1990) 984.

14. W. Cho, M. Yashima, M. Kakihana, A. Kuso, T. Sakata, M. Yoshimura, *Appl. Phys. Lett.* 66 (1995) 1022.
15. K. Nitsch, M. Nikl, S. Ganschow, P. Reiche, R. Uecker, *J. Cryst. Growth* 165 (1996) 163.
16. N. Senguttuvan, P. Mohan, S.M. Babu, C. Subramanian, *J. Cryst. Growth* 183 (1998) 391–397.
17. A.V. Denisov, V.T. Gabrielyan, J.O. Punin, O.S. Grunsky, N.A. Sennova, *J. Cryst. Growth* 275 (2005) 697–701.
18. K. Tanji, M. Ishii, Y. Usuki, K. Hara, H. Takano, A. Senguttuvan, *J. Cryst. Growth* 204 (1999) 505.
19. D. Schultze, K.Th. Wilke, Ch. Waligorn, *Z. Anorg. Allg. Chem.* 352 (1967) 184.
20. S. Nobuhiro, K. Akihiko, K. Tadayoshi, *Bull. Chem. Soc. Jpn.* 69 (1996) 1241–1245.
21. K. Nitsch, M. Nikl, M. Rodov' a, S. Santucci, *Phys. Status Solidi A* 179 (2000) 261–264.
22. J. Geng, J.-J. Zhu, D.-J. Lu, H.-Y. Chen, *Inorg. Chem.* 45 (2006) 8403–8407.
23. D. Chen, G. Shen, K. Tang, Z. Liang, H. Zheng, *J. Phys. Chem. B* 108 (2004) 11280–11284.
24. Guizhen Wang, Chuncheng Hao *Materials Research Bulletin* 44 (2009) 418–421.
25. Jeong Ho Ryu, Jong-Won Yoon, Kwang Bo Shim, *Solid State Communications* 133 (2005) 657–661.
26. HuaTang, Changsheng Li, Haojie Song, Xiaofei Yang and Xuehua Yan, *CrystEngComm*, 13(2011) 5119–5124.
27. C. An, K. Tang, G. Shen, C.Wang, Y. Qian, *Mater. Lett.* 57 (2002) 565–568.

28. Guangyu Chen, Liangbao Yang, and Jinhuai Liu, *Cryst. Res. Technol.* 44, No. 7, (2009) 736 – 740.
29. Wei Zhao, Xinyu Song, Guozhu Chen, Guangru Tian, Sixiu Sun *Materials Letters* 63 (2009) 285–288.
30. D.Tawde, M.Srinivas & K.V.R.Murthy, *Physica Status Solidi A*, Vol.208, Issue 4, 803- 807, 2011.
31. W.X. Zhang, X.G. Wen, S.H. Yang, Y. Berta, Z.L. Wang, *Adv. Mater.* 15 (2003) 822.
32. T. Fujita, I. Kawada, and K. Kato, *Acta Crystallogr. Sect. B: Struct. Sci.* 33(1977)162.
33. R. Shaw and G. F. Claringbull, *Am. Mineral.* 40 (1955) 933.
34. Chunhua Zheng, Chenguo Hu, Xueyan Chen, Hong liu, Yufeng Xiong, Jing Xu, Buyong Wana and Linyong Huang, *CrystEngComm*,12 (2010) 3277–3282.
35. L. S. Cavalcante, J. C. Sczancoski, V. C. Albarici, J. M. E. Matos, J. A. Varela, and E. Longo, *Mater. Sci. Eng., B* 150 (2008) 18.
36. A.A. Kaminskii, C.L. McCray, H.R. Lee, S.W. Lee, D.A. Temple, T.H. Chyba, W.D. Marsh, J.C. Barnes, A.N. Annanenko, V.D. Legun, H.J. Eichler, G.M.A. Gad, K. Ueda, *Opt. Commun.* 183 (2000) 277.
37. R.Y. Zhu, et al., *Nucl. Instr. and Meth. A* 376 (1996) 319.
38. M. Kobayashi, Y. Usuki, M. Ishii, T. Yazawa, K. Hara: *Nucl. Instrum. Methods Phys. Res. A* 399 (1997) 261.

## 2.1 History

The Hydrothermal Technique has been the most popular one, gathering interest from scientists and technologists of different disciplines, particularly in the last fifteen years. The word “*hydrothermal*” has geological origin. A self-explanatory word, “hydro” meaning water and “thermal” meaning heat. British Geologist, Sir Roderick Murchison (1792–1871) was the first to use this word, to describe the action of water at elevated temperature and pressure in bringing about changes in the earth’s crust leading to the formation of various rocks and minerals [1]. The first publication on hydrothermal research appeared in 1845. This reports the successful synthesis of tiny quartz crystals upon transformation of freshly precipitated silicic acid in Papin’s digester by K. F. E. Schafthaul. The term hydrothermal usually refers to any heterogeneous reaction in the presence of aqueous solvents or mineralizers under high pressure and temperature conditions.

Hannay (1880) claimed to have synthesized artificial diamond using Hydrothermal Technique. Similarly, Moissan (1893) also claimed to have synthesized diamond artificially as large as 0.5 mm from charcoal. The first ever large size crystals obtained by the earliest workers was that of hydrated Potassium Silicate, which was about 2–3 mm long, by Friedel and Sarasin (1881). Friedel and Sarasin (1881) termed their hydrothermal autoclave as *hydrothermal bomb*, because of the high pressure working conditions in their experiments.

## 2.2 Definitions

There are different definitions proposed by various scientists for hydrothermal method in literature. In 1913 Morey and Niggli defined hydrothermal synthesis as "...in the hydrothermal method the components are subjected to the action of water, at temperatures generally near though often considerably above the critical temperature of water ( $\sim 370^{\circ}\text{C}$ ) in closed bombs, and therefore, under the corresponding high pressures developed by such solutions " [2]. In Ref. [3] Laudise defined it as "hydrothermal growth means growth from aqueous solution at ambient or near-ambient conditions". Rabenau in 1985 defined hydrothermal synthesis as the heterogeneous reactions in aqueous media above  $100^{\circ}\text{C}$  and 1 bar [4]. Lobachev defined it as a group of methods in which crystallization is carried out from superheated aqueous solutions at high pressures [5]. According to Roy hydrothermal synthesis involves water as a catalyst and occasionally as a component of solid phases in the synthesis at elevated temperature ( $>100^{\circ}\text{C}$ ) and pressure (greater than a few atmospheres) [6]. Byrappa in 1992 defines hydrothermal synthesis as any heterogeneous reaction in an aqueous media carried out above room temperature and at pressure greater than 1 atm [7]. Yoshimura in ref [8] defined it as "...reactions occurring under the conditions of high-temperature-high-pressure ( $>100^{\circ}\text{C}$ ,  $>1$  atm) in aqueous solutions in a closed system". With the vast number of publications under mild hydrothermal conditions in recent years, K. Byrappa in 2001 propose to define hydrothermal reaction as "any heterogeneous chemical reaction in the presence of a solvent (whether aqueous or nonaqueous) above room temperature and at pressure greater than 1 atm in a closed system." [9].

## **2.3 Water as a Reaction Medium**

Water is one of the most important solvent present in nature in abundant amount and has remarkable properties as a reaction medium under hydrothermal conditions. Water shows different characteristics under hydrothermal conditions than that of standard conditions. One of the biggest advantages of using water is the environmental benefit and cheaper than other solvents, and it can act as a catalyst for the formation of desired materials by tuning the temperature and the pressure. It is nontoxic, nonflammable, noncarcinogenic, nonmutagenic, and thermodynamically stable. Another advantage is that water is very volatile, so it can be removed from the product very easily.

Hydrothermal solvents have different properties at above 100°C and above 1 atm, especially at critical point. In order to understand hydrothermal reactions the properties of solvent under hydrothermal conditions must be known very well.

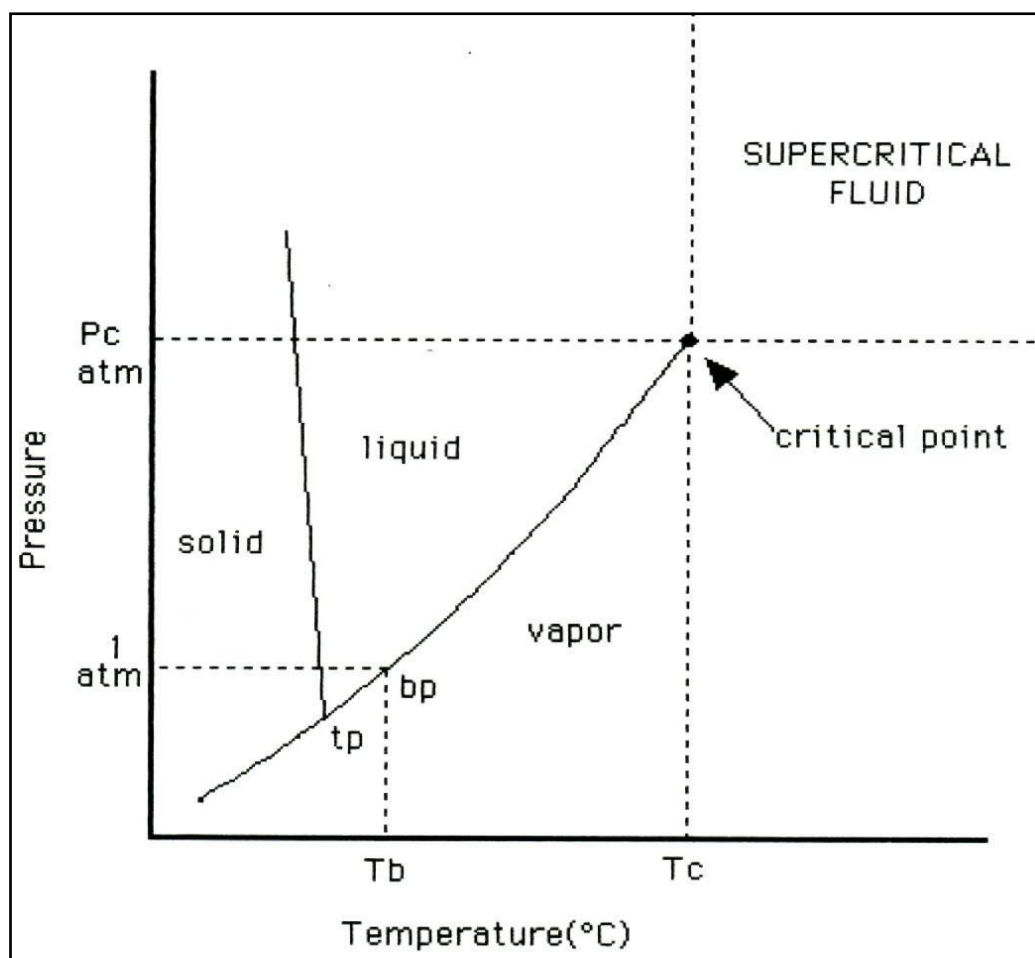


**Figure 2.1** Phase diagram of water.

In the Figure 2.1, the critical point marks the end of liquid-vapor coexistence curve at the critical temperature,  $T_c$ , and pressure,  $P_c$ , in a phase diagram for a pure homogenous substance. A fluid is defined as being supercritical if it is maintained at conditions above its critical temperature and pressure. The properties of supercritical fluids (SCFs) vary depending on the pressure and temperature and frequently described as being intermediate between those of a gas and a liquid. As the temperature increases, the liquid becomes less dense due to thermal expansion and at the same time the gas becomes denser. At the critical point the densities of both phases become the same. The compound is neither liquid nor gas any longer above

the critical point, and it becomes supercritical fluid. After that, the phases of liquid and gas are not distinguishable and properties of SCF will be between gas and liquid.

Diffusivity and viscosity symbolizes transport properties that influence rates of mass transfer. Diffusivity is at least an order of magnitude higher and viscosity is lower compared with a liquid solvent. This means that diffusivity of reactants in SCF will occur faster than that in a liquid solvent, which means that solids can dissolve and migrate more rapidly in SCFs. High diffusivity, low viscosity and intermediate density of water increases the rate of the reaction.

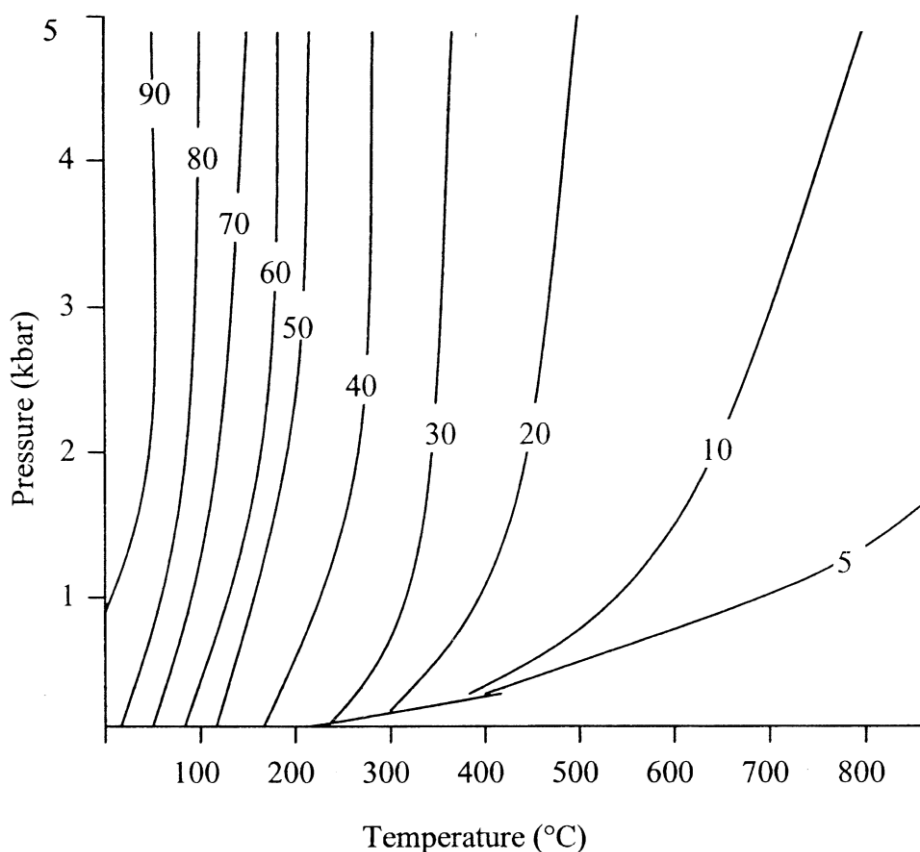


**Figure 2.2** Variation of dielectric constant of water with temperature and pressure [10].

The dielectric constant that is defined as the ability of a solvent to charge separate increases sharply with the pressure in the compressible region that refers to the area around the critical point in which compressibility is considerably greater than would be forecasted from the ideal gas law. This behavior is also parallel to a change in density, as shown in Figure 2.2. Density changes sharply but continuously with pressure in the compressible region. One of the most important advantages of hydrothermal solvents is that a change in density affects the solvating power. A decrease in the density results in a significant change in solvating ability.

The physical and chemical properties of water and aqueous solutions in the temperature and pressure ranges required for hydrothermal synthesis have been discussed in numerous review articles and are well known. The PVT data for water up to 1000°C 10 kbar are known accurately enough (within 1% error) [11]. If the density of water is high enough, nonpolar compounds may be completely miscible with it because water behaves as a nonaqueous fluid. Water is a polar solvent and its polarity can be controlled by temperature and pressure and this can be an advantage over other solvents.

## 2.4 Merits of Hydrothermal Synthesis

Hydrothermal synthesis offers many advantages over conventional and non conventional synthesis methods. Unlike many advanced methods that can prepare a large variety of forms, the respective costs for instrumentation, energy and precursors are far less for hydrothermal methods. From the environmental perspective, hydrothermal methods are more environmentally benign than many other methods. The low reaction temperatures also avoid other problems encountered with high temperature processes (Czochralski method, Bridgeman method) such as poor stoichiometric control due to volatilization of components (e.g. volatilization  $\text{PbO}$  in  $\text{PbWO}_4$ ) and stress-induced defects (e.g. micro-cracks) caused by phase transformations that occur as the phosphor is cooled to room temperature. Moreover, the ability to precipitate the phosphor powders directly from solution regulates the rate and uniformity of nucleation, growth and aging, which affects size, morphology and aggregation control that is not possible with many synthesis processes. Varieties of morphologies and particle sizes possible with hydrothermal processing. This method is beneficial to different industries which rely on powder (e.g. materials, pigments, pharmaceuticals, medical diagnostics) will benefit from having an access to powders with controlled size and morphology for a wide range of reasons. The unique pressure-temperature interaction of the hydrothermal solution allows the preparation of different phases of  $\text{PbWO}_4$  phosphor that are difficult to prepare with other synthetic methods. Phase fields are often simpler when hydrothermal solutions are used. Materials synthesized under hydrothermal conditions often exhibit differences in point defects when compared to materials prepared by high temperature synthesis methods. e.g. Tungstates of Ca, Ba, and Sr synthesized at room temperature by a hydrothermal method do not contain Schottky defects usually present in similar

materials prepared at high temperatures [12] which results in improved luminescent properties.

A major advantage of hydrothermal synthesis is that this method can be hybridized with other processes like microwave, electrochemistry, ultrasound, mechano-chemistry, optical radiation and hot-pressing to gain advantages such as enhancement of reaction kinetics and increase ability to make new materials. A great amount of work has been done to enhance hydrothermal synthesis by hybridizing this method with many other processes. This facile method does not need any seed, catalyst, harmful and expensive surfactant or template thus it is promising for large-scale and low-cost production with high-quality crystals.

## 2.5 Autoclave

Crystal growth under hydrothermal conditions requires a reaction vessel called an *autoclave*. In hydrothermal method highly corrosive salt are used to synthesis inorganic materials for longer reaction time. The Autoclave must be capable of sustaining highly corrosive solvent at high temperature and pressure for a longer duration of time. For selecting a suitable autoclave, the first and foremost parameter is the experimental temperature and pressure conditions and the corrosion resistance in that pressure-temperature range in a given solvent or hydrothermal fluid. In our case as the reaction is taking place directly in the vessel, the corrosion resistance is a prime factor in the choice of the autoclave material. The most successful corrosion resistant materials high-strength alloys, such as 316 series (austenitic) stainless steel, iron, nickel, cobalt-based super alloys, and titanium and its alloys. To avoid corrosion of autoclave material it should coated with non reactive material called Teflon from inside. Due to the larger coefficient of thermal expansion of Teflon (the liner) versus metal (the material in which the liner is enclosed), the Teflon will expand and contract much more upon heating and cooling cycles than its enclosure material.

**An ideal hydrothermal autoclave should have the following characteristics:**

1. Inert to acids, bases and oxidizing agents.
2. It should be easily assemble and dissemble.
3. It should have sufficient length to obtain a desired temperature gradient.
4. It should be leak-proof at desired temperature and pressure.
5. It should bear high pressure and temperature for long duration of time.

## 2.6 Liners

In the hydrothermal experiments, the mineralizer used is highly corrosive and it can react with the vessel, which is inimical to obtaining high purity  $\text{PbWO}_4$  crystals. It requires a suitable lining for the inner wall of the autoclave or separate liners placed in the autoclave. Hence, noble metal lining, liners, or capsules are used successfully for alkaline and neutral media. Studies related to reaction kinetics, solubility and materials processing under mild hydrothermal conditions or pressure temperature conditions below 250 bars and  $300^\circ\text{C}$ , teflon is the most popularly used lining material. Several new autoclave designs with Teflon lining or coating for such studies have been reported in literature. The teflon liner or beaker should sit exactly inside the autoclave without leaving any gap. As the temperature rises, the teflon expands and hermitic sealing can be obtained. The greatest disadvantages of teflon lining is that beyond  $300^\circ\text{C}$ , it cannot be used because teflon dissociates which affects the pH of neutral solutions. This coating tends to get torn and generally must be reapplied after few experiments.

We have designed a Teflon-lined stainless steel autoclave (Figure 2.3) having 90 mL capacity under the guidance of Prof. Diveker (retired Professor from IIT, Bombay) and with the help of Mr. Nitin (Technician, Chemical Engineering department, Faculty of Technology, The M.S.University of Baroda). This reaction vessel was coated with Teflon from inside and possesses a maximum operating temperature  $200^\circ\text{C}$ . To measure the temperature of reaction, Platinum Resistance Thermometer having range  $0\text{-}200^\circ\text{C}$  is used which is purchased by Cliff's Electronics, GIDC, Vadodara. In order to synthesis  $\text{PbWO}_4$ , mixture of Lead salt and Sodium Tungstate salt were taken in precise molar concentration and 80% filled of its

maximum capacity in vessel reactor. Detailed synthesis procedure is explained at the end of this chapter.

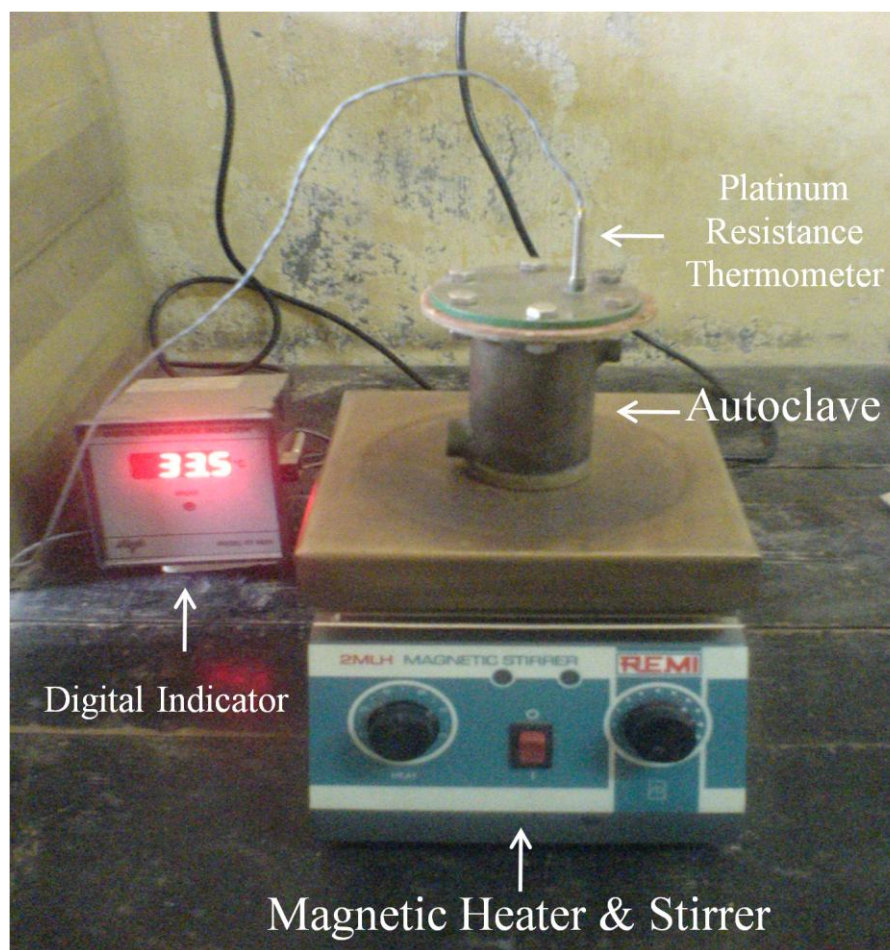


**Figure 2.3** Teflon-Lined Stainless Steel Autoclave.

## 2.7 Effect of Hydrogen on Autoclave

Hydrogen at high temperature and/or pressures can have a disastrous effect on alloys used in autoclaves. It reduces the strength of the autoclaves through any one of the following processes: hydrogen embrittlement, irreversible hydrogen damage, or metal-hydride formation. These problems could be overcome through careful selection of alloys containing small additives such as Ti, Mo, V, heating in H<sub>2</sub> free atmosphere, and using alloys with low thermodynamic activity.

### 2.7.1 Hydrogen embrittlement

Hydrogen is available from the water. Because the hydrogen atom is much smaller in size, it is able to migrate into the crystal lattice of Autoclave metal, and reside interstitially between the individual metal atoms. When these hydrogen atoms recombine in voids of the metal matrix to form hydrogen molecules, they create pressure from inside the cavity they are in. This pressure can increase to levels where the metal has reduced ductility and tensile strength up to the point where it cracks called (*hydrogen induced cracking*, or HIC).

## 2.8 Synthesis

### 2.8.1 Reagents and Solvents

Lead sources [e.g.  $\text{PbCl}_2$ ,  $\text{Pb}(\text{NO}_2)_3$  or  $\text{Pb}(\text{CH}_3\text{COO})_2$  ],  $\text{Na}_2\text{WO}_4 \cdot 2\text{H}_2\text{O}$  and  $\text{CeO}_2$  chemicals are purchased from Alfa Aesar of A.R.(analytical reagent) grade and used without further purification. Distilled water was used as solvent to prepare all required solutions. Acetone and Ethanol were used to wash prepared samples.

### 2.8.2 Procedure

Hydrothermal method used to prepare  $\text{PbWO}_4$  as well as Cerium doped  $\text{PbWO}_4$  nanomaterials with different morphologies are explained here. To produce  $\text{PbWO}_4$  or  $\text{PbWO}_4:\text{Ce}$ , we require different Lead sources [e.g.  $\text{PbCl}_2$ ,  $\text{Pb}(\text{NO}_2)_3$  or  $\text{Pb}(\text{CH}_3\text{COO})_2$  ],  $\text{Na}_2\text{WO}_4 \cdot 2\text{H}_2\text{O}$  and  $\text{CeO}_2$ . All the lead sources are well soluble in distilled water. Initially 30 ml solution of 0.01 M concentration of  $\text{PbX}_2$  [where X= Cl, NO or  $\text{CH}_3\text{COO}$ ] was prepared in distilled water. To prepare 0.01 M concentration of  $\text{PbX}_2$  solution 0.08343 g of  $\text{PbCl}_2$ , 0.0993g of  $\text{Pb}(\text{NO})_2$  or 0.1138g of  $\text{Pb}(\text{CH}_3\text{COO})_2$  is poured in a beaker containing 30ml distilled water with continuous stirring on Magnetic stirrer and Heater. Similarly 30 ml solution of 0.01 M (0.0989 g) concentration of  $\text{Na}_2\text{WO}_4$  was added in it. Instantly precipitates of  $\text{PbWO}_4$  were produced. To prepare Cerium doped  $\text{PbWO}_4$  0.001 M (0.005136 g) concentration of  $\text{CeO}_2$  was added into previously prepared solution. The resulting precursor suspension was transferred to Teflon lined stainless steel autoclave of 90 ml capacity filled 80% with reaction media (i.e. distilled water) one by one. Then the autoclave was

maintained at desired temperature and duration. After achieving required temperature and time for reaction autoclave is air cooled to room temperature. Obtained precipitates were washed and filtered several times with distilled water by using Wattman fine filter papers to remove salt which is produced during reaction. As obtained white precipitates were washed several time with absolute ethanol. To remove water content white powder was dried in vacuum Oven at 80°C for 2h. To understand above procedure simple flow chart is shown in Figure 2.4.

**Hydrothermal Synthesis of Ce doped PbWO<sub>4</sub>**

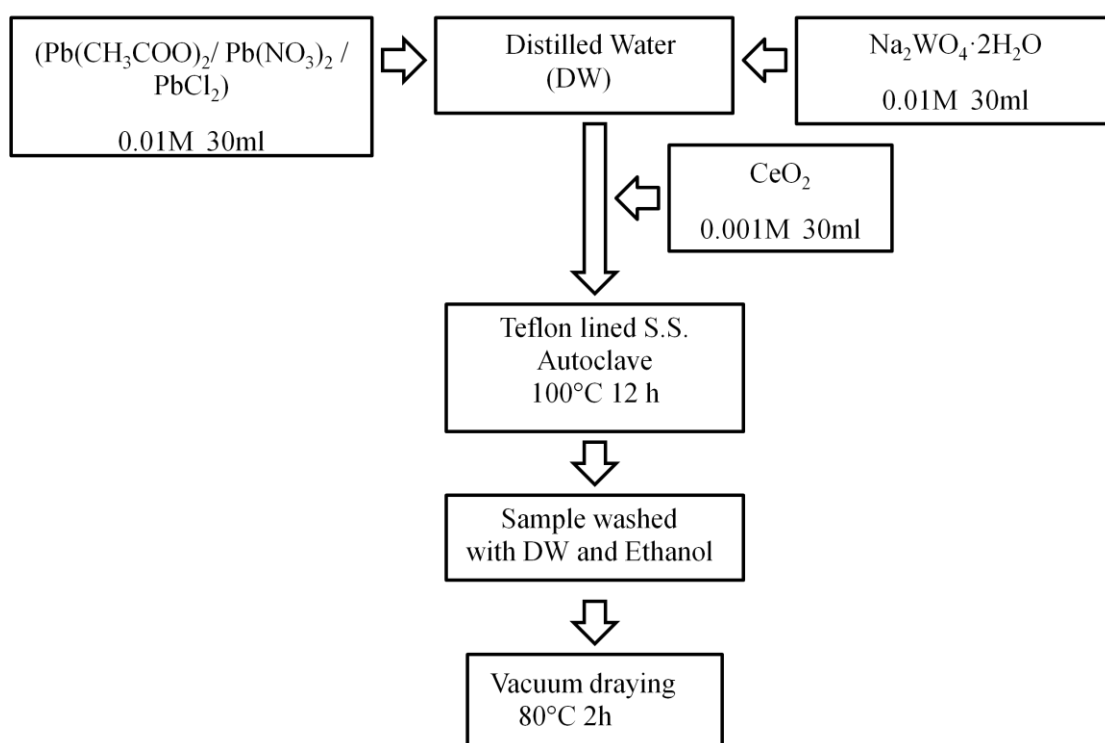


**Figure 2.4** Flow chart of Hydrothermal Synthesis

## 2.9 Summary of Prepared Samples

We have synthesized undoped and Cerium doped  $\text{PbWO}_4$  at different temperatures, with different Lead salts and Cerium concentrations (in molar), at different pH and reaction time in order to study its effect on structural and optical properties. Summary of experiments performed during Ph.D. work is given in following tables.

**Table 2.1**  $\text{PbWO}_4$  and  $\text{PbWO}_4:\text{Ce}$  prepared with different Lead Sources

Sample	Reagent1 conc. (0.01M)	Reagent2 conc. (0.01M)	Dopent conc. (0.001M)	Solvent	Temp. (°C)	Time (h)
1	$\text{Pb}(\text{CH}_3\text{COO})_2$	$\text{Na}_2\text{WO}_4$	-	D.W.	100	12
2	$\text{Pb}(\text{CH}_3\text{COO})_2$	$\text{Na}_2\text{WO}_4$	$\text{CeO}_2$	D.W.	100	12
3	$\text{Pb}(\text{NO}_3)_2$	$\text{Na}_2\text{WO}_4$	-	D.W.	100	12
4	$\text{Pb}(\text{NO}_3)_2$	$\text{Na}_2\text{WO}_4$	$\text{CeO}_2$	D.W.	100	12

**Table 2.2** PbWO<sub>4</sub> and PbWO<sub>4</sub>:Ce prepared at different reaction conditions using Lead Chloride as a Lead Source

Sample No.	PbCl <sub>2</sub> conc. (M)	Na <sub>2</sub> WO <sub>4</sub> conc. (M)	Ce conc. (M)	Temp. (°C)	Time (h)	pH
5	0.01	0.01	-	100	10	7
6	0.01	0.01	0.001	100	10	7
7	0.01	0.01	-	125	10	3
8	0.01	0.01	-	125	10	7
9	0.01	0.01	-	125	10	11
10	0.01	0.01	-	150	10	7
11	0.01	0.01	0.001	150	10	7
12	0.01	0.01	-	200	10	7
13	0.01	0.01	0.001	200	10	7
14	0.01	0.01	0.001	R.T.	10	7

## 2.9 Characterization

Powder X-ray diffraction (XRD) patterns of  $\text{PbWO}_4$  samples which are tabulated in Table 2.1 were recorded at ERDA, Vadodara with a Japan Rigaku D/max-RB diffractometer at a scanning rate of  $3^\circ/\text{min}$  using  $\text{Cu K}\alpha$  radiation ( $\lambda = 0.15406 \text{ nm}$ ). XRD measurements of  $\text{PbWO}_4$  samples which are tabulated in Table 2.2 were carried out using Bruker D8 Advance X-ray diffractometer at UGC-CSR Indore Center. X-rays were produced using a sealed tube and the wavelength of x-ray was  $0.154 \text{ nm}$  ( $\text{Cu K-alpha}$ ). The X-rays were detected using a fast counting detector based on Silicon strip technology (Bruker LynxEye detector). Morphology of as-prepared samples was studied with JEOL JSM-6380LV scanning electron microscopy (FESEM) at ERDA. The microstructure and surface morphology of the microcrystalline powders were observed by transmission electron microscopy (TEM, Tecnai 20 G2 FEI made) at UGC-CSR Indore Center and at SICART, Vidhyanagar. The photoluminescence (PL) of all the samples were investigated on a Shimadzu spectrofluorophotometer at room temperature with Xenon lamp as excitation source at Applied Physics Department, M.S.University of Baroda.

## References

- [1] K. Byrappa, M. Yoshimura, Handbook of Hydrothermal Technology, Noyes Publications, New Jersey, USA, 2001.
- [2] G. W. Morey and P. Niggli, The Hydrothermal Formation of Silicates, A Review, J. Am. Chem. Soc., 35, 1086–1130, 1913.
- [3] R. A. Laudise, The Growth of Single Crystals, pp. 278–281, Prentice-Hall, Englewood Cliffs, NJ, 1970.
- [4] A. Rabenau, The Role of Hydrothermal Synthesis in Preparative Chemistry, Angew. Chem., (English Ed.), 24:1026–1040 (1985).
- [5] A. N. Lobachev, (ed.), Crystallization Processes under Hydrothermal Conditions, pp. 1–255, Consultants Bureau, New York (1973).
- [6] R. Roy, Acceleration the Kinetics of Low-Temperature Inorganic Syntheses, J. Solid State Chem., 111, s11–17, 1994.
- [7] K. Byrappa, (ed.), Hydrothermal Growth of Crystals, pp. 1–365, Pergamon Press, Oxford, UK, 1992.
- [8] M. Yoshimura and H. Suda, Hydrothermal Processing of Hydroxyapatite: Past, Present, and Future, in: Hydroxyapatite and Related Materials (P. W. Brown and B. Constanz, eds.), pp. 45–72, CRC Press, Inc, 1994.
- [9] K. Byrappa and M. Yoshimura, Handbook of Hydrothermal Technology, A Technology for Crystal Growth and Material Processing, Noyes, New Jersey, 2001.
- [10] M. Uematsu, W. Harder and E. U. Franck, The Dielectric Constant of Water, Technical Paper 38p (WLKg. Gp. 3), Int. Assoc. for Prop., of Stern. Inter. Mtg. Kyoto Mtg. Jpn. 1976.
- [11] S.D. Haman, “Properties of electrolyte solutions at high pressures and temperatures”, Physics and Chemistry of the Earth, 13/14, 89, 1981.
- [12] W. S. Cho, M. Yashima, M. Kakihana, A. Kudo, T. Sakata, M. Yoshimura, Appl. Phys. Lett., 66, 1027–1029, 1995.

## 3.1 X-ray Diffraction Analysis (XRD)

### 3.1.1 Introduction

X-rays are high energy electromagnetic radiations having energies ranging from 200 eV to 1MeV, which lies between  $\gamma$ -rays and ultraviolet radiation. Their wavelengths are varying from 10 nm to 1 pm. The useful range of x-rays for diffraction studies is between 0.05 nm to 0.25 nm, which is close to inter-atomic spacing (0.2nm) in crystals. X-rays are produced in an X-ray tube having two metal electrodes (tungsten as cathode and Cu or other metal as anode). Electrons which are produced by heating tungsten filament kept at high negative potential, accelerated towards the anode at ground potential. The loss of energy of the electrons due to impact with the metal anode is manifested as X-rays. Only a small percentage (less than 1%) of energy of the electron beam is converted to X-rays, the majority is dissipated as heat in the water-cooled metal anode.

If the incident electron has sufficient energy to eject an electron from inner-shell, the atom will be left in an excited state with a hole in the electron shell. Suppose this hole is created in innermost K shell and if it is filled by an electron from next outer L shell, an X-ray photon with energy equal to the difference in the electron energy levels is produced. L shell contains three sub shells named  $L_I$ ,  $L_{II}$  and  $L_{III}$ . Transitions from  $L_{III}$ ,  $L_{II}$  to K results emission of  $K\alpha_1$  and  $K\alpha_2$  respectively. If the  $K\alpha_1$  and  $K\alpha_2$  lines cannot be resolved, the characteristic line is simply called the  $K\alpha$  line and the wavelength is given by the weighted average of the  $K\alpha_1$  and  $K\alpha_2$  lines. In our experiment we used Cu source having  $K\alpha_1$  (1.5406 nm) and  $K\alpha_2$  (1.54439 nm) and weighted average of the  $K\alpha_1$  and  $K\alpha_2$  is found to be  $= \frac{1}{3}(2 \times 1.5406 + 1.54439) = 1.54184$  nm.

### 3.1.2 X-ray source

Depending on the target metal, suitable operating voltage is required to knock out K electron. In our work instrument operator used 40 kV operating voltage and 30 mA operating current to produce x-ray from copper (Cu) target.

### 3.1.3 Geometry of X-ray Diffractometer

The three basic components of an x-ray diffractometer are: *x-ray source*, *specimen*, *x-ray detector* and they all lie on the circumference of a circle, which is known as *focusing circle*. The angle between the plane of the specimen and the x-ray source is  $\theta$  called *the Bragg angle* and the angle between the projection of the x-ray source and the detector is  $2\theta$ .

There are four geometries which are used to record X-ray patterns. First geometry is called the  $\theta$ - $2\theta$  geometry in which the X-ray source is fixed and the detector moves through a range of angles. In the second geometry i.e.  $\theta$ - $\theta$  geometry both the X-ray source and the detector moves in the vertical plane in opposite directions above the centre of the specimen. Two more specialized geometries are called  $\omega$  geometry and  $\phi$  geometry, are not widely used although very useful. The *diffractometer circle* also referred to as the *goniometer circle* is centered at the specimen, and both the source and the detector lie on the circumference of the circle. The goniometer is the central component of an x-ray diffractometer and contains the specimen holder. It has arms on which the x-ray source and the detector are mounted.

### 3.1.4 Examination of X-ray diffraction pattern

X-ray diffraction patterns also called reflections which consist of a series of peaks. The peak intensity is plotted on the ordinate (y axis) and the measured diffraction angle,  $2\theta$ , along the abscissa (x axis). Each peak in the diffraction pattern corresponds to X-rays diffracted from a specific set of planes in the specimen, and they are of different heights (intensities). The intensity is proportional to the number of X-ray photons of a particular energy counted by the detector for that particular angle  $2\theta$ . Since it is difficult to measure absolute value of intensity, it is usually expressed in arbitrary units.

The intensities of the reflections depend on several factors i.e. structure factor, incident intensity, slit width and values of operating voltage and current used in the X-ray source. As-recorded X-ray diffraction patterns generally have a background which is usually subtracted and the peaks are smoothed. The positions of the reflections in an X-ray diffraction pattern depend on the crystal structure (shape and size of the unit cell) of the  $\text{PbWO}_4$ . The position of the peak also depends on the wavelength of the X-ray used. The width of an individual peak, often defined as the full width at half the maximum height, can be used to determine crystallite size and the presence of lattice distortions (strain) in the  $\text{PbWO}_4$ . For low values of  $2\theta$  each reflection appears as a single sharp peak. For larger values of  $2\theta$  (above  $80^\circ$ ) each reflection consists of a pair of peaks, which correspond to diffraction of the  $K\alpha_1$  and  $K\alpha_2$  wavelengths. At low  $2\theta$  values of the separation of the peaks is quite small, but increases at larger  $2\theta$  values. The separation of the Cu  $K\alpha_1$  and  $K\alpha_2$  peaks increases from  $0.05^\circ$  at  $20^\circ(2\theta)$  to  $1.08^\circ$  at  $150^\circ(2\theta)$ .

Broadening of X-ray diffraction peaks arises mainly due to three factors:

**1. Instrumental effect:**

These effects include imperfect focusing, unresolved  $\alpha_1$  and  $\alpha_2$  peaks or if these peaks are resolved then their finite width can cause broadening.

**2. Crystallite size:**

The peaks become broader due to the effect of small crystallite sizes, and thus analysis of peak broadening can be used to determine the crystallite size. Small crystallite sizes introduce broadening in addition to broadening due to instrumental effect.

Scherrer has derived an expression for broadening of X-ray diffraction peaks only due to small crystallite sizes:

$$B_{crystallite} = \frac{k\lambda}{L \cos\theta}$$

Where,

$\lambda$  = wavelength of X-ray used

$\theta$  = Bragg angle

k = constant between 0.89 to 1.39

**3. Lattice strain:**

The lattice strain in the material also causes broadening of the diffraction peak, which can be represented by the relationship,

$$B_{strain} = \eta \tan\theta$$

Where,  $\eta$  = strain in the material

## 3.2 Characterization

### 3.2.1 Instruments used to record X-ray spectra

We have done XRD characterization of our samples at two centers: One under UGC-CSR Indore Center, M.P. and Other at ERDA, Vadoadara. The XRD measurements were carried out using Bruker D8 Advance X-ray diffractometer installed at the Indore Centre under UGC Consortium for scientific research facility shown in Figure 3.2.1. The standard sample holder of the diffractometer has a 9 sample changer, making it possible to measure up to 9 samples in as series. The diffractometer uses a 1-D position sensitive detector based on silicon drift detector technique which reduces the measurement time significantly without reduction in the diffracted intensity. The maximum global count rate handled by this detector is  $\sim 10^8$  cps. The inset in the photograph of the XRD system is the sample holder. The X-rays were produced using a sealed tube and the wavelength of X-ray was 0.154 nm (Cu K-alpha). The X-rays were detected using a fast counting detector based on Silicon strip technology (Bruker LynxEye detector).



**Figure 3.2.1** Photograph of XRD instrument at UGC-CSR, Indore Centre

Powder X-ray diffraction (XRD) patterns of some samples were recorded with a Japan RigakuD/max-RB diffractometer (Figure 3.2.2) in Electrical Research and Development Association (ERDA) at Vadodara with a scanning rate of  $3^{\circ}/\text{min}$  using  $\text{Cu K}\alpha$  radiation ( $\lambda = 0.15406 \text{ nm}$ ). The operation voltage and current were fixed at 40 kV and 40mA, respectively.



**Figure 3.2.2** Photograph of XRD instrument at ERDA, Vadodara

### 3.2.2 Analysis of XRD data

Analysis of XRD data was done by “PowdeX” program (available free online or can get by e-mail: [chengdon@aphy.iphy.ac.cn](mailto:chengdon@aphy.iphy.ac.cn) ) provided by Cheng Dong, Institute of Physics, National Laboratory for Superconductivity, Institute of Physics, Chinese Academy of Sciences, Beijing.

### 3.2.3 Procedure to analysis XRD data with PowderX Program

As obtained XRD file was imported to PowderX program.  $K\alpha_2$  elimination was done by DONG’s method. Noise elimination was performed by adaptive smoothing. Background subtraction was performed via Sonneveld method. Lastly Peak search and indexing were done. Path of XRD analysis by PowderX software is shown below.

**Data import →  $K\alpha_2$  elimination → Smoothing → Background Subtraction → Peak Search → Indexing**

## 3.3 X-ray diffraction analysis of $\text{PbWO}_4$

### 3.3.1 Introduction

In order to do systematic analysis, we have divided our experiment in to *two parts*. In the first part of our experiment undoped as well as Cerium doped  $\text{PbWO}_4$  crystals were synthesized with different Lead sources (Lead Acetate, Lead Nitrate and Lead Chloride) using Hydrothermal Method. In the second part of our experiment  $\text{PbCl}_2$  was kept constant as a Lead source and undoped as well as Cerium doped  $\text{PbWO}_4$  crystals were produced by varying reaction temperatures and pH of solution. Effect of different lead sources, reaction temperatures and pH of solution on crystal structure and phase were studied by X-ray diffraction analysis technique. Calculation of lattice parameters, unit cell volume and average crystallite size (using Debey-Scherrer formula) were performed in order to determine crystal structure and phase produced for all samples using PowderX program.

### 3.3.2 Literature Survey

There are hundreds of papers published in which PbO and WO<sub>3</sub> is used as precursor to synthesize large single crystals of PbWO<sub>4</sub> via either Czochralski or Bridgman method. As already discussed in Chapter 1, these methods are expensive and produce harmful gases during crystal growth due to higher synthesis temperature which lowers applicability of these methods for large scale production of PbWO<sub>4</sub> crystals. Moreover, products obtained by these methods are in bulk sized which cannot be used for devices based on nano dimensions. So we have mentioned below only those methods which are effective to produce nanosized PbWO<sub>4</sub> nanomaterial.

According to literature survey, there are 11 papers published on PbWO<sub>4</sub> in which Lead Acetate is used as Lead source to produce PbWO<sub>4</sub> with different morphologies. Out of these eleven papers, 3 papers are based on hydrothermal method [1, 2, 3], 4 papers are based on sonochemical method [4, 5, 6, 7] and 2 paper is based on wet chemical method [8, 9], and two on microemulsion route [10, 11]. In all the published papers mentioned here, pure stolize phase is produced. In our case stolize phase is produced along with raspite phase. Similarly, there are 9 papers published on PbWO<sub>4</sub> in which Lead Nitrate is used as Lead source. Out of these nine papers only one paper is based on hydrothermal route [12], five papers are based on wet chemical method [13, 14, 15, 16, 17], two on microwave assisted method [18, 19], and one paper on microemulsion method [20]. Only one paper by Changhua An [12] had been reported so far in which Lead Chloride is used as Lead source to produce PbWO<sub>4</sub>.

### 3.3.3 Synthesis of $\text{PbWO}_4$ with different Lead Sources

In the first part of experiment various compounds of Lead [ $\text{Pb}(\text{CH}_3\text{COO})_2$ ,  $\text{Pb}(\text{NO}_3)_2$ ,  $\text{PbCl}_2$ ] were used as Lead source and  $\text{Na}_2\text{WO}_4$  was taken as second reagent. Lead sources,  $\text{Na}_2\text{WO}_4 \cdot 2\text{H}_2\text{O}$  and  $\text{CeO}_2$  purchased from Alfa Aesar were analytical reagent grade purity. Distilled water was used as solvent to prepare all required solutions. Initially 30 ml solution of 0.01 M concentration of  $\text{Pb}(\text{CH}_3\text{COO})_2$  was prepared by continuous stirring with magnetic needle in a glass bowl **A**. 30 ml solution of 0.01 M concentration of  $\text{Na}_2\text{WO}_4$  was also prepared separately in another glass bowl **B**. Both these salts are well dissolved in distilled water and produce transparent solutions. Thus prepared solution of  $\text{Na}_2\text{WO}_4$  from the glass bowl **B** is added drop wise in the glass bowl **A**. Instantly white precipitates of  $\text{PbWO}_4$  were formed. In order to dope Cerium, 0.001M solution of  $\text{CeO}_2$  was prepared in third glass bowl **C** and added drop wise to the glass bowl **A**. As prepared solution from the glass bowl **A** was transferred to Teflon Lined Stainless Steel Autoclave and filled upto 80% of its maximum capacity. Autoclave was put on hot plate to achieve desired temperature and time of reaction. After achieving required temperature and time for reaction autoclave is air cooled to room temperature. Obtained white precipitates were washed several times with absolute ethanol and filtered with Wattman fine filter papers to remove unwanted extra salt. After removing unwanted salt, to remove the water content, white powder was dried in vacuum oven at  $80^\circ\text{C}$  for 2h. Similar products were also obtained by using  $\text{Pb}(\text{NO}_3)_2$  and  $\text{PbCl}_2$  as Lead sources. Preparation conditions and chemical reactions of above experiment are given below in tabulated form in Table 3.1. XRD reflection spectra of thus obtained samples are shown in Figure 3.3.1 and Figure 3.3.2.

The reaction processes can be expressed as follow:

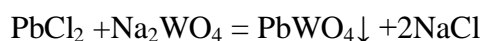
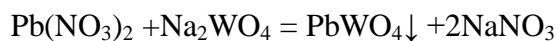
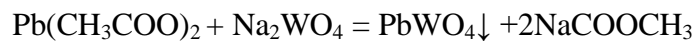


**Table 3.1** Summary of reaction conditions to synthesize  $\text{PbWO}_4$  and  $\text{PbWO}_4:\text{Ce}$  using different Lead sources.

Sample	Reagent1 conc. (0.01M)	Reagent2 conc. (0.01M)	Dopant conc. (0.001M)	Solvent	Temp. (°C)	Time (h)
1	$\text{Pb}(\text{CH}_3\text{COO})_2$	$\text{Na}_2\text{WO}_4$	-	D.W.	100	12
2	$\text{Pb}(\text{CH}_3\text{COO})_2$	$\text{Na}_2\text{WO}_4$	$\text{CeO}_2$	D.W.	100	12
3	$\text{Pb}(\text{NO}_3)_2$	$\text{Na}_2\text{WO}_4$	-	D.W.	100	12
4	$\text{Pb}(\text{NO}_3)_2$	$\text{Na}_2\text{WO}_4$	$\text{CeO}_2$	D.W.	100	12
5	$\text{PbCl}_2$	$\text{Na}_2\text{WO}_4$	-	D.W.	100	12
6	$\text{PbCl}_2$	$\text{Na}_2\text{WO}_4$	$\text{CeO}_2$	D.W.	100	12

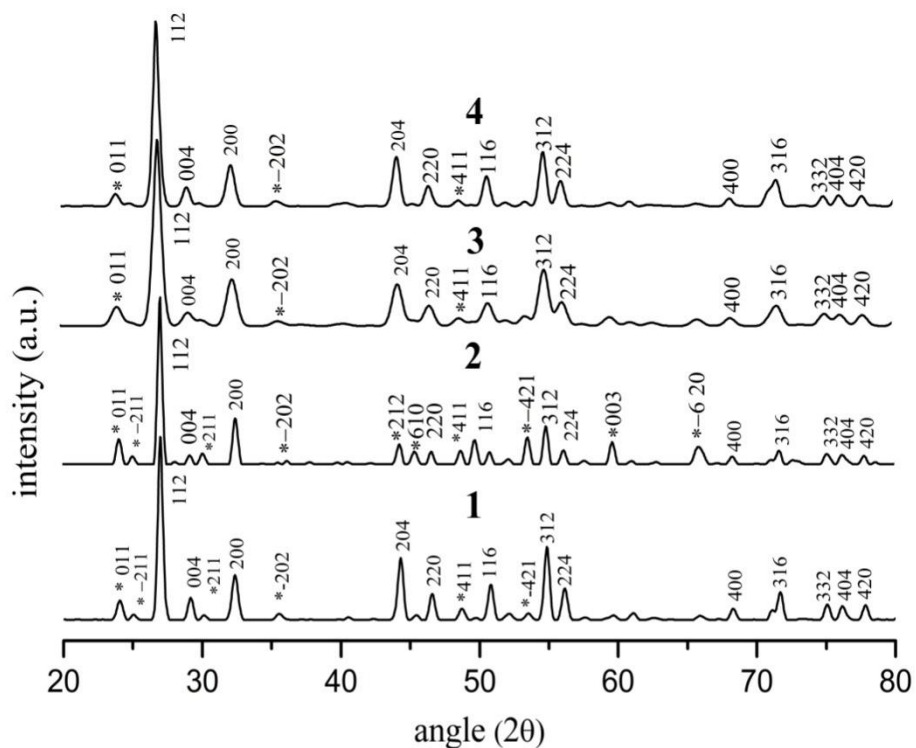


**Figure 3.3.1** XRD reflections of undoped and Cerium doped  $\text{PbWO}_4$  synthesized using Lead Acetate (1, 2) and Lead Nitrate (3,4).

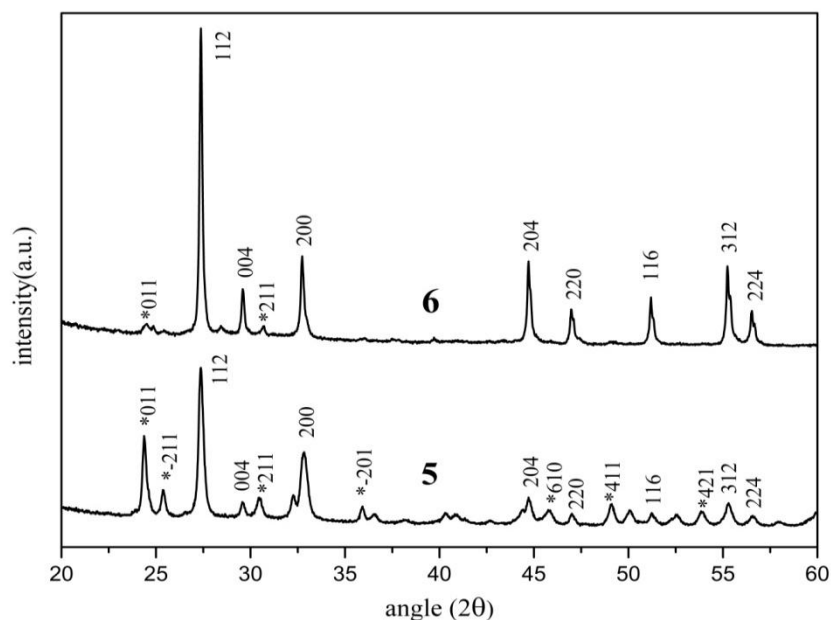


**Figure 3.3.2** XRD reflections of undoped and Cerium doped  $\text{PbWO}_4$  synthesized using Lead Chloride (5,6).

**Table 3.2** Summary of phase, lattice parameters, unit cell volume and average crystallite size of undoped and Cerium doped PbWO<sub>4</sub>.

Sample No.	Reagent 1 conc. (0.01M)	Reagent 2 conc. (0.01M)	Dopant conc. (0.001M)	Phase	Lattice Parameter (Å)			Volume (Å) <sup>3</sup>	Average Crystallite size (nm)
					a	b	c		
1	Pb(CH <sub>3</sub> COO) <sub>2</sub>	Na <sub>2</sub> WO <sub>4</sub>	-	stolzite	5.5890	5.5890	12.030	375.78	19.08
				raspite	13.655	4.9760	5.5601	375.08	
2	Pb(CH <sub>3</sub> COO) <sub>2</sub>	Na <sub>2</sub> WO <sub>4</sub>	CeO <sub>2</sub>	stolzite	5.5730	5.5730	12.028	373.56	18.60
				raspite	13.555	4.9750	5.5601	374.95	
3	Pb(NO <sub>3</sub> ) <sub>2</sub>	Na <sub>2</sub> WO <sub>4</sub>	-	stolzite	5.6445	5.6445	12.047	383.82	19.89
				raspite	13.580	4.9900	5.5600	376.76	
4	Pb(NO <sub>3</sub> ) <sub>2</sub>	Na <sub>2</sub> WO <sub>4</sub>	CeO <sub>2</sub>	stolzite	5.5478	5.5478	12.025	370.10	19.45
				raspite	13.561	4.9770	5.5610	375.32	
5	PbCl <sub>2</sub>	Na <sub>2</sub> WO <sub>4</sub>	-	stolzite	5.4637	5.4637	12.042	359.47	28.27
				raspite	13.561	4.9760	5.5601	375.19	
6	PbCl <sub>2</sub>	Na <sub>2</sub> WO <sub>4</sub>	CeO <sub>2</sub>	stolzite	5.4630	5.4630	12.040	359.32	42.81
				raspite	13.530	4.977	5.5610	374.47	

### 3.3.4 Effect of Lead Sources

Figure 3.3.1 shows typical X-ray diffraction pattern of as synthesized  $\text{PbWO}_4$  (samples 1 and 3) and Cerium doped  $\text{PbWO}_4$  (samples 2 and 4) in which  $\text{Pb}(\text{CH}_3\text{COO})_2$  and  $\text{Pb}(\text{NO}_3)_2$  were used as Lead sources, respectively. Similarly, Figure 3.3.2 shows X-ray diffraction pattern of  $\text{PbWO}_4$  (sample 5) and cerium doped  $\text{PbWO}_4$  (sample 6) in which  $\text{PbCl}_2$  was used as a Lead source. Both Figures are recorded with different instruments at different scanning rate, hence shown separately. The peak intensity is plotted on the ordinate (y axis) and the diffraction angle,  $2\theta$ , along the abscissa (x axis). Each peak also called *reflection*, in the diffraction pattern corresponds to X-ray diffracted from a specific set of planes of  $\text{PbWO}_4$  crystal lattice. Each reflection has different intensity (rather relative intensity) which is proportional to the number of X-ray photons of a particular energy counted by detector for each angle  $2\theta$ .

X-ray reflection spectra (Figure 3.3.1 and Figure 3.3.2) reveals that all prepared samples are polycrystalline in nature and contains two phases of  $\text{PbWO}_4$ . All X-ray diffraction peaks were indexed to a tetragonal scheelite (stolzite) phase with space group  $I4_1/a$  and monoclinic raspite phase with space group  $P2_1/a$ . The peaks representing raspite phase are marked with symbol (\*) for all samples. The formation of Tungstic acid ( $\text{H}_2\text{WO}_4 \cdot n\text{H}_2\text{O}$ ), other tungsten oxide hydrates ( $\text{WO}_3 \cdot n\text{H}_2\text{O}$ ) and unwanted impurity of  $\text{Na}_2\text{WO}_4$ ,  $\text{Ce}_2(\text{WO}_4)_3$ ,  $\text{PbO}$ , and  $\text{Pb}(\text{OH})_2$  were not observed. Calculation of lattice parameters, unit cell volume and average crystallite size were performed for individual sample using Scherrer formula with the help of PowderX software and given in Table 3.2. The highest relative intensity is obtained for (1 1 2) crystallographic plane of tetragonal crystal structure or stolzite phase.

As discussed in Chapter 1, in the tetragonal stolzite structure, W atoms are in tetrahedral O-atom cages and isolated from each other, whereas in monoclinic raspite structure, two W atoms share two O atoms to form a chain of edge-shared octahedra. Each Pb ion is surrounded by seven O ions in the raspite structure, whereas in the scheelite structure, the number of the surrounding O ions to each Pb ion is eight. The monoclinic form of  $\text{PbWO}_4$  (raspите-type) can be considered as a distortion of the tetragonal form of  $\text{PbWO}_4$  (scheelite-type). As raspite phase is transform irreversibly to stolzite phase at higher temperature, high temperature solid state reactions produce  $\text{PbWO}_4$  crystals having pure stolzite phase. XRD data analysis confirms the presence of raspite phase in all the samples. This indicates that at low temperature raspite phase is produced predominantly and with increase in temperature it transforms irreversibly into stolzite phase. Hence some inclusions of raspite phase are still present at 100°C reaction temperature denoted by (\*).

Using  $\text{Pb}(\text{CH}_3\text{COO})_2$  as a Lead source, large amount of raspite phase was produced when compared to  $\text{Pb}(\text{NO}_3)_2$  and  $\text{PbCl}_2$ . It should be noted that  $\text{PbWO}_4$  prepared with Lead Chloride contains least amount of raspite phase inclusions. Efforts are made to find the reason for the well observed raspite phase due to  $\text{Pb}(\text{CH}_3\text{COO})_2$  required more experimental evidence.

Comparing Figure 3.3.1 and Figure 3.3.2, it is observed that among all, sample 5 and sample 6 shows high crystallinity. Hence Lead Chloride proved to be better Lead source to produce high crystalline  $\text{PbWO}_4$  crystals over Lead Nitrate and Lead Acetate.

XRD reflection spectra also confirm that Cerium doping in  $\text{PbWO}_4$  does not distort its characteristic shape. No other impurities such as  $\text{Ce}_2(\text{WO}_4)_3$ ,  $\text{PbO}$  and  $\text{Pb}(\text{OH})_2$  can be observed and it reveals that the doping of  $\text{Ce}^{3+}$  at different temperatures does not change the crystal structure or induce a new phase. The  $\text{Ce}^{3+}$  ions are likely to enter  $\text{PbWO}_4$  crystal lattice to substitute  $\text{Pb}^{2+}$  sites considering that the ion radius of  $\text{Ce}^{3+}$  (0.103 nm) is similar to that of  $\text{Pb}^{2+}$  (0.120 nm) [21]. Figure 3.3.2 shows that intensity of raspite phase peaks are greatly suppressed by Cerium doping. This type of peak suppression is not observed in Figure 3.3.1. Reason of this interesting phenomenon is not clear but we can simply conclude that Cerium act as catalyst and helps raspite phase to convert into stolzite phase when Lead Chloride was used as Lead source.

The volumes of the unit cells of these two structures are very close; the difference is less than 0.53% which can be seen from Table 3.2. Range of unit cell volume for stolzite phase is 359.47-383.83 ( $\text{\AA}^3$ ) and that is for raspite phase is 359.09-375.32 ( $\text{\AA}^3$ ). The average crystallite sizes were estimated by the Scherrer's equation using the full width at half maximum (FWHM) of the most intense peak (1 1 2). The average crystallite size calculated using the Debye-Scherrer formula given in the literature [21], described as follows,

$$D = \frac{k\lambda}{\beta \cos \theta}$$

Where D is the average crystallite size or particle size, k is the constant equal to 0.94,  $\lambda$  is the wavelength of the X-rays equal to 0.1542 nm,  $\theta$  is the Bragg angle and  $\beta$  is FWHM. Value of average crystallite size are smaller for  $\text{PbWO}_4$  prepared using Lead Acetate and Lead Nitrate compared to that of prepared using Lead Chloride. Due to small crystallite size, the number of parallel planes available is too small for a sharp diffraction maximum to build up and hence the reflection peaks in the diffraction

pattern becomes broadened for sample 1 to 4 (Figure 3.3.1) while it is sharp for sample 5 and 6 (Figure 3.3.2). Cerium doping reduce the crystallite size in the case of  $\text{Pb}(\text{CH}_3\text{COO})_2$  or  $\text{Pb}(\text{NO}_3)_2$  while it is increase in the case of  $\text{PbCl}_2$  as a Lead source.

According to the Bragg equation, the shift of reflection peaks towards higher angle suggests the decrease in lattice parameter of as-synthesized products. In order to confirm this we have magnified scale of characteristic reflection peak (112) of all  $\text{PbWO}_4$  samples and compare the shift with calculated lattice parameter in Table 3.2.

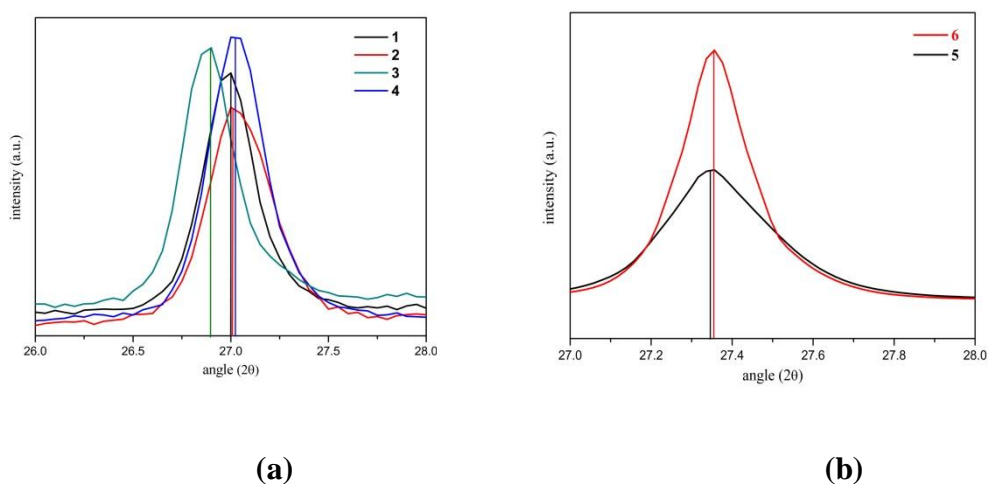


**Figure 3.3.3** Magnified (112) reflection peak of (a) Sample 1-4 (b) Sample 5-6

Figure 3.3.3 (a) and (b) are the images of characteristic (112) reflection peak of  $\text{PbWO}_4$  on magnified scale. In Figure 3.3.3 (a) and (b) peak position of Cerium doped samples (2, 4 and 6) are shifted to higher angle compared to that of undoped sample (1, 3 and 5). The shift of reflection peaks towards higher angle suggests the decrease in lattice parameter can be seen in Table 3.2. As already mentioned  $\text{Ce}^{3+}$  substitute well  $\text{Pb}^{2+}$  in  $\text{PbWO}_4$  lattice and induce  $\text{Pb}^{2+}$  vacancy in order to keep the charge neutral. The substitution of  $\text{Ce}^{3+}$  ion with ionic radius (0.103 nm) is slightly smaller than that of  $\text{Pb}^{2+}$  (0.120 nm) [22] which also explain our result reported [23, 24].

### 3.4 Lead Chloride as a Lead Source

Lead Chloride ( $\text{PbCl}_2$ ) is an inorganic compound which is a white solid under ambient conditions. Lead Chloride is one of the most important lead-based reagents. It also occurs naturally in the form of the mineral *cotunnite*.

In the first part of our experiment we observed that  $\text{PbWO}_4$  with highest crystallinity can be formed by using  $\text{PbCl}_2$  as a Lead source. It is also expected that alkali halide compounds produce good luminescence will see in Chapter 5. As mentioned earlier, only one literature is available in which  $\text{PbWO}_4$  were synthesized using  $\text{PbCl}_2$  is reported till today. These are the some points which encourage us to do systematic research in this direction which is presented in below sections.

#### 3.4.1 Reaction parameters

In this part of experiment Lead Chloride ( $\text{PbCl}_2$ ) was used as Lead source and remaining reagents and synthesis procedure were kept similar to that of previous part.  $\text{PbWO}_4$  synthesized at different Temperature and by varying pH of solvent, taking 0.01 M concentration of  $\text{PbCl}_2$ ,  $\text{Na}_2\text{WO}_4$  and 0.001M concentration of  $\text{CeO}_2$ . All these experiments in which Lead Chloride was used as Lead source are summarized and tabulated in Table 3.3.

**Table 3.3** PbWO<sub>4</sub> and PbWO<sub>4</sub>: Ce prepared at different reaction conditions using Lead Chloride as a Lead source.

Sample No.	PbCl <sub>2</sub> conc. (M)	Na <sub>2</sub> WO <sub>4</sub> conc. (M)	Ce conc. (M)	Temp. (°C)	Time (h)	pH
5	0.01	0.01	-	100	10	7
6	0.01	0.01	0.001	100	10	7
7	0.01	0.01	-	125	10	3
8	0.01	0.01	-	125	10	7
9	0.01	0.01	-	125	10	11
10	0.01	0.01	-	150	10	7
11	0.01	0.01	0.001	150	10	7
12	0.01	0.01	-	200	10	7
13	0.01	0.01	0.001	200	10	7
14	0.01	0.01	0.001	R.T.	10	7

### 3.5 Effect of pH of reaction solution on PbWO<sub>4</sub>

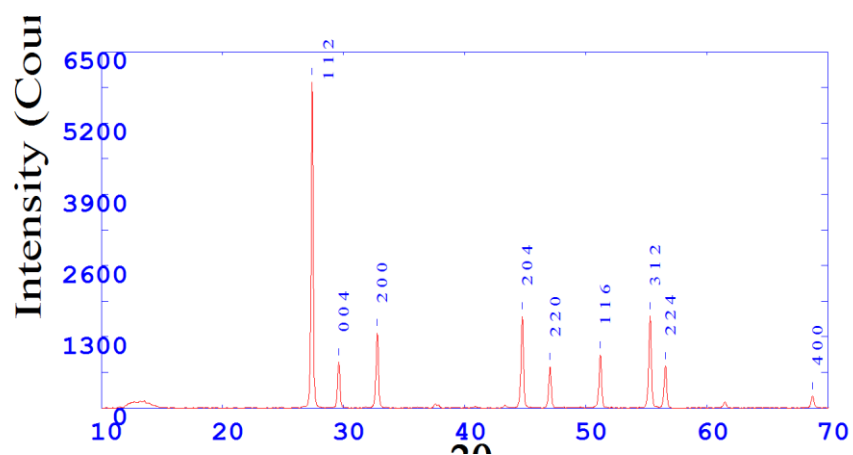
The pH of reaction system is one of the most important factors. It has been found that the pH value of the precursor medium plays an important role in the formation of tungstate phase and their morphology. Controlled experiments were carried out to investigate the influence of pH on the synthesis of PbWO<sub>4</sub>.

To study the effects of pH of solvent on structural properties of PbWO<sub>4</sub> was prepared with 3pH, 7pH and 11pH and they denoted by sample **7**, **8** and **9** as shown in Table 3.4. During preparation of sample 7, pH of distilled water was set to 3 by adding Acetic acid (Glacial) (CH<sub>3</sub>COOH) drop wise while pH of distilled water was increased up to 11 by adding Sodium Hydroxide (NaOH) for sample 9. In all this experiments temperature was kept at 125° C and synthesis time was kept for 10 h.

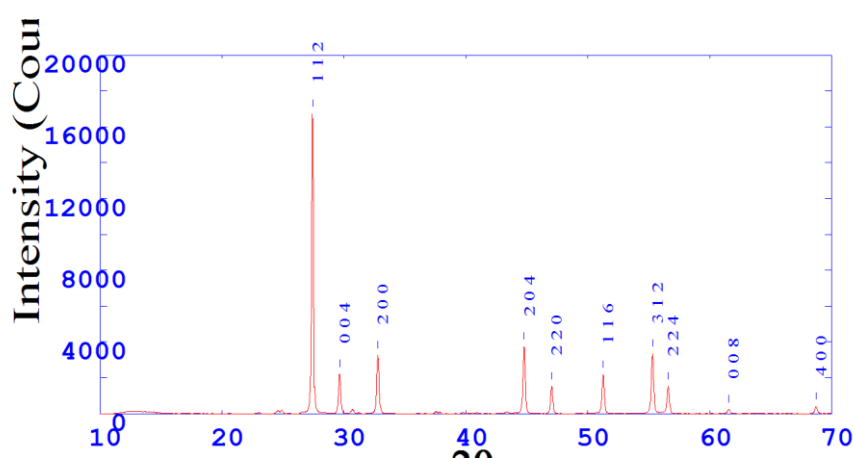
**Table 3.4** PbWO<sub>4</sub> prepared with different pH of reaction solution

Sample	PbCl <sub>2</sub> conc. (M)	Na <sub>2</sub> WO <sub>4</sub> conc. (M)	Temp. (°C)	Time (h)	pH
<b>7</b>	0.01	0.01	125	10	3
<b>8</b>	0.01	0.01	125	10	7
<b>9</b>	0.01	0.01	125	10	11

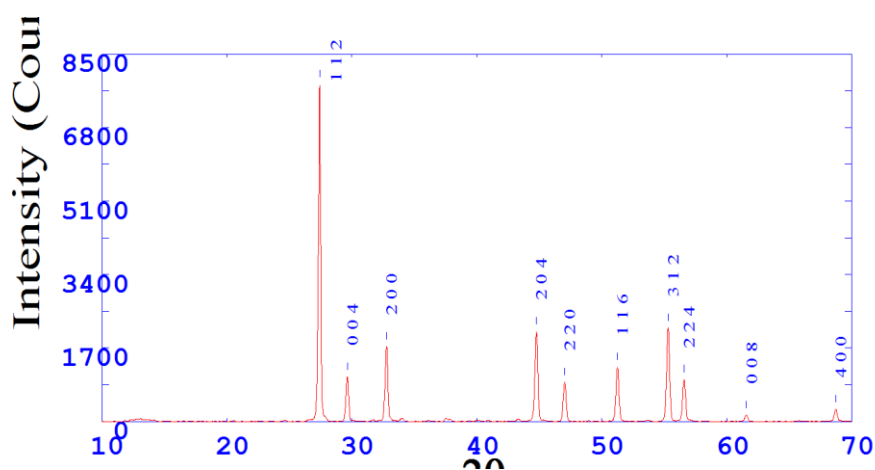
Figure 3.5.1 (a), (b) and (c) shows the XRD pattern of PbWO<sub>4</sub> powders synthesized at different pH 3, 7 and 11, respectively. The XRD data files for these samples are treated with by PowderX software and Indexed images are shown below.



(a) 3pH



(b) 7pH



(c) 11pH

**Figure 3.5.1** Indexed XRD reflections of  $\text{PbWO}_4$  synthesized at (a) 3pH, (b) 7pH and (c) 11pH. (Images from PowderX program)

It can be seen from the Figure 3.5.1 (a), (b) and (c) that  $\text{PbWO}_4$  synthesized at different pH of reaction solution is a single phase. All the reflection peaks can be completely indexed to a pure tetragonal stolzite phase of  $\text{PbWO}_4$  with space group  $I4_1/a$ . The formation of Tungstic acid  $\text{H}_2\text{WO}_4 \cdot n\text{H}_2\text{O}$ , other tungsten oxide hydrates  $\text{WO}_3 \cdot n\text{H}_2\text{O}$  and unwashed impurity of  $\text{Na}_2\text{WO}_4$  washed not observed. XRD results indicate that the powders are free of secondary phases. The strong and sharp peaks indicate that the  $\text{PbWO}_4$  powders processed in 3pH, 7pH and 11pH are highly crystallized and structurally ordered at long-range. This result shows that the different pH promotes the formation of crystalline  $\text{PbWO}_4$  powders at low synthesis temperature and reduced processing time than the other conventional methods.

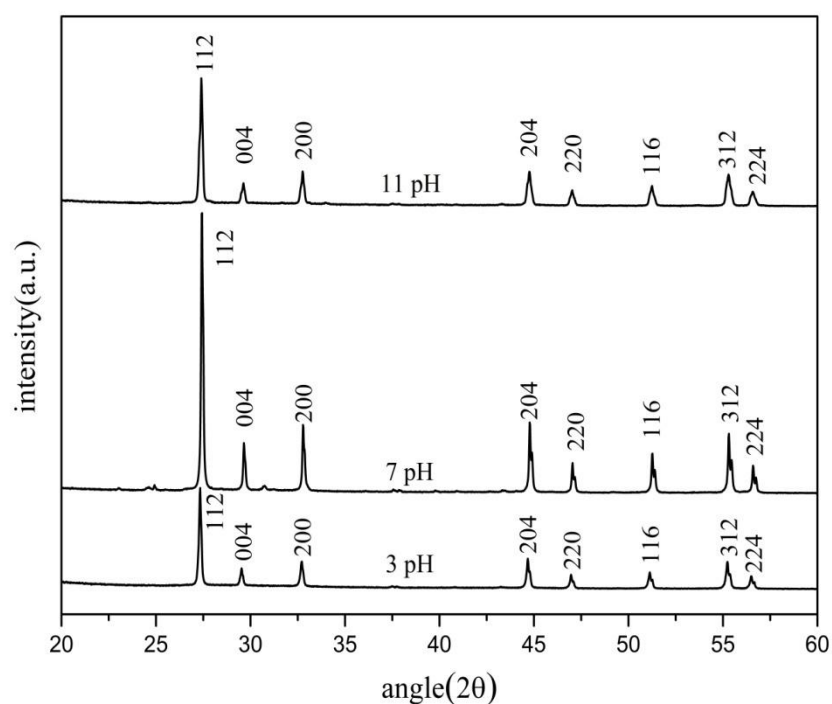


**Figure 3.5.2** XRD pattern of  $\text{PbWO}_4$  prepared at different pH

However, on comparing the XRD spectra of three samples (see Figure 3.5.2), we found that the relative intensity of the peaks varied significantly, which indicates different percentage of crystallinity. Highest crystallization observed for  $\text{PbWO}_4$  prepared at 7pH and lowest crystallization observed for  $\text{PbWO}_4$  prepared at 3pH. Samples prepared at 7pH and 11pH show better crystallization than the one made at 3pH.

According to Jun Geng et al. [25], 5-9 pH range is optimal for production of  $\text{PbWO}_4$  with different morphologies. If the pH value is higher than 11, another complex,  $\text{Pb}(\text{OH})_x^{2-x}$ , was formed due to the high concentration of  $\text{OH}^-$  and the strong complexing ability between  $\text{Pb}^{2+}$  and  $\text{OH}^-$ . In this case, no product of  $\text{PbWO}_4$  could be obtained. But our result shows that  $\text{PbWO}_4$  nanomaterials with good crystallinity can be formed even at 11pH and optimal pH range is 3-11 pH.

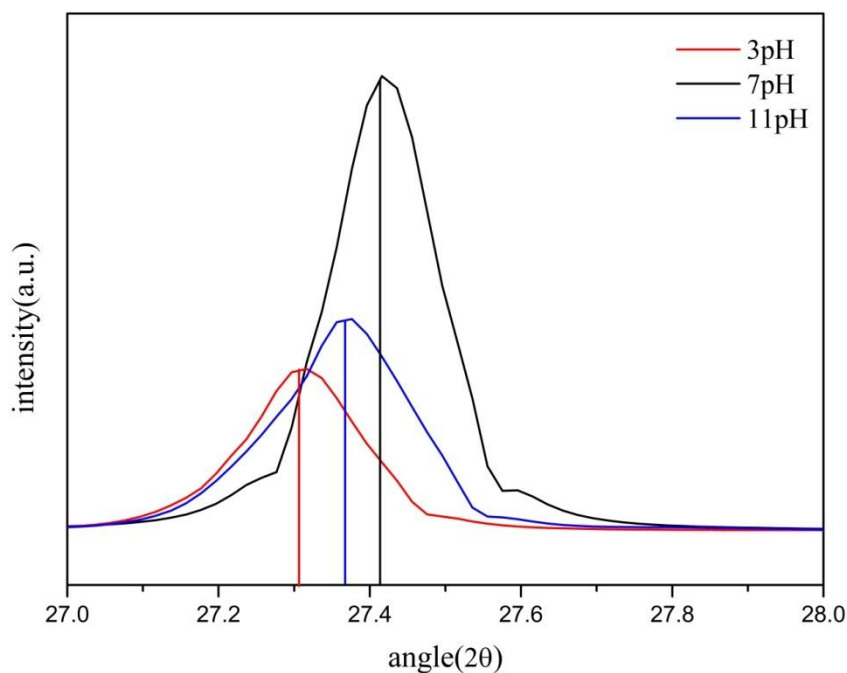


**Figure 3.5.3** Shift of (112) reflection peak of  $\text{PbWO}_4$  prepared at different pH.

Shift in the main reflection peak (112) of stolzite phase of  $\text{PbWO}_4$  is compared and shown in Figure 3.5.3. It can be seen from the figure that (112) peak for sample prepared at 3 pH is at lowest angle and that of for sample prepared at 7pH is at highest angle. According to the Bragg equation, the shift toward higher angle of reflection peaks suggested that the cell parameters of as-synthesized products could continuously decrease. By observing the variation of PowderX calculated lattice parameters for all three sample (Table 3.5) verification of this rule can be done.

**Table 3.5** Summary of phase identified, lattice parameters, unit cell volume and average crystallite size of  $\text{PbWO}_4$  prepared at different pH.

Sample	pH	Phase	Lattice Parameter (Å)			Volume (Å) <sup>3</sup>	Average Crystallite size (nm)
			a	b	c		
7	3	stolzite	5.4614	5.4614	12.046	359.29	40.75
8	7	stolzite	5.4590	5.4590	12.042	358.85	44.75
9	11	stolzite	5.4598	5.4598	12.045	359.05	35.45

### 3.6 Effect of synthesis Temperature on $\text{PbWO}_4$

Temperature is another most important reaction parameter which controls the crystal structure and morphology of the product. Hydrothermal method is used to produce high crystalline samples at lower synthesis temperature compared to other high temperature solid state reaction. In Hydrothermal method product is in polycrystalline form while High temperature methods are used to produce large single crystals. Low temperature formation of highly crystalline powder products could be used in nano-functional devices.

To study the effect of reaction temperature on crystal structure and phase formation of  $\text{PbWO}_4$ , samples were synthesized at four different temperatures: 100°C, 125°C, 150°C and 200°C and symbolized as sample 5, 8, 10 and 12, respectively. Preparation condition of sample 5, 8, 10 and 12 are given in Table 3.6.

**Table 3.6**  $\text{PbWO}_4$  synthesized at different reaction temperatures.

Sample	$\text{PbCl}_2$ conc. (M)	$\text{Na}_2\text{WO}_4$ conc. (M)	Ce conc. (M)	Temp. (°C)	Time (h)	pH
5	0.01	0.01	-	100	10	7
8	0.01	0.01	-	125	10	7
10	0.01	0.01	-	150	10	7
12	0.01	0.01	-	200	10	7

The XRD reflection spectra of  $\text{PbWO}_4$  synthesized at different temperatures are shown in Figure 3.6.1. As mentioned earlier, all XRD reflection peaks are indexed to a tetragonal scheelite (stolzite) phase with space group  $I4_1/a$  and monoclinic raspite phase with space group  $P2_1/a$ . The identification of raspite phase peaks for all samples are marked with symbol (\*). The formation of Tungstic acid  $\text{H}_2\text{WO}_4 \cdot n\text{H}_2\text{O}$ , other tungsten oxide hydrates  $\text{WO}_3 \cdot n\text{H}_2\text{O}$  and unwanted impurity of  $\text{Na}_2\text{WO}_4$ ,  $\text{Ce}_2(\text{WO}_4)_3$ ,  $\text{PbO}$ , and  $\text{Pb}(\text{OH})_2$  were not observed. XRD spectra of sample 5,10 and 12 indicates the presence of secondary raspite phase of  $\text{PbWO}_4$  while sample 8 is free of secondary phase and contains pure stolzite phase.

Comparing XRD graph of  $\text{PbWO}_4$  samples prepared at  $100^\circ\text{C}$ ,  $125^\circ\text{C}$ ,  $150^\circ\text{C}$  and  $200^\circ\text{C}$  following observations can be done.  $\text{PbWO}_4$  prepared at  $100^\circ\text{C}$  temperature contains highest amount of raspite phase compared to samples prepared at  $150^\circ\text{C}$  and  $200^\circ\text{C}$  temperatures. With increase of temperature from  $100^\circ\text{C}$  to  $200^\circ\text{C}$  percentage of raspite phase of  $\text{PbWO}_4$  decreases. Among all the samples prepared at different temperatures, pure stolzite phase produced only for sample prepared at  $125^\circ\text{C}$  with highest crystallinity. However, on comparing the XRD peaks of the products, we found that the relative intensity of the peaks varied significantly, indicate that at different temperature  $\text{PbWO}_4$  with different crystallinity form. Thus different reaction temperature in our experiment would bring about significant changes in the crystallization of stolzite phase of  $\text{PbWO}_4$ .

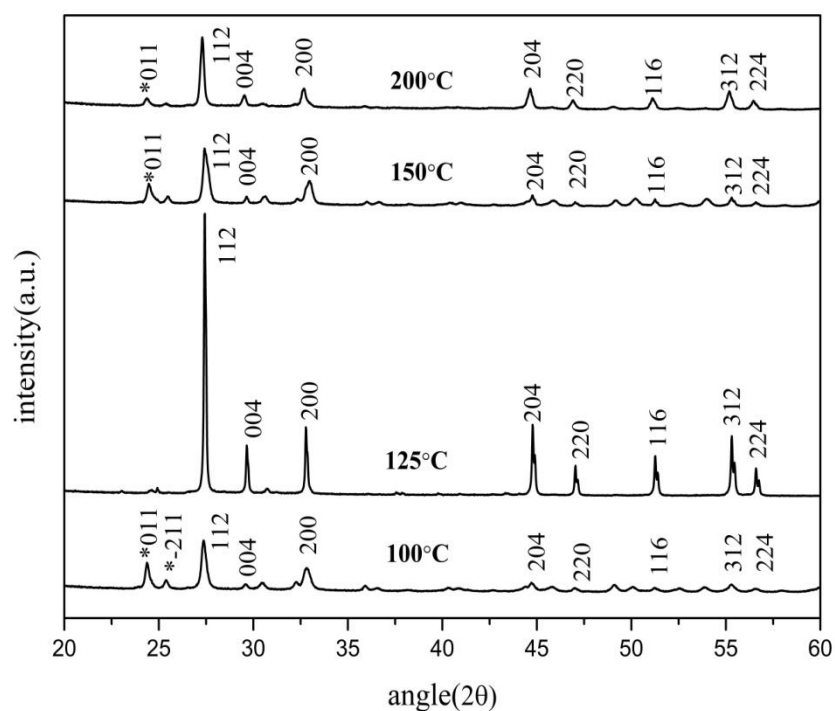


**Figure 3.6.1** XRD pattern of  $\text{PbWO}_4$  prepared at different Temperature.

**Table 3.7** Summary of phase identified, lattice parameters, unit cell volume and average crystallite size of  $\text{PbWO}_4$  prepared at different Temperature.

Sample	Temp. (°C)	Phase	Lattice Parameter(Å)			Volume (Å) <sup>3</sup>	Average crystallite size (nm)
			a	b	c		
5	100	stolzite	5.4637	5.4637	12.042	359.48	28.27
		raspite	13.561	4.976	5.5601	375.09	
8	125	stolzite	5.4598	5.4598	12.042	358.96	44.75
10	150	stolzite	5.4584	5.4584	12.057	359.23	24.76
		raspite	13.496	4.985	5.579	375.34	
12	200	stolzite	5.4602	5.4602	12.049	359.23	36.32
		raspite	13.552	4.985	5.563	375.82	

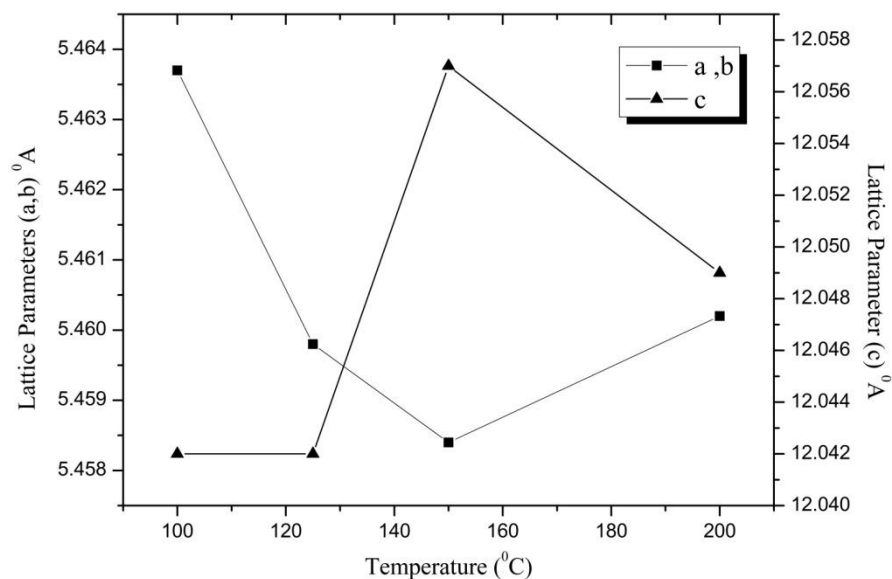


**Figure 3.6.2** Effect of synthesis Temperature on Lattice Parameters of  $\text{PbWO}_4$

We have plot the graph which shows the variation of lattice parameters of stolzite phase as a function of Temperature. Figure 3.8 shows graph of Temperature verses lattice parameter by taking the values tabulated in Table 3.7. As we can see from the table that, all  $\text{PbWO}_4$  samples except prepared at 125 °C, exhibit little amount of raspite phase. Lattice parameter (a, b) is highest for sample prepared at 100 °C which decreases with increase in temperature up to 150 °C and again increase for sample prepared at 200°C. While lattice parameter (c) remains constant for sample prepared at 100 °C to125 °C and increase and become maximum for 150 °C then again decrease for sample prepared at 200°C.

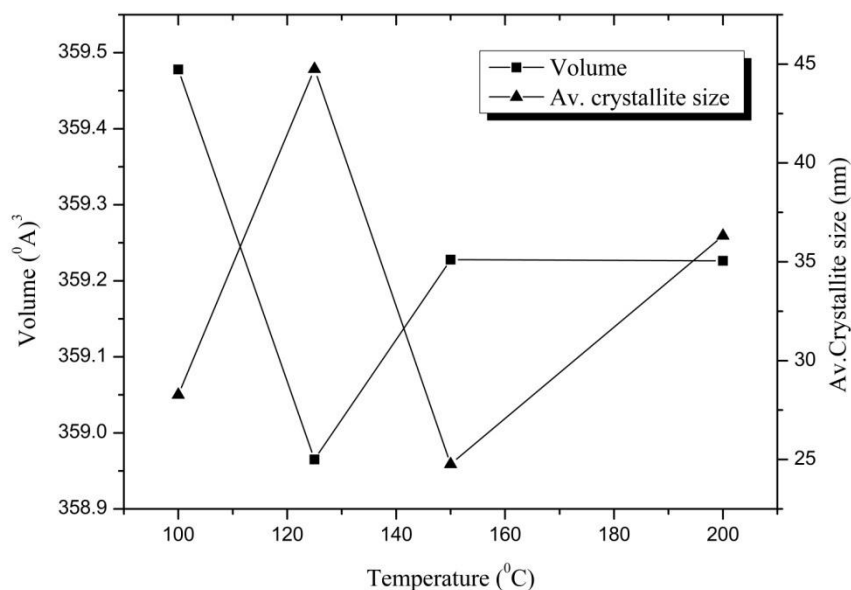


**Figure 3.6.3** Effect of synthesis Temperature on Volume and Average Crystallite size of PbWO<sub>4</sub>

We have also plot the graph which shows the variation of unit cell volume and average crystallite size as a function of Temperature. Figure 3.6.3 shows the graph of Temperature verses unit cell volume and average crystallite size by taking the values tabulated in Table 3.7. Unit cell volume is highest for sample prepared at 100 °C which decreases with increase in temperature up to 125 °C and again increase for sample prepared at 150°C. This behavior can be associated with aggregates production and nuclei formation [27], promoting the expansion of cell volume. Unit cell volume then remains constant up to 200 °C. While average crystallite size is highest for sample prepared 125 °C and decrease for 150 °C then again increase for sample prepared at 200°C. From the graphs we can conclude that unit cell volume is inversely proportional to average crystallite size.

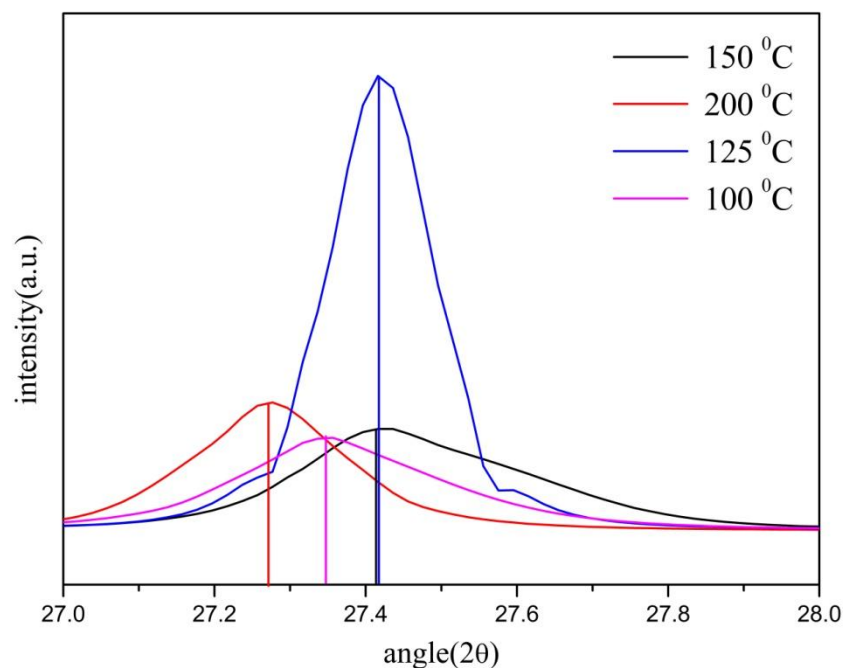


**Figure 3.6.4** Shift of (112) peak of PbWO<sub>4</sub> synthesized at different temperature

Figure 3.6.4 shows the shift of reflection peak (112) for different temperature towards higher angle suggests that the cell parameters of as-synthesized products could decrease with Ce<sup>3+</sup> doping. The peak position of the PbWO<sub>4</sub> samples synthesized at 125°C and 150°C is almost same so lattice parameters of these samples should close to each other and smaller than the sample prepared at 100°C and 200°C. This can be verified by values given in Table 3.7.

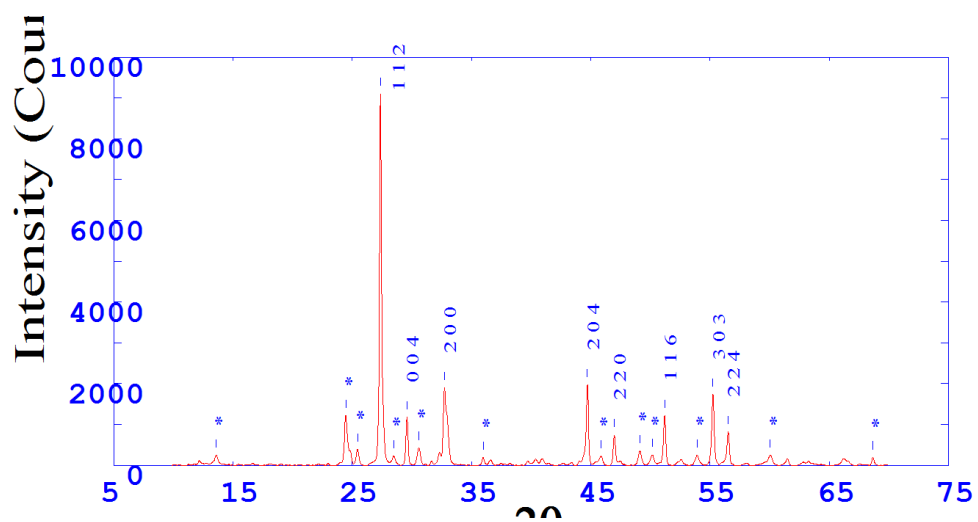
### 3.7 Effect of synthesis Temperature on PbWO<sub>4</sub>:Ce

To study the effect of reaction temperature on crystal structure and phase formation of Cerium doped PbWO<sub>4</sub>, PbWO<sub>4</sub> phosphor synthesized at room temperature, 100°C, 150°C and 200°C temperatures were selected and symbolized as sample 6, 11, 13 and 14, respectively. Preparation conditions for sample 6, 11, 13 and 14 are given in Table 3.8.

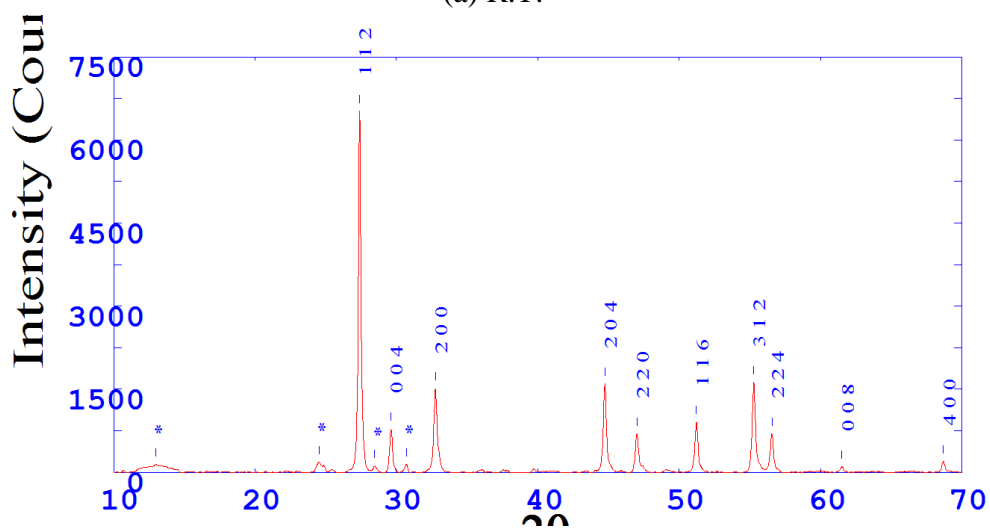
**Table 3.8** PbWO<sub>4</sub>:Ce synthesized at different reaction temperatures.

Sample	PbCl <sub>2</sub> conc. (M)	Na <sub>2</sub> WO <sub>4</sub> conc. (M)	Ce conc. (M)	Temp. (°C)	Time (h)	pH
<b>6</b>	0.01	0.01	0.001	100	10	7
<b>11</b>	0.01	0.01	0.001	150	10	7
<b>13</b>	0.01	0.01	0.001	200	10	7
<b>14</b>	0.01	0.01	0.001	R.T.	10	7

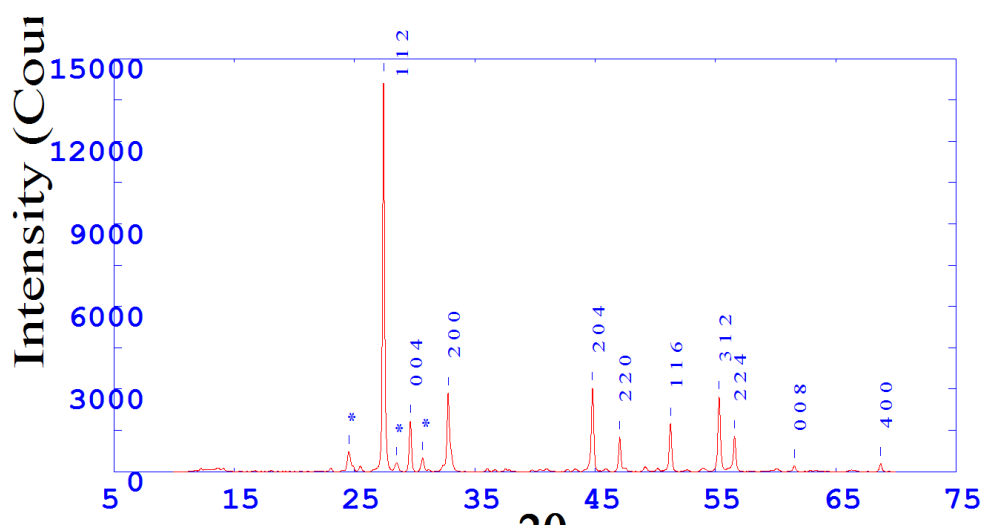
XRD reflection spectra of Cerium doped samples synthesized at room temperature, 100°C, 150°C and 200°C temperatures are refined with PowderX software and shown in Figure 3.7.1 (a), (b), (c) and (d). All XRD reflection peaks are indexed to a tetragonal scheelite (stolzite) phase with space group I4<sub>1</sub>/a and monoclinic raspite phase with space group P2<sub>1</sub>/a. The identification of raspite phase peaks for all samples are marked with symbol (\*). The formation of Tungstic acid H<sub>2</sub>WO<sub>4</sub>.nH<sub>2</sub>O, other tungsten oxide hydrates WO<sub>3</sub>.nH<sub>2</sub>O and unwashed impurity of Na<sub>2</sub>WO<sub>4</sub> Ce<sub>2</sub>(WO<sub>4</sub>)<sub>3</sub>, PbO and Pb(OH)<sub>2</sub> were not observed in all the samples.



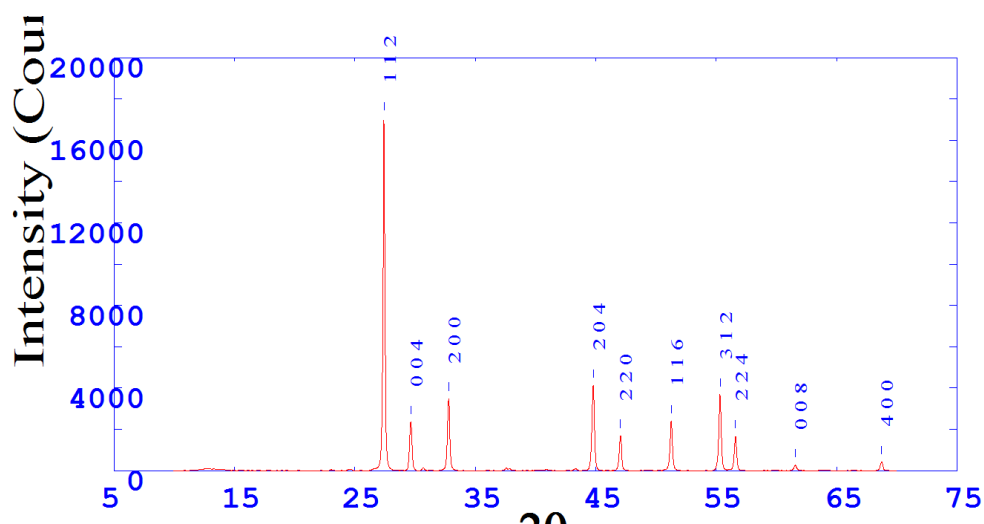
(a) R.T.



(b) 100°C



(c) 150°C



(d) 200°C

**Figure 3.7.1** Indexed XRD spectra of PbWO<sub>4</sub>:Ce synthesized at (a) R.T. (b) 100°C (c)150°C and (d) 200°C.

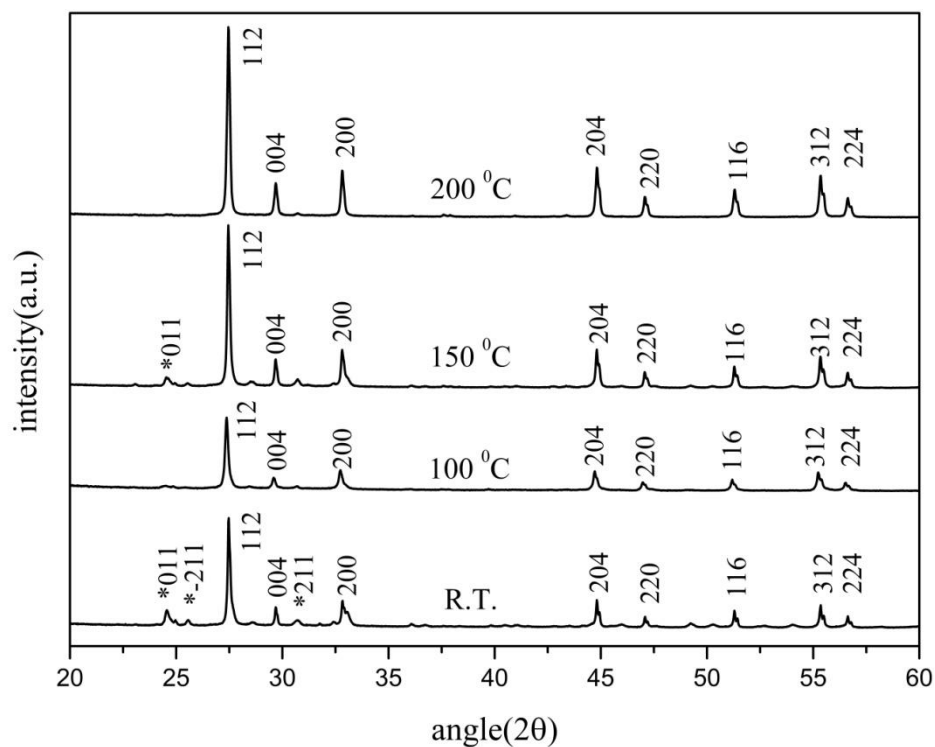


**Figure 3.7.2** XRD pattern of PbWO<sub>4</sub>:Ce prepared at different Temperature

**Table 3.9** Summary of phase identified, lattice parameters, unit cell volume and average crystallite size of  $\text{PbWO}_4\text{:Ce}$  prepared at different Temperature.

Sample	Temp. (°C)	Phase	Lattice Parameter(Å)			Volume (Å) <sup>3</sup>	Average crystallite size (nm)
			a	b	c		
6	100	stolzite	5.4630	5.4630	12.051	359.65	42.81
		raspite	13.561	4.977	5.561	375.33	
11	150	stolzite	5.4595	5.4595	12.042	358.92	47.82
		raspite	13.555	4.976	5.561	375.09	
13	200	stolzite	5.4596	5.4596	12.042	358.94	46.78
14	R.T.	stolzite	5.4692	5.4692	12.064	360.86	46.77

As we can see from the PowderX refined XRD reflections that relative intensity of XRD peaks are increases as temperature increases from 100°C to 200°C. However, on comparing the intensities of the products, we found that the relative intensity of the peaks varied significantly, which indicates that at different temperature  $\text{PbWO}_4$  with different crystallinity form. On doping with Cerium in  $\text{PbWO}_4$ , intensity of peaks representing raspite phase decreases, which means that doping of cerium also decrease the amount of raspite phase with increase in temperature. XRD spectra of  $\text{PbWO}_4\text{:Ce}$  crystals prepared at 200°C temperature shows raspite free pure stolzite phase. Among all the samples prepared at different temperatures, sample prepared at 200°C is highest crystalline in nature. Intensity of peaks representing stolzite phase also increases with Cerium which can be seen from XRD reflections. These results indicate that along with Temperature, Cerium also plays an important role to increase crystallinity.

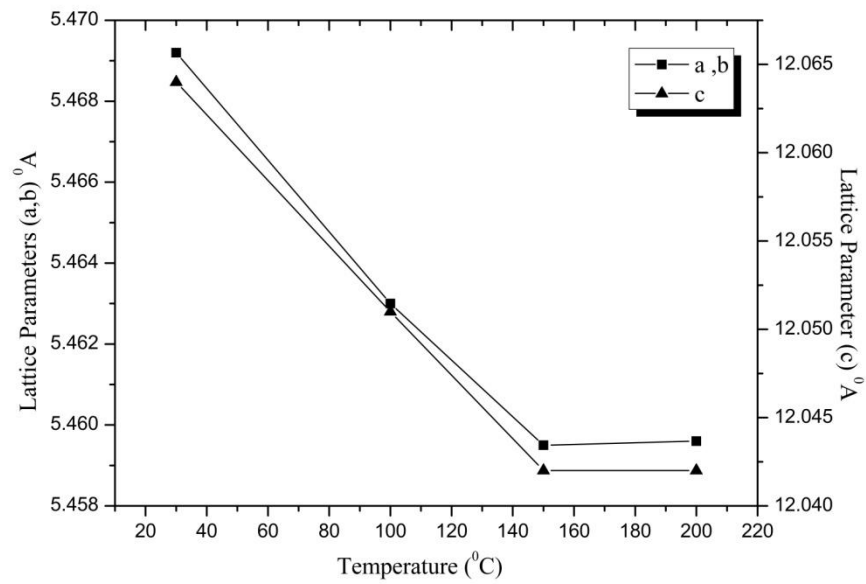


**Figure 3.7.3** Effect of synthesis Temperature on Lattice Parameters of  $\text{PbWO}_4:\text{Ce}$

We have plot the graph which shows the variation of lattice parameter as a function of Temperature for Cerium doped  $\text{PbWO}_4$  synthesized at different temperature. Figure 3.7.3 shows the graph of Temperature verses Lattice parameter by taking the values tabulated in Table 3.9. As we can see from the table that, all  $\text{PbWO}_4$  samples except prepared at 200 °C exhibit little amount of raspite phase. Lattice parameter (a,b) is highest for sample prepared at room temperature which decreases with increase in temperature up to 150 °C and then remains constant up to 200°C. Lattice parameter (c) also follows the same behaviour. Lattice parameter (c) is also highest for sample prepared at room temperature which decreases with increase in temperature up to 150 °C and then remains constant up to 200°C. Possible explanation for this can be given as follow. At room temperature nucleation and crystal growth occurs at very low temperature and so at room temperature Cerium was not able to replace  $\text{Pb}^{2+}$ . With increase in temperature more amount of  $\text{Ce}^{3+}$  ions substitute well  $\text{Pb}^{2+}$  ions in

$\text{PbWO}_4$  lattice and induce  $\text{Pb}^{2+}$  vacancy in order to keep the charge neutral. As ionic radius of  $\text{Ce}^{3+}$  ion is 0.103 nm which is slightly smaller than that of  $\text{Pb}^{2+}$  (0.120 nm). Hence with substitution of  $\text{Ce}^{3+}$  ion at  $\text{Pb}^{2+}$  site which increases with increase in temperature lattice parameter are decreases with increase in temperature.

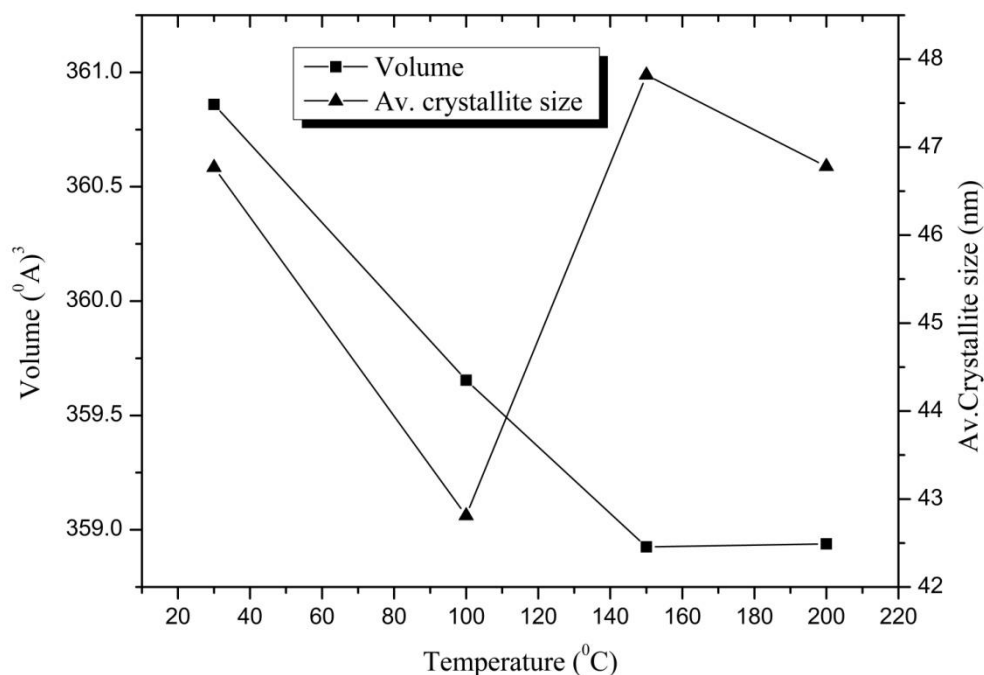


**Figure 3.7.4** Effect of synthesis Temperature on Volume and Average Crystallite size of  $\text{PbWO}_4:\text{Ce}$

We have also plot the graph which shows the variation of unit cell volume and average crystallite size as a function of Temperature. Figure 3.7.4 shows graph of Temperature verses unit cell volume and average crystallite size by taking the values tabulated in Table 3.9. Unit cell volume is highest for sample prepared at room temperature which decreases with increase in temperature up to 150 °C and then remains constant up to 200 °C. This can explain only the basis of substitution of  $\text{Ce}^{3+}$  ion on  $\text{Pb}^{2+}$  site decrease lattice parameters and hence unit cell volume. Average crystallite size is lowest for sample prepared 100 °C and almost remains same for

remaining samples. It well known that increase of temperature promotes a raise in the average crystallite size or particle size [25].

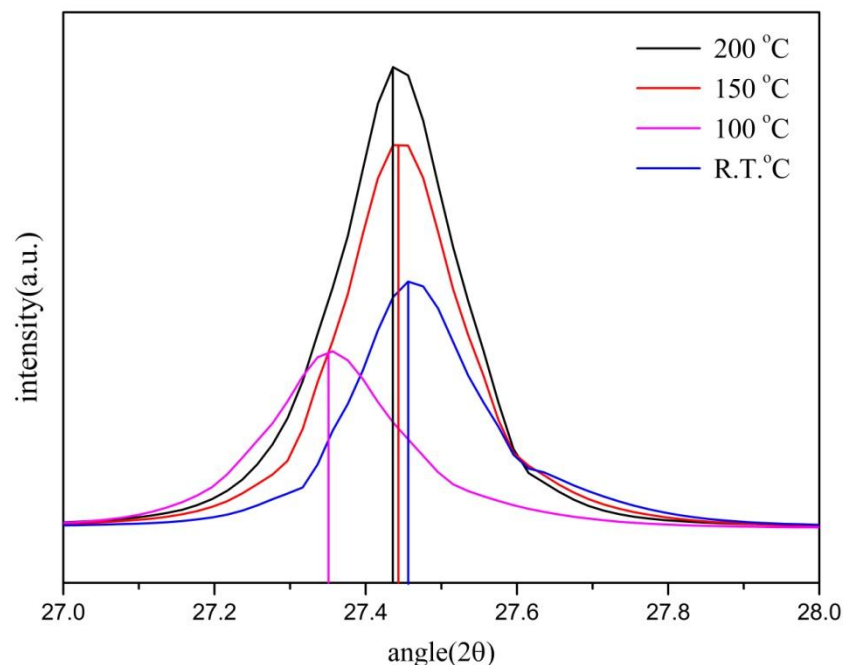


**Figure 3.7.5** Shift of (112) peak of PbWO<sub>4</sub>:Ce synthesized at different temperature

Figure 3.7.5 shows the shift of reflection peak (112) for different temperature towards higher angle suggests that the cell parameters of as-synthesized products could decrease with Ce<sup>3+</sup> doping. The peak position of the PbWO<sub>4</sub>: Ce samples synthesized at room temperature, 150°C and 200°C is almost same so lattice parameters of these samples should close to each other and smaller than the sample prepared at 100°C. This can be verified by values given in Table 3.9.

### 3.8 Effect of Cerium doping on structural properties of PbWO<sub>4</sub>

There is only one report has been done on structural and optical properties of Cerium doped PbWO<sub>4</sub> by Yan Fang et al using wet chemical method [8]. Very few literatures are available in which affect of Ce<sup>3+</sup> doping on luminescence property of PbWO<sub>4</sub> reported but effect of Ce<sup>3+</sup> doping on crystal structure at different temperature is not reported till date. We have already discussed the effect Ce<sup>3+</sup> at different temperatures. In this section comparison of XRD spectra of undoped and Cerium doped PbWO<sub>4</sub> at three individual 100°C, 150°C and 200°C temperatures is done. The XRD reflection spectra of undoped and Cerium doped PbWO<sub>4</sub> synthesized different temperatures are shown in Figure 3.8.1.

All XRD reflection peaks are indexed to a tetragonal scheelite (stolzite) phase with space group I4<sub>1/a</sub> and monoclinic raspite phase with space group P2<sub>1/a</sub>. The identification of raspite phase peaks for all samples are marked with symbol (\*). The formation of Tungstic acid H<sub>2</sub>WO<sub>4</sub>.nH<sub>2</sub>O, other tungsten oxide hydrates WO<sub>3</sub>.nH<sub>2</sub>O and unwashed impurity of Na<sub>2</sub>WO<sub>4</sub>, Ce<sub>2</sub>(WO<sub>4</sub>)<sub>3</sub>, PbO, and Pb(OH)<sub>2</sub> were not observed, which reveals that the doping of Ce<sup>3+</sup> at different temperatures does not change the crystal structure or induce a new phase.

Comparing XRD graphs of undoped and Cerium doped PbWO<sub>4</sub> samples prepared at 100°C, 150°C and 200°C following observations can be derived. Sample prepared at 100°C temperature contains highest amount of raspite phase compared to samples prepared at 150°C and 200°C temperatures. With increase of temperature from 100°C to 200°C percentage of raspite phase of PbWO<sub>4</sub> decreases. This indicates that at higher temperature stolzite phase with Tetragonal crystal structure dominates over raspite phase with monoclinic structure. In another words with increase in

temperature probability of raspite phase to convert into stolzite phase irreversibly increases. Conversion from raspite to stolzite is completed at 200°C temperatures and single phase  $\text{PbWO}_4$  is produced.

It is also inferred from the XRD spectra that with Cerium doping, intensity of peaks representing raspite phase decreases and intensity of peaks representing stolzite phase increases. This behaviour is observed in all the samples for all the temperatures. Thus we can conclude that along with temperature doping of cerium also play an important role to decrease the amount of raspite phase and increase the amount of stolzite phase with increase in temperature.

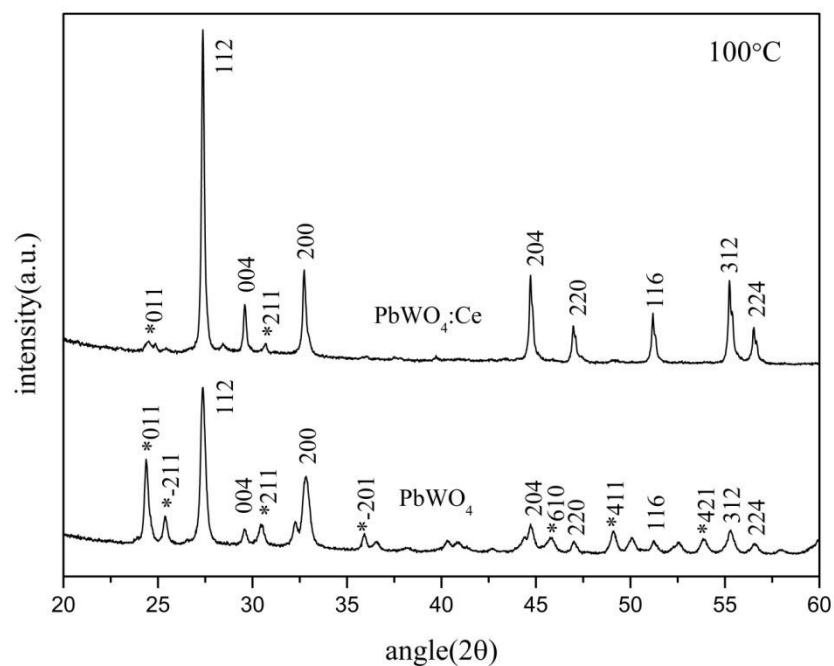


**Figure 3.8.1** XRD spectra of  $\text{PbWO}_4$  and  $\text{PbWO}_4:\text{Ce}$  synthesized at 100°C.

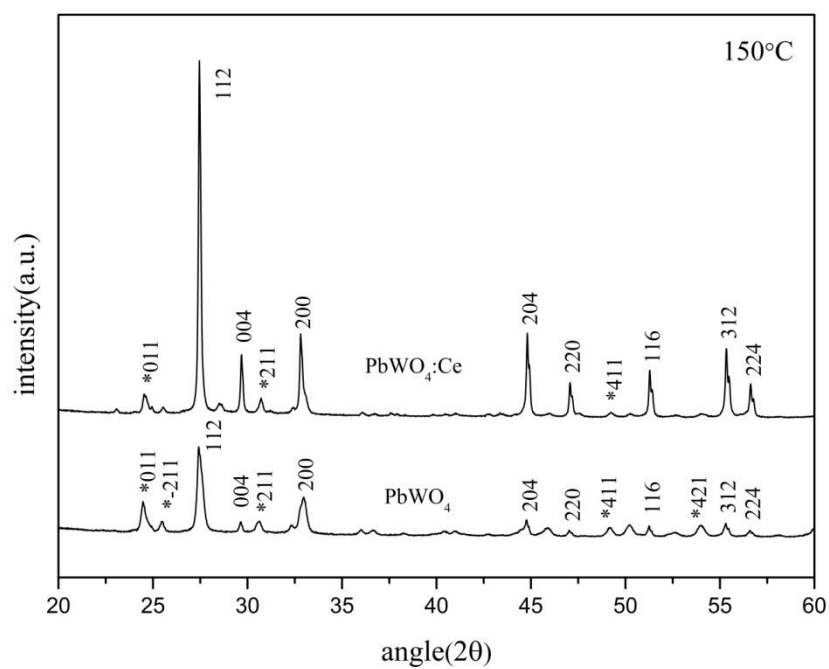


Figure 3.8.2 XRD spectra of PbWO<sub>4</sub> and PbWO<sub>4</sub>:Ce synthesized at 150°C.

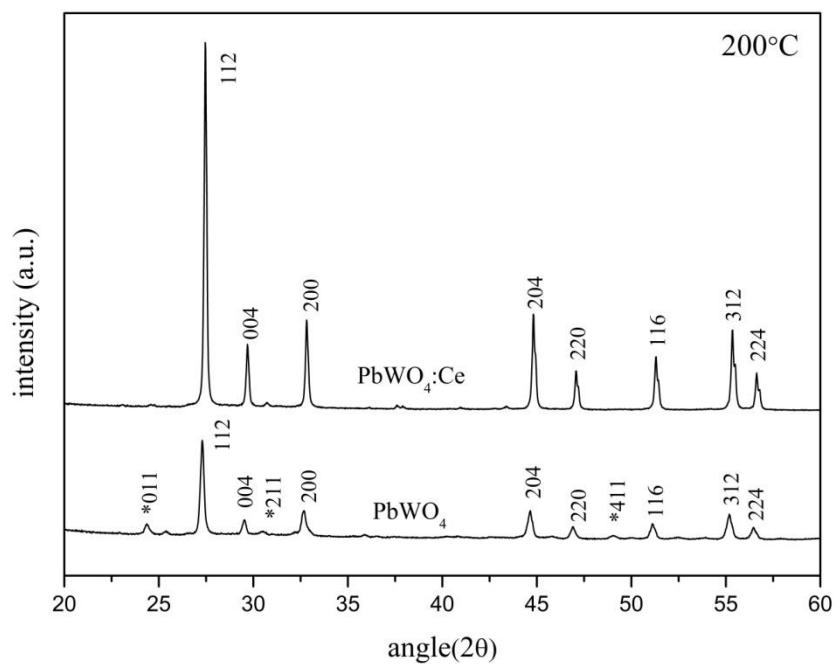
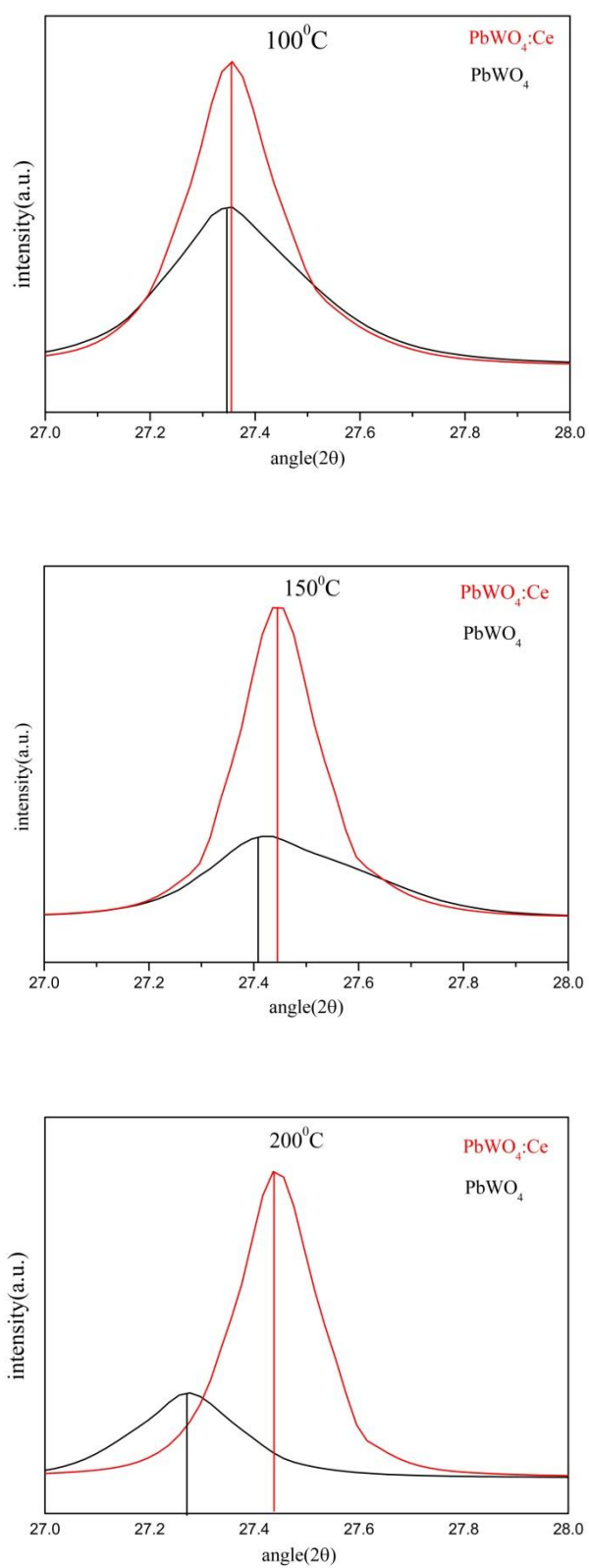


Figure 3.8.3 XRD spectra of PbWO<sub>4</sub> and PbWO<sub>4</sub>:Ce synthesized at 200°C

**Table 4.0** Summary of phase identified, lattice parameters, unit cell volume and average crystallite size of undoped and Cerium doped  $\text{PbWO}_4$  prepared at different Temperature.

Temp (°C)	Product	Phase	Lattice Parameter (Å)			Volume (Å) <sup>3</sup>	Average crystallite size (nm)
			a	b	c		
100	$\text{PbWO}_4$	stolzite	5.4637	5.4637	12.051	359.74	28.27
		raspite	13.561	4.977	5.561	375.09	
	$\text{PbWO}_4\text{:Ce}$	stolzite	5.4630	5.4630	12.042	359.38	42.81
		raspite	13.555	4.976	5.556	375.33	
150	$\text{PbWO}_4$	stolzite	5.4595	5.4595	12.057	359.37	24.76
		raspite	13.496	4.985	5.579	375.34	
	$\text{PbWO}_4\text{:Ce}$	stolzite	5.4584	5.4584	12.042	358.78	47.82
		raspite	13.555	4.976	5.561	375.09	
200	$\text{PbWO}_4$	stolzite	5.4602	5.4602	12.049	359.23	36.32
		raspite	13.552	4.985	5.563	375.82	
	$\text{PbWO}_4\text{:Ce}$	stolzite	5.4596	5.4596	12.042	358.94	46.78



**Figure 3.8.4** Shift of (112) peak of undoped and Cerium doped  $\text{PbWO}_4$  prepared at different Temperature.

The cell parameters, unit cell volume and average crystallite size of undoped and Cerium doped  $\text{PbWO}_4$  crystals for different temperatures were also investigated and the results are listed in Table 4.0. It is found from the table that the values of lattice parameters decreased and average crystallite size increase more than 50% with the introduction of Cerium for all the temperatures. Incorporation of Cerium in to  $\text{PbWO}_4$  host lattice also decreases the unit cell volume. The appearance of these interesting phenomena is previously discussed and attributed: firstly due to the substitution  $\text{Ce}^{3+}$  for  $\text{Pb}^{2+}$  in the  $\text{PbWO}_4$  crystal lattice induced the formation of  $\text{Pb}^{2+}$  vacancies to keep the charge neutral. Secondly, the ion radius of  $\text{Ce}^{3+}$  (0.103 nm) is slightly smaller than that of  $\text{Pb}^{2+}$  (0.120 nm). The  $\text{Ce}^{3+}$  ions would go into  $\text{PbWO}_4$  crystal lattice well. The  $\text{Ce}^{3+}$  ions are likely to enter  $\text{PbWO}_4$  crystal lattice to substitute  $\text{Pb}^{2+}$  sites considering that the ionic radius of  $\text{Ce}^{3+}$  (0.103 nm) is smaller than that of  $\text{Pb}^{2+}$  (0.120 nm) So the lattice parameters of Cerium doped  $\text{PbWO}_4$  could be undoubtedly reduced. As reported for the La-doped  $\text{PbWO}_4$ , the cell parameters decrease with increasing  $\text{La}^{2+}$  content [28]; a similar trend was also observed in results of our experiments.

Figure 3.8.4 shows the shift toward higher angle of reflection peaks suggested that the cell parameters of as-synthesized products could decrease with  $\text{Ce}^{3+}$  doping for the sample synthesized at 100 °C. The similar change can be seen in for the sample synthesized at 150 °C and 200°C also in Figure 3.8.4. The decrease in lattice parameter can also be confirmed from the Table 4.0. Distance between peak positions of undoped and Cerium doped  $\text{PbWO}_4$  is increases with increase in the temperature, corresponding variation in lattice parameters can also be seen from Table 4.0.

## References

- [1] Wei Zhao, Xinyu Song, Guozhu Chen, Guangru Tian and Sixiu Sun, *Materials Letters* 63, 285–288, 2009.
- [2] Biao Liu, Shu-Hong Yu, Linjie Li, Qiao Zhang, Fen Zhang and Ke Jiang, *Angew. Chem.* 116, 4849–4854, 2004.
- [3] Guangyu Chen, Liangbao Yang and Jinhui Liu, *Cryst. Res. Technol.* 44, 7, 736–740, 2009.
- [4] Titipun Thongtem, Sulawan Kaowphong and Somchai Thongtem, *Ceramics International* 35, 1103–1108, 2009.
- [5] Jun Geng, Jun-Jie Zhu and Hong-Yuan Chen, *Crystal Growth & Design*, Vol.6, No.1, 2006.
- [6] Jun Geng, Yinong L, Dujuan Lu and Jun-Jie Zhu, *Nanotechnology* 17, 2614–2620, 2006.
- [7] Jun Geng, Dujuan Lu, Jun-Jie Zhu and Hong-Yuan Chen, *J. Phys. Chem. B* 110, 13777-13785, 2006.
- [8] Yan Fang, Ying Xiong, Yuanlin Zhou, Jinxiang Chen, Kaiping Song, Yi Fang and Xulan Zhen, *Solid State Sciences* 11, 1131–1136, 2009.
- [9] Xian-Luo Hu and Ying-Jie Zhu, *Langmuir* 20, 1521-1523, 2004.
- [10] Xiaoyan He and Minhua Cao, *Nanotechnology* 17, 3139–3143, 2006.
- [11] Di Chen, Guozhen Shen, Kaibin Tang, Zhenhua Liang and Huagui Zheng, *J. Phys. Chem. B*, 108, 11280-1284, 2004.
- [12] Changhua An, Kaibin Tang, Guozhen Shen, Chunrui Wang and Yitai Qian, *Materials Letters* 57, 565–568, 2002.
- [13] Thresiamma George, Sunny Joseph, Anu Tresa Sunny and Suresh Mathew, *J Nanopart Res* 10, 567–575, 2008.

- [14] Jinhua Yang, Conghua Lu, Hong Su, Jiming Ma, Humin Cheng and Limin Qi, *Nanotechnology* 19, 035608, 2008.
- [15] Guangjun Zhou, Mengkai Lu, Feng Gu, Dong Xu and Duorong Yuan, *Journal of Crystal Growth* 276,577–582, 2005.
- [16] Guangjun Zhou, Mengkai Lu, Benyu Su, Feng Gu, Zhiliang Xiu, Shufen Wang, *Optical Materials* 28,1385–1388, 2006.
- [17] Chunhua Zheng, Chenguo Hu, Xueyan Chen, Hong liu, Yufeng Xiong, Jing Xu, Buyong Wana and Linyong Huang, *CrystEngComm*, 12, 3277–3282, 2010.
- [18] Guizhen Wang, Chuncheng Hao, *Materials Research Bulletin* 44, 418–421, 2009.
- [19] Jeong Ho Ryu, Sang-Mo Koo, Dong Suk Chang, Jong-Won Yoon, Chang Sung Lim and Kwang Bo Shim, *Ceramics International* 32,647–652, 2006.
- [20] Hua Tang, Changsheng Li, Haojie Song, Xiaofei Yang and Xuehua Yan, *CrystEngComm*, 13, 5119, 2011.
- [21] C. Suryanarayana, M.G. Norton, *X-ray Diffraction: A Practical Approach*, Plenum Press, New York, 1998.
- [22] M. Kobayashi, Y. Usuki, M. Ishii, N. Senguttuvan, K. Tanji, M. Chiba, A. Hark, H. Takano, M. Nikl, P.Bohacek, S. Baccaro, A. Cecilia, M. Diemoz, A. Vedda and M. Martini, *Nucl. Instrum. Methods Phys. Res. A* 465, 428, 2001.
- [23] D.Tawde, M.Srinivas & K.V.R.Murthy, *physics status solidi a*, Vol.208, Issue 4, 2011, 803- 807.
- [24] D.Tawde, Dhaval Modi, M.Srinivas and K.V.R. Murthy, manuscript accepted to be published in *International Journal of Luminescence and its Applications*, 2012.
- [25] Jun Geng et al., *Crystal Growth & Design*, Vol. 6, No.1, 2006.
- [26] G. Zhou, M. Lu, F. Gu, D. Xu, D. Yuan, *J. Cryst. Growth* 276, 577, 2005.
- [27] L.S. Cavalcante , J.C. Sczancoski , V.C. Albarici , J.M.E. Matos , J.A. Varela , E.

Long , *Materials Science and Engineering B* 150,18–25, 2008.

[28] S. Takai, S. Touda, K. Oikawa, K. Mori, S. Torii, T. Kamiyama, T. Esaka, *Solid State Ionics* 148, 123, 2002.

## 4.1 Characterization Techniques

### 4.1.1 Transmission Electron Microscopy (TEM)

Transmission electron microscopy (TEM) is a microscopy technique where a beam of electrons is transmitted through an ultra thin specimen, interacting with the specimen as it passes through. An image is formed from the interaction of the electrons transmitted through the specimen; the image is magnified and focused onto an imaging device, such as a fluorescent screen, on a layer of photographic film, or to be detected by a sensor such as a CCD camera. TEM Characterization of our samples were carried out at two different facility centres during our research work. One at UGC-CSR, Indore centre and other at SICART, Vidhyanagar. Images of TEM instrument at both centers are shown below.



**Figure 4.1** Photograph of TEM (Model : Philips Tecnai 20 G2, FEI make) instrument at UGC-CSR, Indore Centre.



**Figure 4.2** Photograph of TEM (Model : Philips Tecnai 20, Holland) instrument at SICART, Vidhyanagar, Anand.

### 4.1.2 Scanning Electron Microscopy (SEM)

Scanning electron microscopy (SEM) is a type of electron microscopy that images a sample by scanning it with a beam of electrons in a raster scan pattern. The electrons interact with the atoms that make up the sample producing signals that contain information about the sample's surface topography, composition, morphology, shape and size. Preparation of the samples is relatively easy since most SEMs only require the sample to be conductive. The SEM has a large depth of field, which allows a large amount of the sample to be in focus at one time. The SEM also produces images of high resolution, which means that closely spaced features can be examined at a high magnification. SEM characterization of our samples were carried out at Electrical Research Development Association (ERDA),Vadodara.

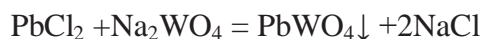
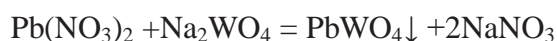
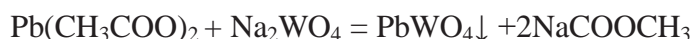


**Figure 4.3** Photograph of SEM (JEOL JSM-6380LV) instrument at ERDA,Vadodara.

## 4.2 Introduction

It is well known that the crystal growth is controlled by the extrinsic as well as intrinsic factors, including the degree of supersaturation, diffusion of the reaction, surface energy, crystal structure etc. in the solution reaction system. Crystallization process can be divided into two events: *Nucleation* and *Crystal growth*. The size and the morphology of the products depend on the competition between nucleation and crystal growth, which are determined by the inherent crystal structure and the chemical potential in the precursor solution.

In our experiments  $\text{PbWO}_4$  were synthesized in aqueous solution under the effect of different reaction conditions i.e. Pb Source, temperatures, pH of reaction solution. As a result, we obtained undoped and Cerium  $\text{PbWO}_4$  nanomaterials through the reaction between  $\text{Pb}^{2+}$  and  $\text{WO}_4^{4-}$  at hydrothermal conditions having interesting morphologies. In present work, we have not used any type of directing or capping agent e.g. CTAB, PVP, EG etc. because these surfactants are expensive which increase the production cost. The reaction processes can be expressed as follows:



By mixing  $\text{Na}_2\text{WO}_4$  and surfactant (distilled water in our case),  $(\text{WO}_4)^{2-}$  anions were possibly coordinated to the surfactant molecules to form surfactant–tungstate complexes. The addition of Lead source compound into the solution containing the surfactant–tungstate complexes under the assistance of constant magnetic stirring and heating in Teflon lined Stainless steel autoclave led to the substitution of the surfactant by  $\text{Pb}^{2+}$  cations. At the beginning of the reaction,  $\text{PbWO}_4$

nuclei produced in solution aggregate to form small particles. These particles may serve as crystal seeds to grow the building blocks for different structures. Once  $\text{PbWO}_4$  nuclei (very fine particles) formed, they came together to form crystalline solids. The surfactant may have been selectively adsorbed onto the crystals and possibly desorbed due to magnetic stirring and heating in autoclave, resulting in a particular shape from the anisotropic process.

### 4.3 Effect of Lead Source on Morphology of $\text{PbWO}_4$

As discussed in Section 3.3.2 of Chapter 3, large single crystals of  $\text{PbWO}_4$  are extensively grown using  $\text{PbO}$  and  $\text{WO}_3$  as precursors which were used for scintillation detector or other application based on macro dimensions. Recent development in nanotechnology requires  $\text{PbWO}_4$  material having different morphologies and dimensions suitable for nano-devices. So it is important to study effect of different reaction parameters (Precursor, pH, Concentration, Time and Temperature) on morphology of the final product. Among these effect of reaction parameters pH, concentration, time and temperature had reported in many literatures. It should be noted that the effect of different Lead sources on morphology and crystal structure of  $\text{PbWO}_4$  has not been investigated yet except us [1]. Lead sources (Lead Acetate, Lead Nitrate and Lead Chloride) have different chemical properties and hence react differently with  $\text{Na}_2\text{WO}_4$  under the same hydrothermal reaction conditions. They required different amount of energy in order to react with  $\text{Na}_2\text{WO}_4$  rather surfactant–tungstate complex to form  $\text{PbWO}_4$ . The effect of different Lead sources [ $\text{Pb}(\text{CH}_3\text{COO})_2$ ,  $\text{Pb}(\text{NO}_3)_2$  and  $\text{PbCl}_2$ ] on the morphology of  $\text{PbWO}_4$  were investigated from TEM and SEM characterization. Many interesting morphologies were produced in our experiments without the use of expensive template or surface directing capping agents by facile low temperature hydrothermal method. The results of our experiments demonstrate that different Lead sources could also affect the morphology of the products as discussed below.

## 4.4 PbWO<sub>4</sub> prepared with Lead Acetate

The morphology of pure and Cerium doped PbWO<sub>4</sub> prepared by Pb(CH<sub>3</sub>COO)<sub>2</sub> (Lead Acetate) as a lead source were characterized through SEM and TEM. When Pb(CH<sub>3</sub>COO)<sub>2</sub> was used as the Lead source, obtained PbWO<sub>4</sub> displayed agglomerated dendrite or seaweed like shape of around 5μm [see Figure 4.4(b)] long and regular tetrahedron shaped particles are about 500nm size [see Figure 4.4(d)]. Dendrites are well-defined, complex and highly ordered and structurally similar to those prepared by sonochemical preparation method with N-cetyl pyridinium chloride surfactant [2] shown in Figure 4.4(a). The individual PbWO<sub>4</sub> dendrite shown in inset of Figure 4.4 (a) and (b) has only one trunk and shrunken branches. The branches are perpendicular to the trunk and they are built up of parallel-arrayed particles.

### 4.4.1 Tetrahedron shaped microparticles of PbWO<sub>4</sub>

Small crystalline nuclei are formed in a highly supersaturated solution right after the mixing of the reactants at the molecular level called nucleation process. These tiny nuclei acted as precursor to form various morphologies. Thermodynamically all of the nuclei will grow towards the shape having the lowest energy at equilibrium. Larger particles grew at the cost of the small ones, due to the difference in solubility between the large particles and the small particles according to Gibbs-Thomson law. Synthesis of such type of tetrahedron shaped particles was reported by Qilin Dai et al in [3] by hydrothermal method. These crystals further aggregate and attach to each other by oriented attachment process to form dendrite shaped microstructures. Moreover, The Ostwald ripening process contributes to the self-assembly of the tetrahedron nanocrystals by sharing the edges of polyhedrons.

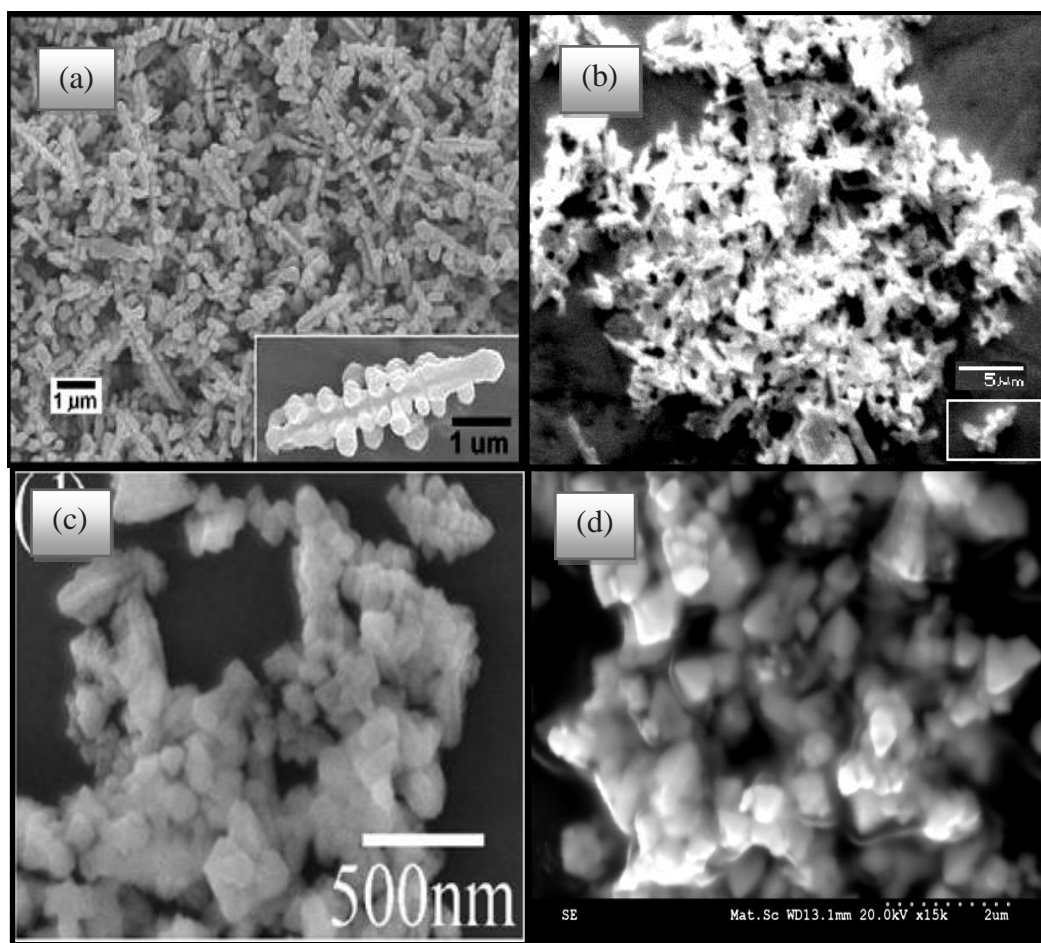


**Figure 4.4** SEM images of  $\text{PbWO}_4$  (a) agglomeration of dendrite with single trunk reported in ref. [2]; (b) single trunk dendrite produced using Lead Acetate as lead source; (c) tetrahedron microparticles reported in ref. [3]; (d) tetrahedron microparticles produced using Lead Acetate as lead source.

#### 4.5 PbWO<sub>4</sub>:Ce prepared with Lead Acetate

According to literature survey only Yan Fang et.al. [4] reported the effect of Ce doping on morphology of PbWO<sub>4</sub> produced using Lead Acetate as Lead source. He found that Cerium doping in PbWO<sub>4</sub> changes morphology from Prism-like structure with terminating pyramids to shuttle shape. Similar type of Prism-like morphology (Tetrahedron microparticles) of undoped PbWO<sub>4</sub> also produced in our case as mentioned in previous section but when Cerium was doped one dimensional microbelts like morphology was obtained shown in Figure 4.5 and Figure 4.6. Possible reason and process for production of microbelt like structure is explained in detail in the next section.

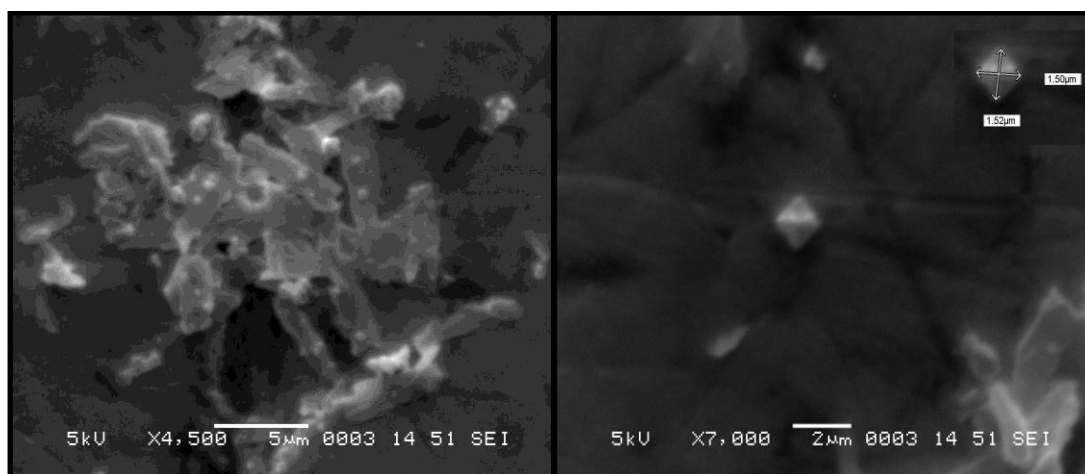


**Figure 4.5** SEM images of microbelts (left) and octahedron microparticles (right) of PbWO<sub>4</sub>:Ce produced using Lead Acetate as lead source.

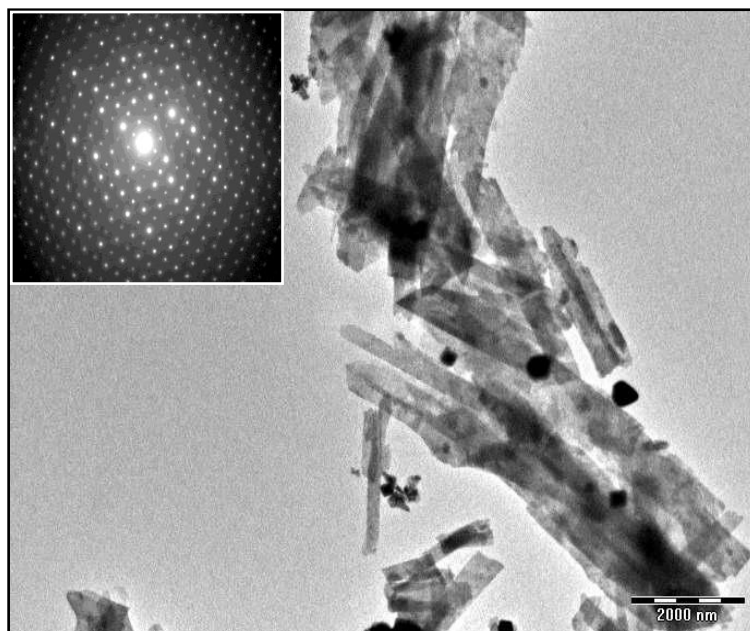


**Figure 4.6** TEM images of PbWO<sub>4</sub>:Ce produced using Lead Acetate as lead source.

Figure 4.5 represents the SEM photographs of Cerium doped PbWO<sub>4</sub> prepared by Lead Acetate as a lead source. As shown in images Cerium doping in PbWO<sub>4</sub> host lattice produced flat microbelt. PbWO<sub>4</sub>:Ce microbelts are about 5 μm long and about 1 μm broad. High magnification SEM image [Figure 4.5 (right)] shows that Octahedron shaped Cerium doped PbWO<sub>4</sub> microparticles are also present along with microbelt. An individual PbWO<sub>4</sub>: Ce Octahedron particle is shown in inset of Figure 4.5 (right) having length along the long axis about 1.52 μm and along short axis about 1.50 μm. Formation of such microbelt like structures also supported by TEM photograph as shown in Figure 4.6 TEM image inferred agglomeration of microbelts having width about 100 nm and few μm in length. Electron Diffraction (ED) pattern of thus obtained PbWO<sub>4</sub> is shown in inset of Figure 4.6. ED patterns shows well crystalline microbelts were formed at low temperature mild hydrothermal method.

#### 4.5.1 Raspite Phase

In ref. [1] we have proposed that one dimensional flat microbelt like structure is produced due to raspite phase of  $\text{PbWO}_4$ . Cerium will not play any direct role in the production of belt like structure. Very few reports have been published on the preparation of raspite phase in the laboratory. The raspite  $\text{PbWO}_4$  nanobelts were synthesized using charged dextran as a structure directing coordination molecular template by J. Yang [5]. With the assistance of PVP surface-capping agent, the bamboo-leaf-like raspite  $\text{PbWO}_4$  nanostructures were fabricated by T. Gorge et al [6] and with composite-salt-mediated synthesis method by C. Zheng [7] to prepare ultra-long  $\text{PbWO}_4$  raspite nanobelts. C. Zheng prepared few millimetre long  $\text{PbWO}_4$  nanobelts at  $160^\circ\text{C}$  for 18 h reaction duration by using composite-salt ( $\text{LiNO}_3/\text{KNO}_3$ ) at 9 pH while we get  $\text{PbWO}_4$  nanobelts about  $5\mu\text{m}$  long and 500 nm broad at comparatively low ( $100^\circ\text{C}$ ) temperatures for short (12h) reaction time at 7pH. This result shows that  $\text{PbWO}_4$  microbelts can be produced at lower temperature without using any surfactant/capping agent or composite salt by hydrothermal method. Morphology of  $\text{PbWO}_4$  microbelt produced in our case is similar to bamboo-leaf-like which is close to reported by T. Geogre et al. using polyol (polyethylene glycol-200).

4.5.2 Growth Mechanism of  $\text{PbWO}_4$  microbelt

A schematic illustration of the growth mechanism of the raspite phase lead tungstate microbelt is shown in Figure 4.7. In the initial stage, the  $\text{OH}^-$  ions from  $\text{H}_2\text{O}$  react with  $\text{Pb}^{2+}$  ions of Lead Source to produce the  $\text{Pb}(\text{OH})_2$  molecule. The  $\text{Pb}(\text{OH})_2$  molecule further reacts with  $(\text{WO}_4)^{2-}$  ion of  $\text{Na}_2\text{WO}_4$  to form  $\text{PbWO}_4$  nuclei and release  $\text{OH}^-$  ions, and the latter is adsorbed on the surface of the former.

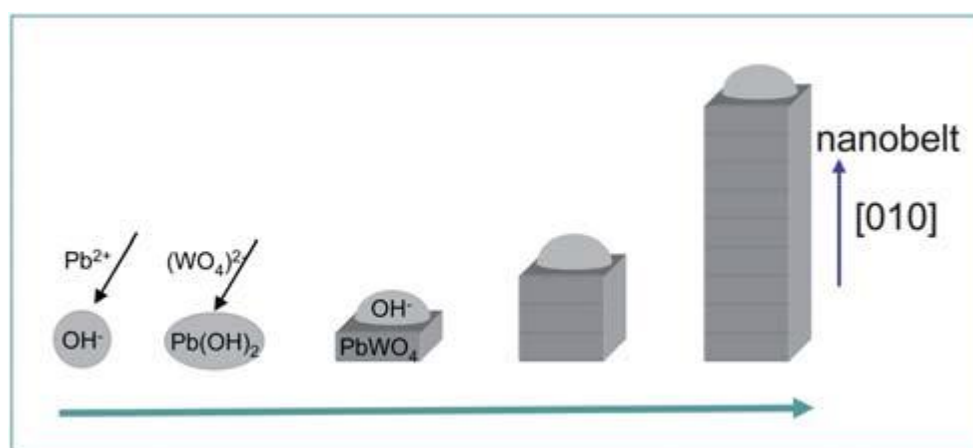


**Figure 4.7** Growth mechanism of  $\text{PbWO}_4$  microbelt suggested by C. Zheng [7].

In the second stage, the adsorbed  $\text{OH}^-$  ion reacts with a nearby  $\text{Pb}^{2+}$  ion to produce  $\text{Pb}(\text{OH})_2$ , and then react with  $(\text{WO}_4)^{2-}$  ions to form the bigger  $\text{PbWO}_4$  nuclei. Unit cell of raspite  $\text{PbWO}_4$  contain four  $\text{Pb}^{2+}$ , four  $\text{W}^{6+}$  and sixteen  $\text{O}^{2-}$  ions. Table 4.1 shows calculated atomic packing density for different faces for different lead sources.

**Table 4.1** Summary of lattice parameter and atomic packing density of different lead sources.

Lead Source	Lattice Parameter ( $\text{\AA}$ )			Atomic packing density ( $\text{\AA}^{-2}$ )		
	a	b	c	(100)	(010)	(001)
Lead Acetate	13.525	4.9682	5.546	0.036	0.028	0.030
Lead Nitrate	13.580	4.9900	5.5600	0.036	0.028	0.030
Lead Chloride	13.555	4.9760	5.5601	0.036	0.028	0.030

Due to the structured anisotropy of the raspite  $\text{PbWO}_4$  crystal, the top faces (exposure surfaces) of (100), (010) and (001) have different atomic packing density and surface energy. Theoretically, the face that contains all four  $\text{Pb}^{2+}$  ions possesses the highest density of  $\text{Pb}^{2+}$  ions, though this kind of face is unusual and less stable. The density of  $\text{Pb}^{2+}$  ions in this face is about  $0.045 \text{ \AA}^{-2}$ . However, the density of possible exposure surfaces calculated is  $0.036 \text{ \AA}^{-2}$  [ $1/(4.968 \text{ \AA} \times 5.546 \text{ \AA})$ ] for (100),  $0.028 \text{ \AA}^{-2}$  [ $2/(13.52 \text{ \AA} \times 5.546 \text{ \AA} \sin 107.7^\circ)$ ] for (010) and  $0.030 \text{ \AA}^{-2}$  [ $2/(13.52 \text{ \AA} \times 4.968 \text{ \AA})$ ] for (001) faces. Atomic packing density is inversely proportional to the surface energy. In other words, the top faces (exposure surfaces) of (100) and (001) of  $\text{PbWO}_4$  nanobelts may have larger packing density and lower surface energy, while the top faces of (010) have the smallest packing density and highest surface energy [8]. So the  $\text{OH}^-$  ions would be preferentially adsorbed on the (010) faces to reduce the surface energy, which finally form the quasi-one-dimensional  $\text{PbWO}_4$  microbelts after periodical repeat of the previous growth process. So it is reasonable to conclude that the  $\text{PbWO}_4$  microbelt grows along the [010] direction to reduce surface energy with the side faces of the microbelt contained by the  $\text{Pb}^{2+}$ -enriched (100) and (001) planes. Similar type of  $\text{PbWO}_4$  microbelts also produced when we use  $\text{Pb}(\text{NO}_3)_2$  and  $\text{PbCl}_2$  as lead sources, which shows that the process of  $\text{PbWO}_4$  microbelt formation is independent of Lead Sources.

#### 4.6 PbWO<sub>4</sub> prepared with Lead Nitrate

PbWO<sub>4</sub> was synthesized using Lead Nitrate as a Lead source. When Pb(NO<sub>3</sub>)<sub>2</sub> was used as the lead source, the product consists of agglomerated microbelts and dendrites as we can see from SEM images in Figure 4.8. Microbelts are flat with irregular edge. Average length of microbelt is about 5 μm and width is about 1 μm. Similar type of microbelts with regular edges were also produced in the case of Cerium doped PbWO<sub>4</sub> synthesized using Lead Acetate. Dendrite having single trunk were produced with Lead Acetate while here three dimensional dendrites having six branched or trunk is produced. The length of the long trunk is about 2.10 μm and that of the two branches is about 1.18 μm can be seen in inset of Figure 4.8 (b).

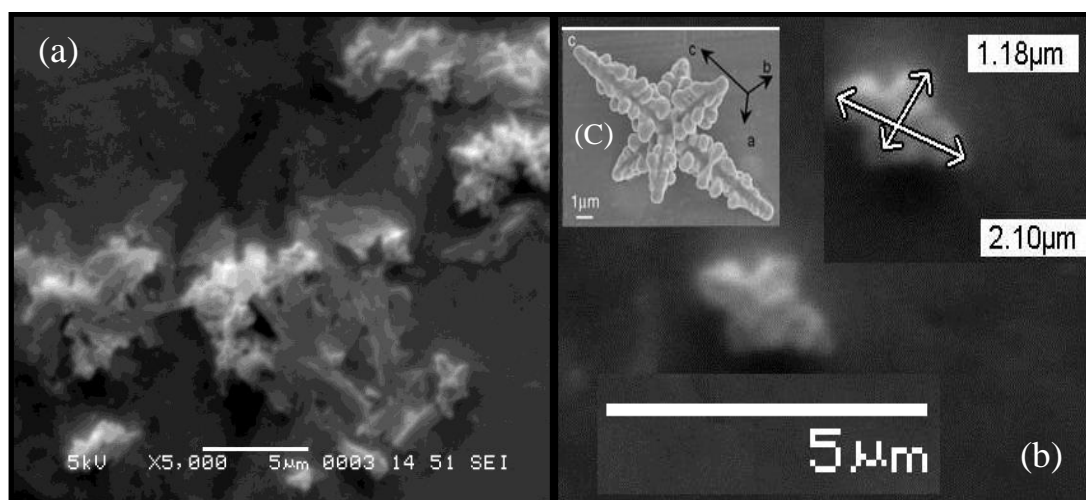


**Figure 4.8** (a) SEM image of agglomerated microbelts and dendrites of PbWO<sub>4</sub>; (b) High magnified SEM image of individual six branched/trunk dendrite (inset shows same dendrite with scale); (c) Three dimensional dendrite reported in [9] by Biao Liu et al. with CTAB surfactant.

#### 4.6.1 Explanation of formation of $\text{PbWO}_4$ 3-Dimensional dendrite

However, the individual  $\text{PbWO}_4$  dendrite with three-dimensional structure displays more complex features which are similar to reported by Biao Liu et al. with CTAB surfactant with Hydrothermal method [9] as shown in a higher magnification SEM image of individual dendrite (inset to Figure 4.8 (c)). 3-dimensional dendrite structure is complex, uniform and systematic. There are two pair of short trunks and one pair of long trunk. The trunks are in the shape of pine trees and have arrowhead-shaped tips. Four branches of two short trunks grow vertically on main long trunk in perpendicular directions and in the same plane. The length of the long trunk is about  $2.10 \mu\text{m}$  and that of the two paired branches is about  $1.18 \mu\text{m}$ . The ratio of the lengths of the three main trunks is equal to the ratio of the cell parameters  $c/a = c/b = 2.2:1$ ; therefore, it is believed that the longer trunk grew in the  $c$  direction and the two shorter ones, in  $a$  or  $b$  directions.  $\text{PbWO}_4$  dendrite produced in our case is 10 times smaller than that of reported by Biao Liu et. al. We have not used expensive surface capping agent to produce such a 3-dimensional structure which lowers the production cost though optimisation is required. The dimensions of such high hierarchical structures finely reflect the intrinsic cell structure of stolzite. Further optimization of the growth conditions could make it possible to obtain perfect uniform hierarchical structures.

#### 4.6.2 Explanation of formation of rhombic shaped $\text{PbWO}_4$ particles

$\text{PbWO}_4$  particles with rhombic shape were also produced with Lead Nitrate which is shown in Figure 4.9 (a) of below TEM image.

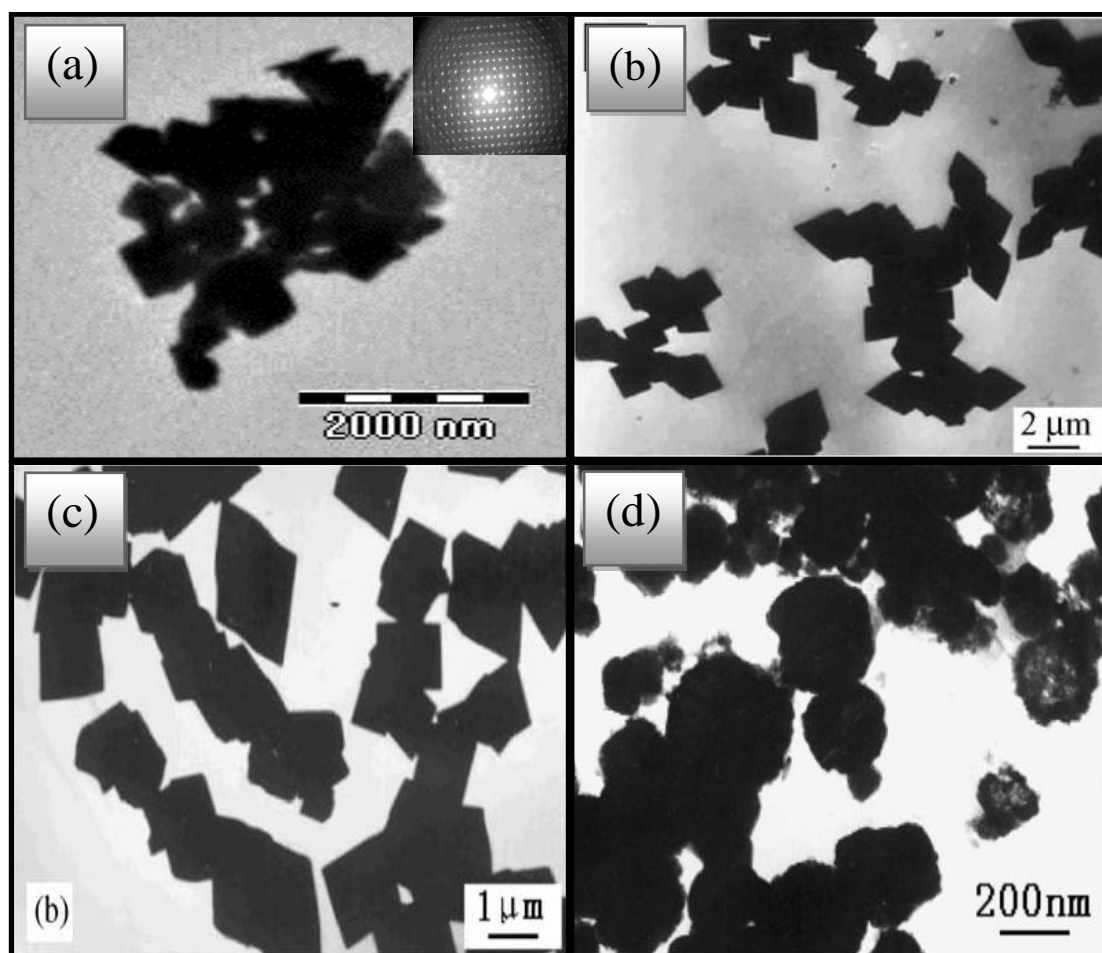


**Figure 4.9** TEM image of rhombic shaped  $\text{PbWO}_4$  microparticles (a) synthesized by us without using any surfactant; (b) synthesized by using PVP [12] and (c) CTAB [13] surfactant; (d) nanoparticles prepared without surfactant.

As mentioned earlier, the  $\text{PbWO}_4$  nanoparticles are produced via hydrothermal crystallization process in the supersaturated solution. One basic crystal-growth mechanism in supersaturated solution systems is the well known “**Ostwald ripening process**” [10]. In the Ostwald ripening process, the initial formation of tiny crystalline nuclei in a supersaturated medium is followed by crystal growth. In this process the larger particles grow at the cost of the small ones due to the energy difference between large particles and small particles. This difference is reflected in the higher solubility of the smaller particles as defined by the Gibbs–Thompson law [11] which tells that solubility is inversely proportional to the particle size. These freshly formed nuclei are unstable and have the tendency to grow into larger particles due to their high chemical potential. The rhombic-shaped particles are then formed via a transformation process using the  $\text{PbWO}_4$  nanoparticles [Figure 4.9 (d)] as precursors. Guangjun Zhou et al. had produced similar shaped  $\text{PbWO}_4$  micro sized particles by using PVP (poly-vinyl-pyrrolidone K30) [12] and CTAB [13] (cetyltrimethylammonium bromine) shown in Figure 4.9 (b) and (c), respectively. It should be noted that we have not use any type of surfactant to produced rhombic shaped  $\text{PbWO}_4$ . Moreover  $\text{PbWO}_4$  particle which are produced in our experiments are about 500 nm in size while those prepared by Guangjun Zhou [12, 13] et al. are about 1 $\mu\text{m}$  in size. This result shows that by using hydrothermal method we can produce rhombic shaped  $\text{PbWO}_4$  without using any surfactant.

As reported by Changhua An in [14], rod and flake like morphology with stolzite phase of  $\text{PbWO}_4$  was produced during 100-150 °C temperature range and 3-8 h reaction time, while in our case six branched dendrite, microbelt and rhombohedral morphology were produced around 100°C for 12 h reaction period. Comparing all the results we can say that initially nanoparticles are formed as soon as the both reactants

mixed in the supersaturated aqueous solution. When such mixture is treated in the autoclave for 3-8 hr  $\text{PbWO}_4$  nanoparticles grow to form rod and flake like structure for shorter duration of reaction time. If we increase the reaction time for 12 h as in our case, rhombic shaped  $\text{PbWO}_4$  microparticles are produced which turns into single or multiple branched dendrite or flat microbelt structure. Also we can conclude that at lower temperature raspite phase is produced and with increases in temperature raspite phase turns into stolzite phase.

#### 4.7 PbWO<sub>4</sub>:Ce prepared with Lead Nitrate

Preparation of Cerium doped PbWO<sub>4</sub> using Lead Nitrate as a Lead source is not reported yet by any other method except us with hydrothermal method [1]. Figure 4.10 shows TEM image of tetrahedron shaped microparticles of Cerium doped PbWO<sub>4</sub> at different magnification. Similar tetrahedron microparticles having size about 500nm were produced when Lead Acetate was used as Lead source. Size of microparticles is reduced to 100 nm which may attribute to smaller ionic radius of Ce<sup>3+</sup> ion (0.103 nm) compared to Pb<sup>2+</sup> ions (0.120 nm).

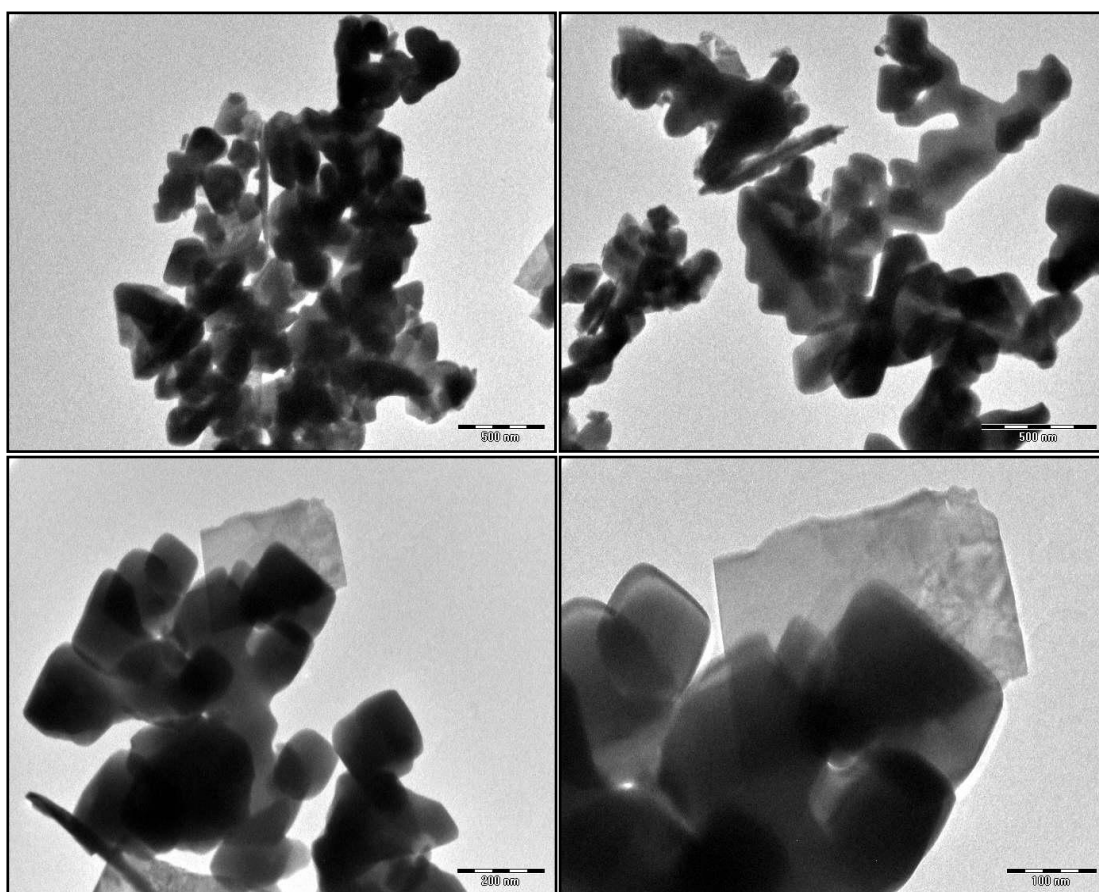


**Figure 4.10** TEM images of Cerium doped tetrahedron PbWO<sub>4</sub> prepared using Lead Nitrate as a Lead source with different magnification.

Formation mechanism of Tetrahedron microparticles have been already discussed in section 4.4.1. The formation of  $\text{PbWO}_4$  tetrahedron is attributed to the favourable thermo-dynamic conditions. The formation and evolution processes can be divided into three steps: initial nucleation process in supersaturated solution, self-assembly process (oriented aggregation), and subsequent crystal growth process (Ostwald ripening).

## 4.8 PbWO<sub>4</sub> prepared with Lead Chloride

According to our literature survey, only one paper by Changhua An [14] had been reported so far in which Lead Chloride was used as a Lead source to produce PbWO<sub>4</sub>. PbWO<sub>4</sub> nanomaterial prepared with Lead chloride a Lead source shows excellence Photoluminescence compared to other that prepared with Lead Nitrate and Lead Acetate which will discussed in next chapter. The TEM photographs of PbWO<sub>4</sub> obtained by using Lead Chloride as a Lead source under identical reaction conditions shown in Figure 4.11. As shown in TEM images, microparticles of octahedron shape having size around 100 nm as well as flat microplates having width 100-150nm and about few  $\mu\text{m}$  in length are obtained. Changhua An et al. reported formation of similar type morphology for 100°C -150°C reaction temperature and 3-8 h reaction duration.

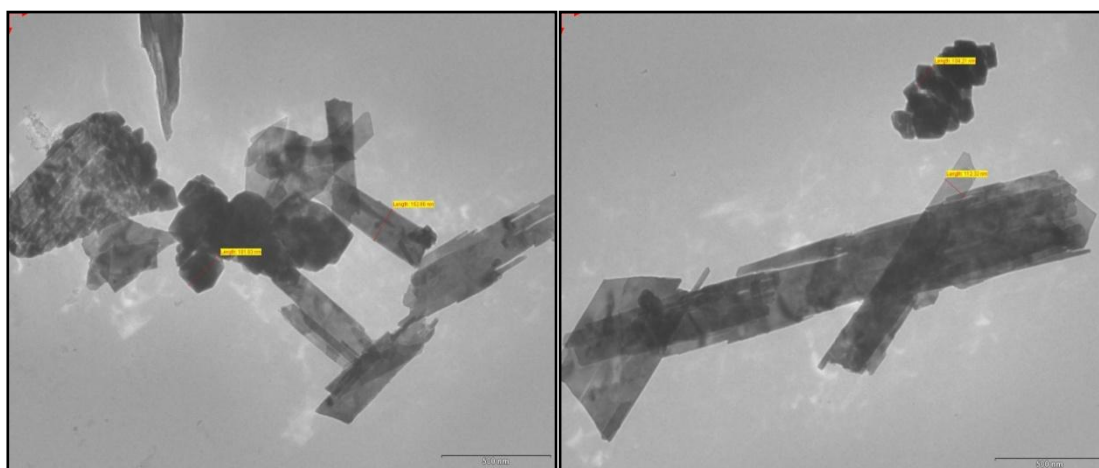


**Figure 4.11** TEM images of agglomerated octahedron microparticles and flat micro belts of PbWO<sub>4</sub> prepared with Lead Chloride (both images are of same sample).

#### 4.9 PbWO<sub>4</sub>:Ce prepared with Lead Chloride

Cerium doping during preparation of PbWO<sub>4</sub>, produces tetrahedron shaped microparticles having size around 100 nm as shown in Figure 4.11. Similar type of Tetrahedron shaped microparticles were produced with Lead Nitrate as a Lead source. Formation mechanism of PbWO<sub>4</sub> microparticles can explain on the basis of Oswald ripening process followed by oriented attachment of PbWO<sub>4</sub> microparticles to form dendrite like structure similar to that form in Lead Nitrate case.

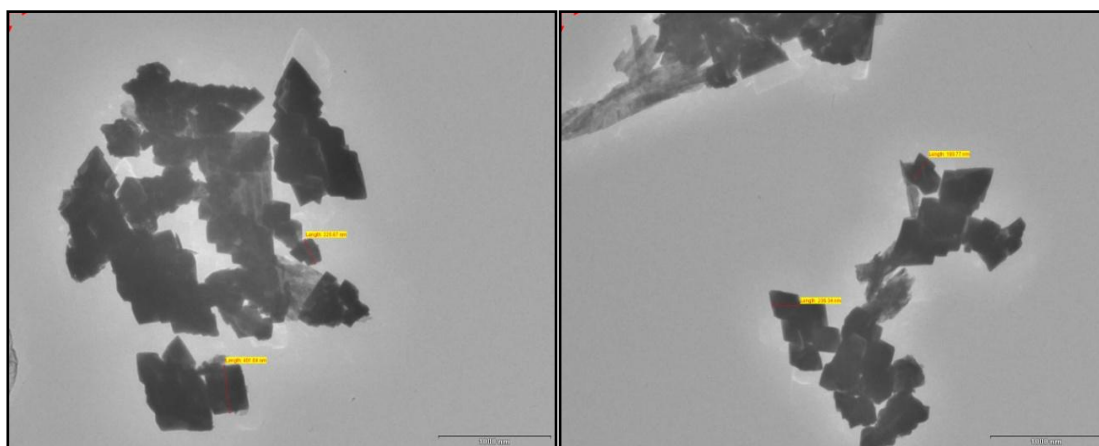


**Figure 4.12** TEM images of agglomerated tetrahedron microparticles of Cerium doped PbWO<sub>4</sub> prepared with Lead Chloride (both images are of same sample).

X-ray diffraction studies in the previous chapter 3 reveals that Cerium doping in the PbWO<sub>4</sub> crystal lattice suppress the formation of raspite phase and favours production of stolzite phase. We proposed that flat microbelt and flake like morphologies are related to raspite phase and dendrite (whether single or multiple branched), microparticles with tetrahedron and rhombic shaped morphologies are related to stolzite phase. As Cerium having tendency to suppress raspite phase related morphologies, morphologies related to stolzite phase predominantly produced in the Cerium doped samples. It should be noted that these type of behaviour is observed in

Cerium doped  $\text{PbWO}_4$  samples prepared with Lead Nitrate and Lead Chloride. Cerium doped  $\text{PbWO}_4$  samples prepared with Lead Acetate do not show this type of characteristics. Single branched dendrites (stolzite phase related morphology) produce in the case of undoped sample which is understood but Cerium doped sample produce microbelts (raspite phase related morphology) which is deviating our assumption. This contradiction can be explained on the basis of limitation of characterization techniques including skill of operating technician. We know that from xrd analysis, all the samples produced at  $100^\circ\text{C}$  temperature contains almost equal amount of stolzite as well as raspite phase. During TEM and SEM characterization very small areas of sample is focused. For example in the case of Cerium doped  $\text{PbWO}_4$ , if the area being focused contains more amount of raspite phase related morphologies compared to stolzite one, we will get images of microbelts though remaining area of sample contains more amount of morphologies related to stolzite phase. It is our future aim to investigate in this direction by analysing Cerium doped  $\text{PbWO}_4$  produced at higher temperatures by using Lead Acetate as a Lead source.

From above results we conclude that Cerium doping in  $\text{PbWO}_4$ , tetrahedron shaped microparticles with stolzite phase is dominantly produced over raspite phase. Thus Cerium plays an important role in controlling the morphology of  $\text{PbWO}_4$  prepared with Lead Nitrate and Lead Chloride. So we proposed that Cerium plays the role of surfactant or capping agent by regulating crystal growth direction. This is a very interesting phenomenon and it should be investigated for other types of rare earth elements also.

Thus we can see that various types of morphologies of undoped as well as Cerium doped  $\text{PbWO}_4$  can be prepared by using different Lead sources. The results of above experiments are summarized in Table 4.2.

**Table 4.2** Summary of morphologies and particle size of undoped and Cerium doped  $\text{PbWO}_4$  prepared using different Lead sources.

Sample No.	Lead Source	Dopant	Morphology	Dimensions
1	$\text{Pb}(\text{CH}_3\text{COO})_2$	-	single branched dendrite	$1\mu\text{m}$
			tetrahedron	500nm
2	$\text{Pb}(\text{CH}_3\text{COO})_2$	$\text{CeO}_2$	flat nanobelt	$5\mu\text{m} \times 1\mu\text{m}$
			octahedron microparticles	$1.5\mu\text{m}$
3	$\text{Pb}(\text{NO}_3)_2$	-	flat nanobelt	$5\mu\text{m} \times 1\mu\text{m}$
			six branched dendrites	$2\mu\text{m}$
			rhombic microparticles	500nm
4	$\text{Pb}(\text{NO}_3)_2$	$\text{CeO}_2$	tetrahedron	100nm
5	$\text{PbCl}_2$	-	micro plates	few $\mu\text{m}$
			microparticles	100nm
6	$\text{PbCl}_2$	$\text{CeO}_2$	tetrahedron	100nm

#### 4.10 Effect of reaction parameter on the morphology

Literature survey shows that reaction parameters such as pH of reaction solution during crystal growth, Temperature of reaction solution plays an important role to modified morphology and particle size of final product. In order to analyse effect of pH, Temperature and Cerium doping, TEM characterization of some selected samples are shown in below table were performed and discussed in this chapter.

**Table 4.3** Summary of reaction conditions of undoped and Cerium doped  $\text{PbWO}_4$  samples selected for TEM analysis.

Sample No.	$\text{PbCl}_2$ conc. (M)	$\text{Na}_2\text{WO}_4$ conc. (M)	Ce conc. (M)	Temp. ( $^\circ\text{C}$ )	Time (h)	pH
5	0.01	0.01	-	100	12	7
6	0.01	0.01	0.001	100	12	7
8	0.01	0.01	-	125	12	7
9	0.01	0.01	-	125	12	11
13	0.1	0.1	0.001	200	12	7

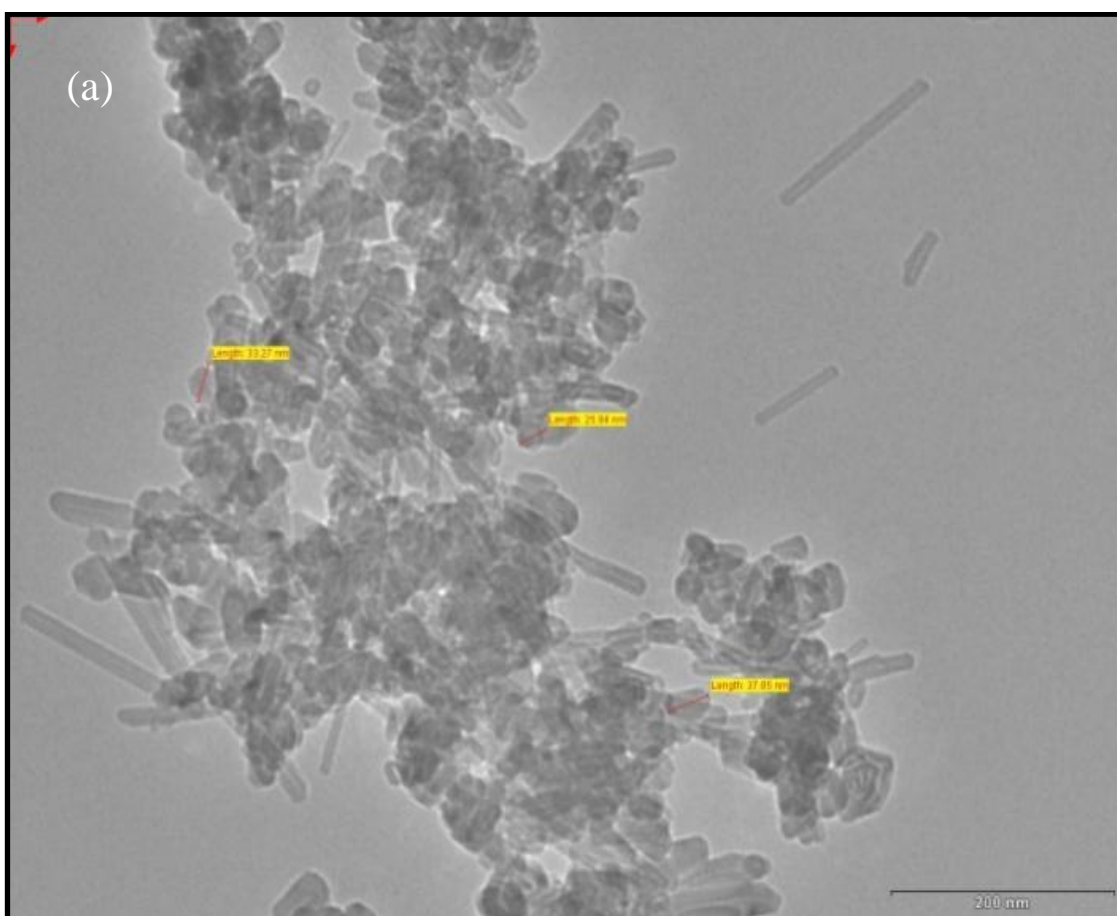
#### 4.11 Effect of pH of reaction solution on morphology of $\text{PbWO}_4$

The pH value of reaction system is one of the most important factors. It has been found that the pH value of the precursor medium plays an important role in the formation of tungstate phase and its morphology. We assume that the influence of pH value on the growth of the  $\text{PbWO}_4$  crystals may lie in three aspects: affecting the adsorption of surfactant to different facets, changing the relative energy of the different facets, and affecting the controlling growth mechanism.

As mentioned previously, we have prepared undoped  $\text{PbWO}_4$  at three different pH values (3pH, 7pH and 11pH). X-ray diffraction analysis of these samples discussed in Chapter 3 shows that all three samples are highly crystallized and indexed to purely tetragonal stolzite phase. In order to analyze morphology of these samples with TEM, two samples (samples prepared at 7pH and 11pH) were chosen based on their excellent photoluminescence spectra. TEM images of  $\text{PbWO}_4$  prepared at 7pH and 11pH are shown in Figure 4.13 and Figure 4.15, respectively. Both samples are prepared at 125 °C for 10 h reaction duration.

The product obtained at 7pH contains agglomerated Quasi-spherical hollow nanoparticles (HNPs) and hollow nanotubes (HNTs) of  $\text{PbWO}_4$  as shown in Figure 4.13. Hollow Nanoparticle (HNPs) have an average diameter of about 20-40 nm and their shape is not perfectly spherical.  $\text{PbWO}_4$  hollow nanotubes have outer diameter approximately 12.37 nm and length around 80-170 nm. Moreover, HNTs which are produced at 7pH are having uniform smooth surface. Upon rising pH to 11, nano particles were disappeared and bigger particles of irregular shape are formed as shown in Figure 4.16.  $\text{PbWO}_4$  nanorods are also produced at 11pH but their length increases from 80-170 nm to 2 $\mu\text{m}$  with 40 nm outer

diameter.  $\text{PbWO}_4$  nanorods produced at 11pH are not hollow like those formed at 7pH. Because of the small diameter, these nanorods have tendency to bundle together, a phenomenon always observed in single walled carbon nanotubes. A closer observation of the nanorods reveals that they have a narrow width distribution and uniform diameter throughout their entire length.



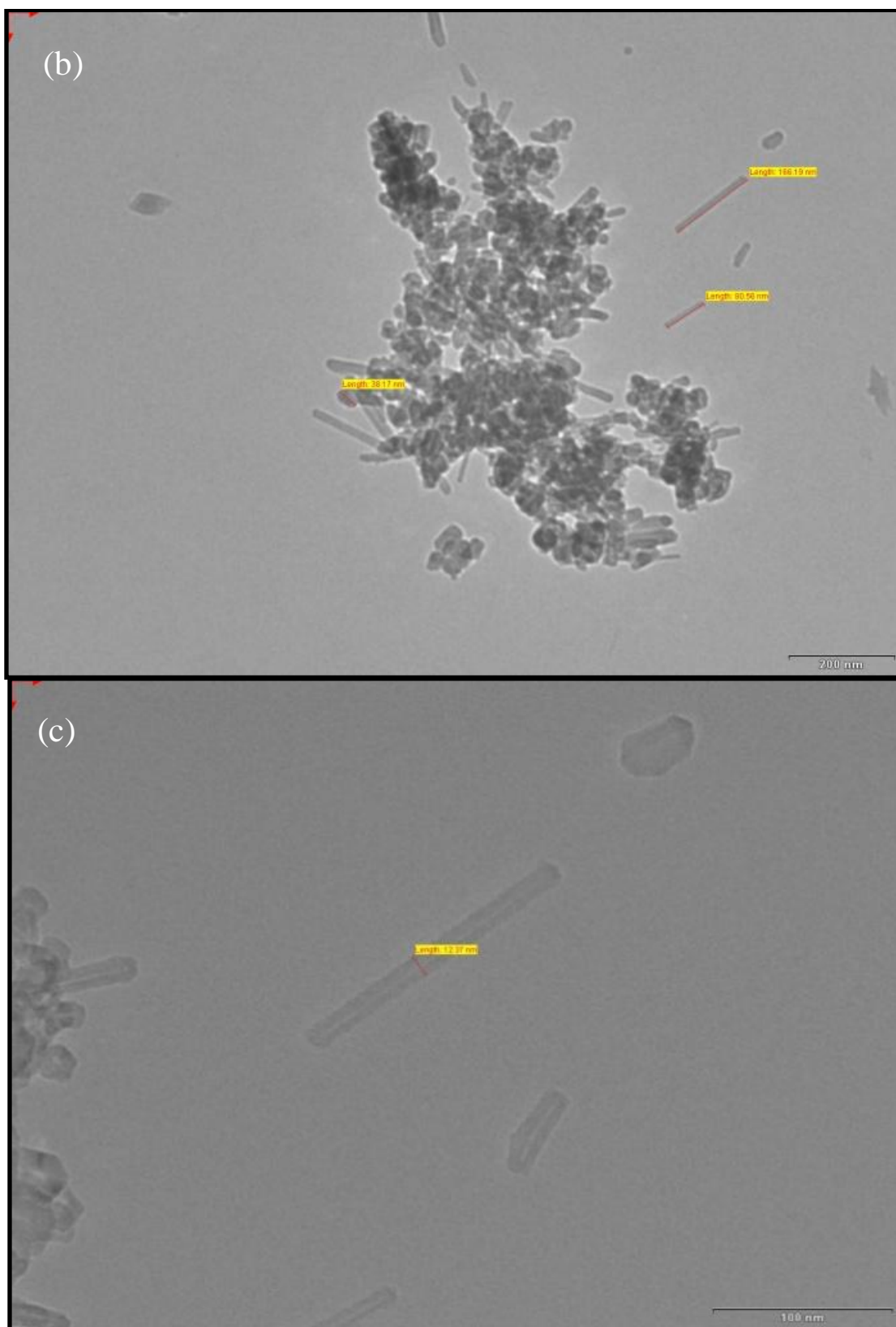


**Figure 4.13** The high-magnification TEM images of (a) quasi-spherical hollow nano particles (HNPs) of PbWO<sub>4</sub> with scale (b) hollow nano tubes (HNTs) of PbWO<sub>4</sub> with scale (c) individual single HNT

### 4.11.1 Formation Mechanism of Hollow Nanostructures of $\text{PbWO}_4$

#### 4.11.1.1 The Kirkendall Effect

The Kirkendall effect is a classical phenomenon in metallurgy [15-18]. It is basically refers to irreversible mutual diffusion process at interface of two metals compounds so that vacancy diffusion occurs to compensate for the inequality of the material flow and the initial interface moves. Prasad and Paul [19] derived the growth rate of the product layer as well as the rate of consumption of core and shell material. Following their formulation, it is possible to determine the radius of the core and shell, and time required to produce a single-phase nanotube.

#### 4.11.1.2 Hollow Nanoparticles

Aldinger was the first to study the hollowing of spherical particles induced by the Kirkendall effect early in 1974 [21]. Only one author Fan Dong was reported the formation of hollow nano particles of  $\text{PbWO}_4$  synthesized by ultrasonic spray pyrolysis method using citric acid surfactant. HNPs produced by them were bigger in size compared to us and have small pores on the surface while HNPs in our case has continuous surface. Formation of hollow nanoparticles (HNPs) in our case (Figure 4.13 (a)) can be explained on the basis of Kirkendall counter diffusion effect. This is a typical ternary compound reaction. In this reaction two reagents  $\text{PbCl}_2$  (compound A) and  $\text{Na}_2\text{WO}_4$  (compound B) sacrifice themselves to produce HNPs of  $\text{PbWO}_4$  (compound AB). We proposed that there are two possible way: Process **A** and Process **B**. Both processes are based on Core/Shell model with difference only in Core and Shell Compound. Process **A** is shown schematically in Figure 4.14. In the Process **A**, (a) initially agglomerated  $\text{PbCl}_2$  molecules behave as a Core and  $\text{Na}_2\text{WO}_4$

molecules gathered around it and form a shell shown in (b).  $\text{Pb}^{2+}$  ions from the core diffuse to the shell side and  $\text{WO}_4^{2-}$  ions from the shell diffuse to the core side. By this way Kirkendall diffusion will take place in the form of two way mass transfer (Wagner counter diffusion) between core and shell compounds. Thus the product  $\text{PbWO}_4$  form at core/shell interface site. Simultaneously  $\text{Na}^+$  move and react with  $\text{Cl}^-$  outer side to form  $\text{NaCl}$  which dissolve in aqueous solution. At the same time small isotropic voids are forms in core contains only  $\text{Cl}^-$  ions shown in (c). Small Kirkendall voids merge into each other and forms larger cavities. If gaps are present at the core/shell interface which appear during the growth,  $\text{Cl}^-$  ions escape from these gaps and direct dissolution of  $\text{Cl}^-$  ions is taking place in solution phase shown in (d), leading to hollowing of the  $\text{PbWO}_4$  NPs shown in (e). HNPs of  $\text{PbWO}_4$  also form via Process B similar way with  $\text{Na}_2\text{WO}_4$  as Core and  $\text{PbCl}_2$  as Shell.

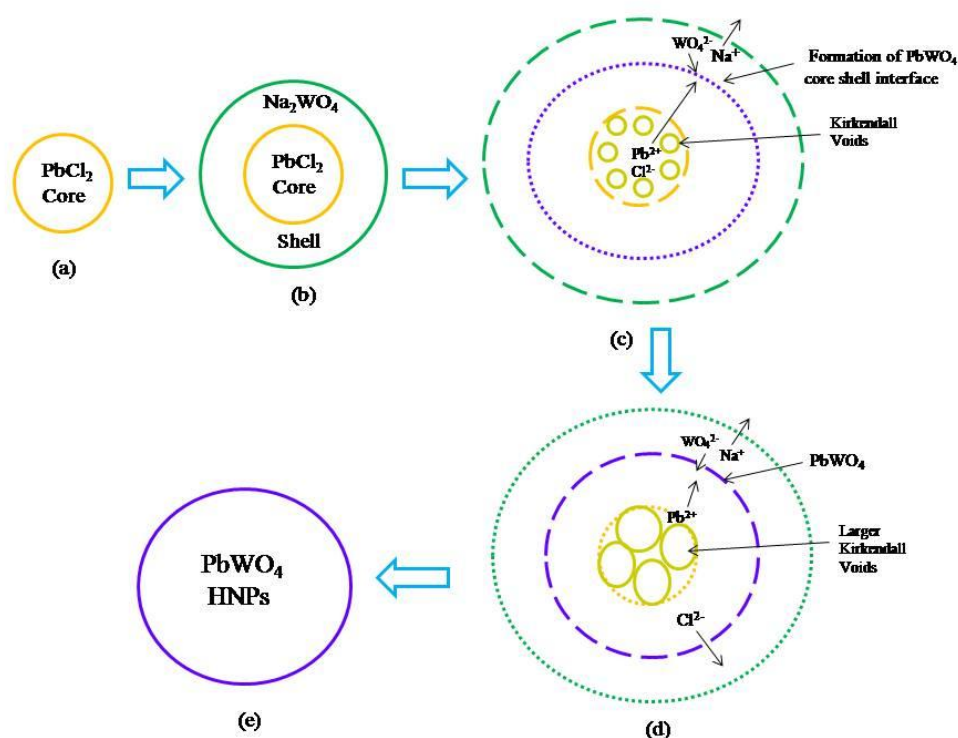


**Figure 4.14** Schematic diagram showing formation of  $\text{PbWO}_4$  Hollow Nano Particles by Process A.

#### 4.11.1.3 Hollow Nanotubes

Formation of  $\text{PbWO}_4$  Hollow Nano Tubes (HNTs) have not been reported yet, hence we are first to synthesis it. Formation tubular Hollow structures based on Kirkendall effect were reported in ref [21-28].  $\text{Ag}_2\text{Se}$  nanotubes are shown in Figure 4.15 to compare it with HNTs  $\text{PbWO}_4$  form in our case [29]. The Kirkendall-based formation route of  $\text{PbWO}_4$  HNPs can also be extended to tubular structures as shown in Figure 4.13(c). The nanotubes have one more degree of freedom and allow material transport along the longitudinal axes. Elimination of the Cl from the core is taking place via open ends of Nanotubes which makes them hollow.

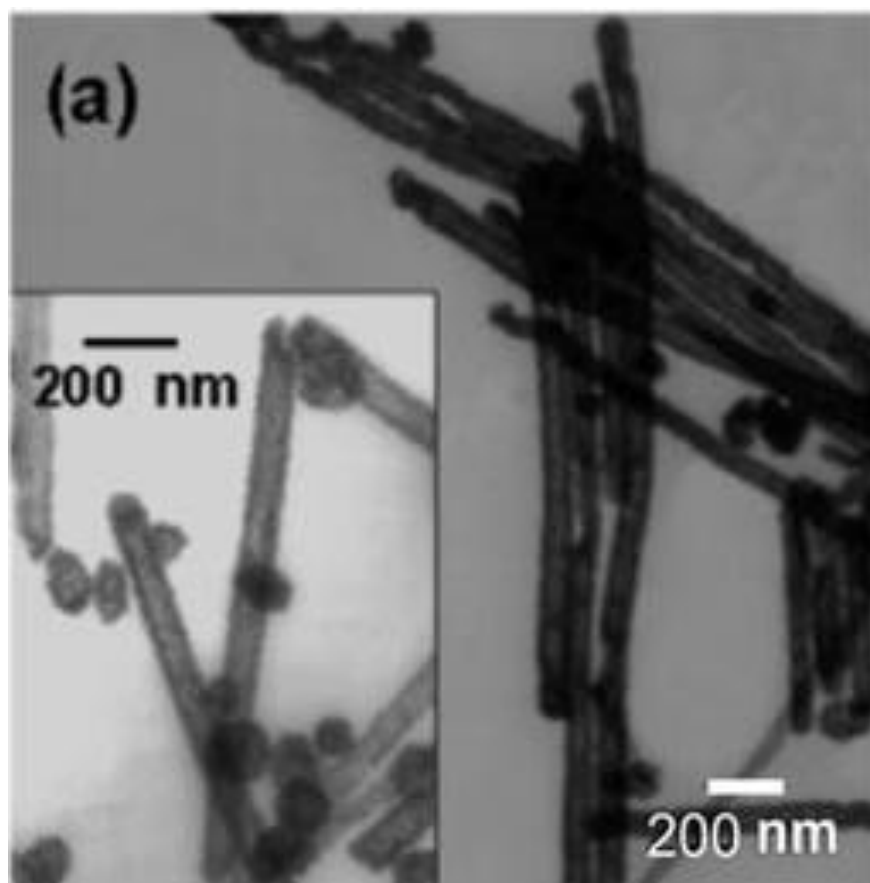


**Figure 4.15** Polycrystalline  $\text{Ag}_2\text{Se}$  nanotubes [29]

From these observations, we can generally conclude that at 7pH, we get mixture of spherical Hollow nanoparticles which act as precursor and they gathered to form hollow nanotubes (HNTs). On increasing the pH of the precursor mixture, we obtained nanorods which are not hollow with increased length. From XRD and TEM analysis we can say that in the 7-11pH range highly crystallized 1-Dimensional  $\text{PbWO}_4$  nanorods with pure stolzite phase obtained. These results indicate that this is the optimal pH range for the formation of  $\text{PbWO}_4$  nanorods.

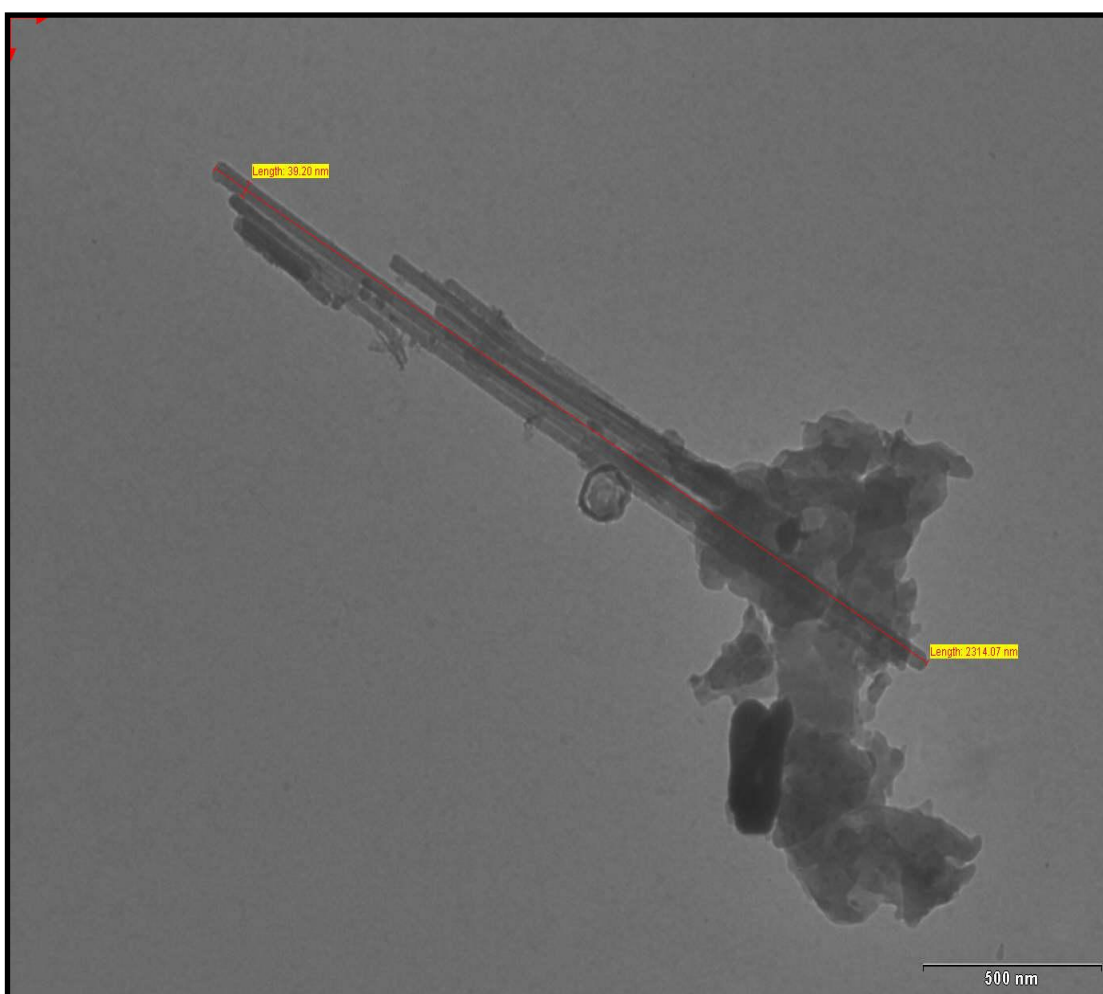
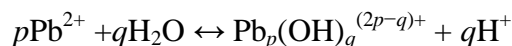


**Figure 4.16** TEM image of agglomerated  $\text{PbWO}_4$  nanorods

### 4.11.2 Formation Mechanism of 1-Dimensional PbWO<sub>4</sub> nanorods: Spherical Diffusion Model

The solid nanorods of PbWO<sub>4</sub> can be thought to be having a habit to form this morphology due to its crystal structures. Yu et al. [30] have recently reported the general synthesis of metal tungstate nanorods by the hydrothermal process without using templates or surfactants and found that the formation mechanism of the nanorods can be explained by the spherical diffusion model well. Anisotropic lateral growth of PbWO<sub>4</sub> nanorods can be explained by Sugimoto's spherical diffusion model [31].

According to spherical diffusion model there is a spherical diffusion layer of solute [Pb<sup>2+</sup> or WO<sub>4</sub><sup>2-</sup>] around each crystal during lateral growth of PbWO<sub>4</sub> nanorods. Solubility is inversely proportional to particle size. As the particle size decreases solubility increases (Gibbs-Thompson law). The concentration of solute within the diffusion layer maintains the solubility of specific crystal face by rapid growth onto or dissolution from the face. The above surfactant\ ligand-free exclusive anisotropic growth of nanorods can be understood from the view point of intrinsic structure of the tungstates. At high pH e.g. at 11pH in our case, Pb<sup>2+</sup> is extensively hydrolyzed [32, 33];



forming “mononuclear” ( $p = 1$ ) and “polynuclear” ( $p > 1$ ) species.

According to Peng et al [34] a higher monomer (Pb<sup>2+</sup>) concentration favors 1D-growth and lower monomer (Pb<sup>2+</sup>) concentration favours 3D-growth. At high pH, Pb<sup>2+</sup> exists as Lead hydroxide complex Pb<sub>p</sub>(OH)<sub>q</sub><sup>(2p-q)+</sup> instead of PbWO<sub>4</sub>, which Lead to a relatively slow release of Pb<sup>2+</sup> and lower Pb<sup>2+</sup> concentration, which result in the formation of larger PbWO<sub>4</sub> particles.

At pH 7 reaction system could provide a higher monomer ( $\text{Pb}^{2+}$ ) concentration due to the relatively weaker metal complexing association and faster release of  $\text{Pb}^{2+}$ . At pH 7, a large amount of  $\text{PbWO}_4$  nuclei produced in the solution leads to form very high supersaturation solution, which advantages the formation of HNTs by assembling  $\text{PbWO}_4$  nanoparticles. Compared with pH 7.0, the pH 11.0 reaction system provides slow release of  $\text{Pb}^{2+}$  and at lower  $\text{Pb}^{2+}$  concentration certain facets to function as a structural directing agent efficiently, resulting in the formation of one-dimensional  $\text{PbWO}_4$  nanorods.

In the present work, it is found that the pH value of reaction system has great influence on the morphologies of the obtained samples, when the other conditions were the same. Regarding the formation mechanism of the  $\text{PbWO}_4$  nanorods through hydrothermal approach, it is clear that the growth process is not surfactant-assisted or template-directed, because no surfactants or templates are introduced into the reaction system. It is noted from our result that with the increase in pH, the size of  $\text{PbWO}_4$  nanoparticles and length of the  $\text{PbWO}_4$  nanotubes increases. Morphology changes from HNTs to Nanorods.

#### 4.12 Effect of Synthesis Temperature on Morphology of PbWO<sub>4</sub>

Temperature-dependent analysis of TEM images was carried out and they show that reaction temperature is another important parameter that affects the morphology of PbWO<sub>4</sub> samples. We assume that the influence of the temperature on the growth of the PbWO<sub>4</sub> crystals may lie in three aspects similar to pH: affecting the adsorption of surfactant to different facets, changing the relative energy of the different facets, and affecting the controlling growth mechanism.

To investigate the effect of temperature on morphology of undoped PbWO<sub>4</sub>, TEM images of samples prepared at two different reaction temperatures were selected i.e 100°C and 125°C and TEM photographs of those samples are shown in Figure 4.17 (a-d). As discussed previously, TEM photographs of product obtained at 100°C temperature under identical solution conditions shows mixture of microparticles of octahedral shape having size around 100 nm as well as aggregation of nanoflakes like structure having width 100-150nm and about few μm in length as shown in Figure 4.17(a-b). When the temperature was raised about 125 °C, Quasi-spherical hollow nanoparticles having average diameter of about 20-40 nm and Hollow Nano Tubes (HNTs) having outer diameter 12.37 nm and around 80-170 nm in length having uniform smooth surface were obtained which is shown in Figure 4.17(c-d). These HNPs and HNTs are highly crystalline compared to product obtained at 100 °C.

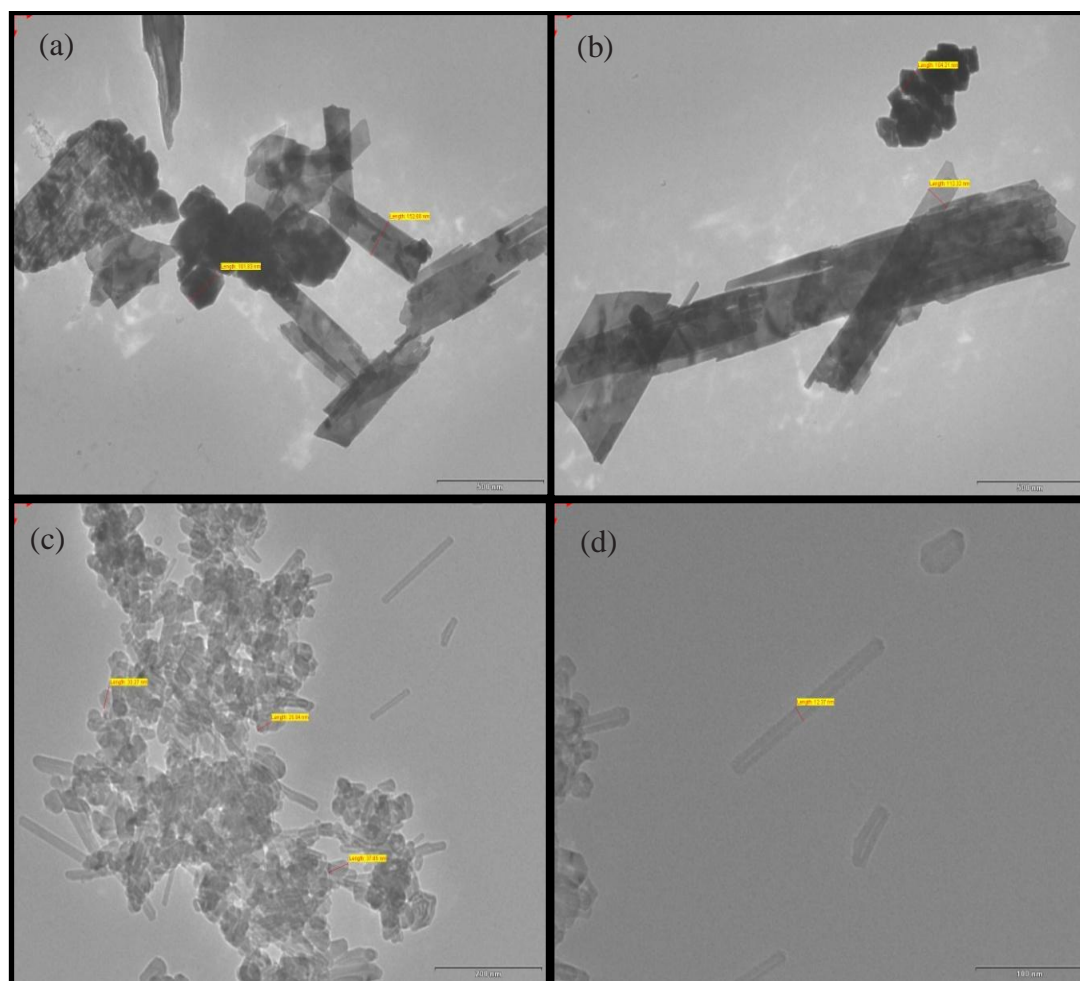


**Figure 4.17** TEM images of  $\text{PbWO}_4$  prepared at (a-b)  $100^\circ\text{C}$  and (c-d)  $125^\circ\text{C}$  temperatures.

Xrd analysis of these samples shows that Octahedraon microparticles and nanoflakes obtained at  $100^\circ\text{C}$  contains mix phases of stolzite and raspite structures, while Hollow nanoparticles and HNTs produced at  $125^\circ\text{C}$  are of pure stolzite phase with high crystallinity. Reasons for production of these morphologies are already discussed in respective sections. Comparison of these products shows that at low temperature (around  $100^\circ\text{C}$ ),  $\text{PbWO}_4$  microstructures containing mix morphologies influenced by raspite as well as stolzite phase will obtained. As we go from low temperature to high temperature raspite phase is diminished and nanostructures with lower dimensions having pure stolzite phase is obtained.

### 4.13 Effect of Synthesis Temperature on morphology of $\text{PbWO}_4:\text{Ce}$

Temperature-dependent analysis of TEM images was also performed for Cerium doped  $\text{PbWO}_4$  samples and it shows that the reaction temperature plays an important role to control the morphology of Cerium doped  $\text{PbWO}_4$  samples. To investigate the effect of temperature of reaction solution on the morphology of  $\text{PbWO}_4:\text{Ce}$ , two reaction temperatures are selected i.e  $100^\circ\text{C}$  and  $200^\circ\text{C}$  and the TEM photographs of obtained product at these two temperatures are shown in Figure 4.18(a-d).

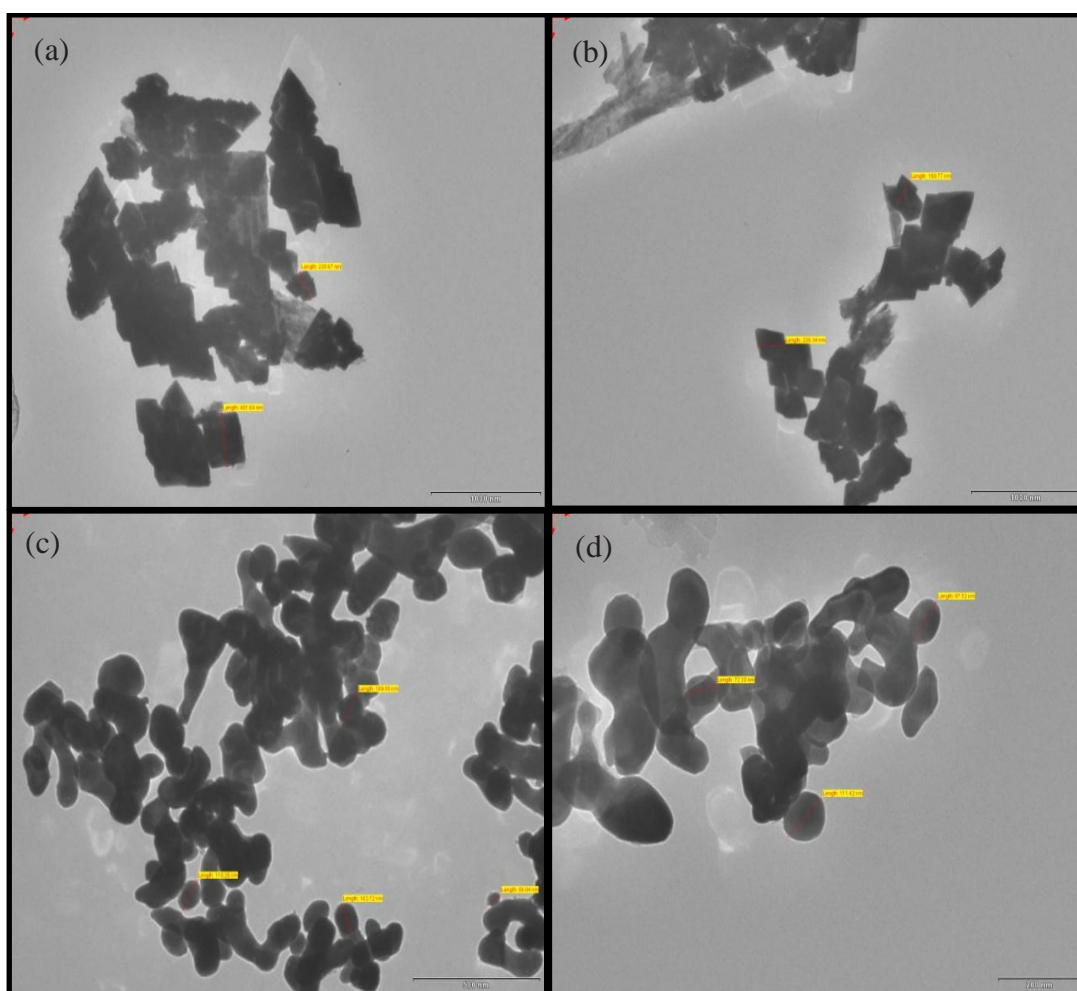


**Figure 4.18** TEM images of  $\text{PbWO}_4:\text{Ce}$  prepared at (a-b)  $100^\circ\text{C}$  and (c-d)  $200^\circ\text{C}$  temperatures.

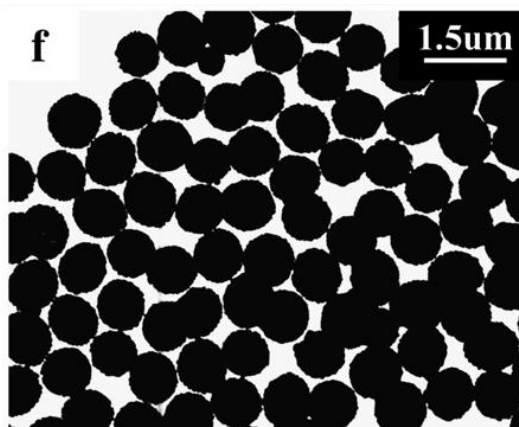


**Figure 4.19** TEM image of  $\text{PbWO}_4$  microparticle synthesized by hydrothermal method using Tripotassium citrate surfactant at  $180^\circ\text{C}$  temperature by Wei Zhao

As discussed previously, doping with cerium in  $\text{PbWO}_4$  at  $100^\circ\text{C}$  produces tetrahedron microparticles having size around 100 nm as shown in Figure 4.18(a-b). Some inclusions of bamboo-leaf-like morphology also present which can be attributed to raspite phase.  $\text{PbWO}_4$  microparticles are attached to each other in an interesting manner. Formation mechanism of this type of dendrite like structure was already explained on the basis of Oswald ripening process followed by oriented attachment of  $\text{PbWO}_4$  microparticles to form dendrite. Figure 4.18(c-d) shows the TEM images of Ce doped  $\text{PbWO}_4$  synthesized at  $200^\circ\text{C}$  temperatures. It is clear from the image that solid spherical nanoparticles are about 50-100 nm in size and they are agglomerated.

X-ray diffraction analysis of these samples shows that Cerium doped  $\text{PbWO}_4$  prepared at  $100^\circ\text{C}$  contains mix phases of stolzite and raspite structures while spherical nanoparticles prepared at  $200^\circ\text{C}$  contains only stolzite phase. The above results indicate that the solution temperature have a certain effect on the morphology along with crystal structure of  $\text{PbWO}_4$ . The formation of spherical particles includes the production of nuclei, their growth and finally their stabilization. It was obviously that the sphere-like products were assembled by the nanoparticles obtained initially,

and we considered that the minimization of the surface energy might be the drive force for the formation of spherical  $\text{PbWO}_4$  nanoparticles. Figure 4.19 shows the TEM photograph of  $\text{PbWO}_4$  microparticle having size about  $1\mu\text{m}$  produced by Wei Zhao by hydrothermal method using Tripotassium citrate surfactant at  $180^\circ\text{C}$  temperature. These microparticles are composed of  $\text{PbWO}_4$  nanorods. Nanospheres obtained in our case (without citrate surfactant) are smaller than that obtained by Wei Zhao. From these results we conclude that raspite phase which exist at low temperature ( $100^\circ\text{C}$ ) vanishes at high temperature ( $200^\circ\text{C}$ ) and to lower the surface energy  $\text{PbWO}_4$  with spherical shape forms.

Thus TEM and SEM analysis of our samples shows that different reaction parameters (pH of reaction solution and Temperature) influence the morphologies of  $\text{PbWO}_4$  and Cerium doped  $\text{PbWO}_4$  to great exchange which is tabulated in Table 4.4.

**Table 4.4** Summary of reaction conditions, phase, morphologies and particle size of undoped and Cerium doped  $\text{PbWO}_4$  prepared using different Lead chloride.

Sample No.	Temp. (°C)	pH	Phase	Morphology	Dimensions
5	100	7	raspite	micro plates	few $\mu\text{m}$
			stolzite	micro particles	100nm
6	100	7	stolzite	tetrahedron	100nm
8	125	7	stolzite	Hollow Spherical Nanoparticles (HNPs)	20-40 nm
			stolzite	Hollow Nano Tubes (HNTs)	12.37 nm (OD) 80-170 nm (L)
9	125	11	stolzite	nano rods	40nm (OD) 2 $\mu\text{m}$ (L)
13	200	7	stolzite	spherical nanoparticles	50-100 nm

## References

1. D.Tawde, M.Srinivas & K.V.R.Murthy, *Physica Status Solidi A*, Vol.208, Issue 4, 803- 807, 2011.
2. Titipun Thongtem, Sulawan Kaowphong, Somchai Thongtem, *Ceramics International* 35, 1103–1108, 2009.
3. Qilin Dai, Hongwei Song, Xinguang Ren, Shaozhe Lu, Guohui Pan, Xue Bai, Biao Dong, Ruifei Qin, Xuesong Qu and Hui Zhang, *J. Phys. Chem. C*, 112, 19694–19698, 2008.
4. Yan Fang, Ying Xiong ,Yuanlin Zhou , Jinxiang Chen, Kaiping Song, Yi Fang, Xulan Zhen, *Solid State Sciences* 11, 1131–1136, 2009.
5. Jinhu Yang, Conghua Lu, Hong Su, Jiming Ma, Humin Cheng, Limin Qi, *Nanotechnology* 19, 035608, 2008.
6. Thresiamma George, Sunny Joseph, Anu Tresa Sunny, Suresh Mathew, *J Nanopart Res* 10, 567–575, 2008.
7. Chunhua Zheng, Chenguo Hu, Xueyan Chen, Hong liu, Yufeng Xiong, Jing Xu, Buyong Wana and Linyong Huang, *CrystEngComm* 12, 3277–3282, 2010.
8. A. Kshetov and N. A. Gorbatyi, *Russ. Phys. J.*, 20, 860,1969.
9. Biao Liu, Shu-Hong Yu, Linjie Li, Qiao Zhang, Fen Zhang, and Ke Jiang, *Angew. Chem.* 116, 4849 –4854, 2004.
10. T. Sugimoto, *Adv. Colloid Interface Sci.* 28,65,1987.
11. J.W. Mullin, *Crystallization*, third ed, Butterworth-Heinemann, Oxford, 1997.
12. Guangjun Zhou , Mengkai Lu, Benyu Su, Feng Gu, Zhiliang Xiu , Shufen Wang, *Optical Materials* 28, 1385–1388, 2006.
13. Guangjun Zhou, MengkaiLu, Feng Gu, Dong Xu, Duorong Yuan , *Journal of Crystal Growth* 276 , 577–582, 2005.
14. Changhua An, Kaibin Tang, Guozhen Shen, Chunrui Wang, Yitai Qian, *Materials Letters* 57, 565– 568, 2002.

15. E. O. Kirkendall, Trans. AIME, 147, 104, 1942.
16. A. D. Smigelskas, E. O. Kirkendall, Trans. AIME, 171, 130, 1947.
17. H. Nakajima, J. Miner. Met. Mater. Soc. 49, 15, 1997.
18. A. Paul, PhD thesis, Technische Universiteit Eindhoven, The Netherlands, 2004.
19. S. Prasad, A. Paul, Appl. Phys. Lett., 90, 233114, 2007.
20. F. Aldinger, Acta Metal., 22, 923, 1974.
21. Q. Li, R. M. Penner, Nano Lett., 5, 1720, 2005.
22. H. J. Fan, M. Knez, R. Scholz, K. Nielsch, E. Pippel, D. Hesse, M. Zacharias, U. Gçsele, Nat. Mater., 5, 627, 2006.
23. H. Tan, S. P. Li, W. Y. Fan, J. Phys. Chem. B, 110, 15812, 2006.
24. C. H. B. Ng, H. Tan, W. Y. Fan, Langmuir, 22, 9712, 2006.
25. J. Zhou, J. Liu, X. D. Wang, J. H. Song, R. Tummala, N. S. Xu, Z. L. Wang, Small, 3, 622, 2007.
26. X. Y. Chen, Z. J. Zhang, Z. G. Qiu, C. W. Shi, X. L. Li, J. Colloid Interface Sci., 308 271, 2007.
27. Y. Chang, M. L. Lye, H. C. Zeng, Langmuir 2005, 21, 3746.
28. Q. Wang, J. X. Li, G. D. Li, X. J. Cao, K. J. Wang, J. S. Che, J. Cryst. Growth, 299, 386, 2007.
29. C. H. B. Ng, H. Tan, W. Y. Fan, Langmuir, 22, 9712, 2006.
30. S. H. Yu, B. Liu, M. S. Mo, J. H. Huang, X. M. Liu, Y. T. Qian, Adv. Funct. Mater. 13, 639, 2003.
31. T. Sugimoto, Photog. Sci. Eng., 28, 137, 1984.
32. D. T. Richens, The Chemistry of Aqua Ions, Wiley, New York, 1997.
33. G. Zhou, M. Lu, F. Gu, D. Xu, D. R. Yuan, J. Cryst. Growth 276, 577, 2005.
34. Peng, Z. A.; Peng, X. G. J. Am. Chem. Soc., 123, 1389, 2001.

## 5.1 Luminescence

It is the phenomenon in which electronic states of solid are excited by some energy sources (Infrared, ultraviolet, visible light for PL and heating in TL) and excitation energy is re-emitted as a light of longer wavelength (Stokes Law). Light is directed onto a sample, where it is absorbed and imparts excess energy into the material in a process called photo-excitation. One way this excess energy can be dissipated by the sample is through the emission of light, or *luminescence*. In the case of photo-excitation, this luminescence is called *photoluminescence*. Photo-excitation causes electrons within a material to move into permissible excited states. When these electrons return to their equilibrium states, the excess energy is released and may include the emission of light (a radiative process) or may not (a non-radiative process). The energy of the emitted light (photoluminescence) relates to the difference in energy levels between the two electron states involved in the transition between the excited state and the equilibrium state. The quantity of the emitted light is related to the relative contribution of the radiative process. Photoluminescence spectroscopy is a contactless, non-destructive method of probing the electronic structure of materials.

The optical properties of  $\text{PbWO}_4$  nanomaterial are different than that of the bulk material. It is observed that with decrease in size optical absorption band shifts to the blue side. This is ascribed to the quantum size effect which can well explained by electron in a box model. Due to their spatial confinement the kinetic energy of electron increases. This results in a broadening of band gap.

## 5.2 General characteristics of Photoluminescence spectra of $\text{PbWO}_4$

The emission spectra of scheelite tungstates  $\text{AWO}_4$  ( $A = \text{Pb}, \text{Cd}, \text{Ba}, \text{Ca}, \text{etc.}$ ) exhibit always broad luminescence band in the blue spectral region.  $\text{PbWO}_4$  at room temperature exhibits  $\text{ABO}_4$  crystal structure with tetragonal unit cell with  $\text{A}^{2+}$  ( $\text{Pb}^{2+}$ ) as cation and a tetrahedral  $\text{BO}_4^{-2}$  ( $\text{WO}_4^{-2}$ ) as anion. The tetrahedrons consist of a  $\text{W}^{6+}$  ion at the center, surrounded by four  $\text{O}^{2-}$  ions. It is well known that the luminescence spectrum of PWO is composed of two main bands; the “blue” one peaking around 420 nm and the “green” one peaking between 490 and 540 nm. There are two defects: 1. a regular lattice  $(\text{WO}_4)^{-2}$  defect and 2. a defect based  $\text{WO}_3$  center, which are responsible for the complex character of  $\text{PbWO}_4$  emission. The blue luminescence is an intrinsic feature of PWO, and is generally ascribed to the radiative decay of a self-trapped exciton that locates on the regular  $\text{WO}_4$  group [1]. The green luminescence is of extrinsic origin and it was ascribed to a defect based  $\text{WO}_3$  center [2] possibly with F center [3]. The concentration of these defects are strongly influenced by the raw material and the method used for the crystal growth.

### 5.3 Electronic Structure of $\text{PbWO}_4$

According to the band theory given by C.Zheng et al., the bottom of conduction band (CB) is formed by both 5d state of  $\text{W}^{6+}$  ion and 6p state of  $\text{Pb}^{2+}$  ion in  $\text{PbWO}_4$ , and the coping of valence band (VB) is formed by both 6s state of the  $\text{Pb}^{2+}$  ion and 2p state of  $\text{O}^{2-}$  ion, as shown in Figure 5.1.

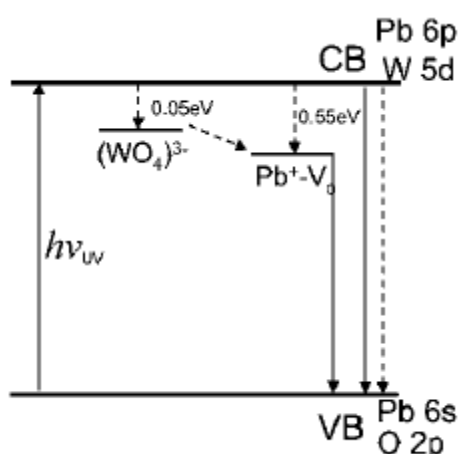


**Figure 5.1** Band Structure of  $\text{PbWO}_4$

The  $\text{W}5\text{d}$  states are degenerated and split in a crystal field of tetragonal symmetry in  $e$  and  $t_2$  vibrational modes. The  $\text{Pb}^{2+}$  6s state and  $\text{Pb}^{2+}$  6p state have appreciable contributions throughout the valence band and conduction band, respectively. The valence-band width is calculated to be 5.5 eV. The  $\text{Pb}^{2+}$  6s state forms a narrow band 1 eV below the bottom of the valence band.

When the  $\text{PbWO}_4$  is excited within fundamental absorption band, charge transfer by two types of electronic transitions can be observed,

- (i) From  $\text{O}^{2-}$  to  $\text{W}^{6+}$  within  $\text{WO}_4^{2-}$  oxyanion complex
- (ii) From  $\text{O}^{2-}$  to  $\text{Pb}^{2+}$  outside  $\text{WO}_4^{2-}$  oxyanion complex

## 5.4 Self Trapped Exciton (STE)

An electron from oxygen 2p goes into one of the empty tungsten 5d orbital (the bottom of W5d) in the  $WO_4^{2-}$  group by absorbing ultraviolet irradiation in  $PbWO_4$ . In the excited state of the  $WO_4^{2-}$  group, the hole (on the oxygen) and the electron (on the tungsten) remain together as an exciton because of their strong interactions. This type of exciton which is produced in  $PbWO_4$  is called Frenkel exciton. The exciton binding energy was estimated as being about 0.1 eV. The lowest exciton transition is connected to an electronic excitation from the mixed  $Pb(6s) \rightarrow O(2p)$  ground states to the mixed  $Pb(6p) \rightarrow W(5d)$  excited states. As the Pb contributions to the top of the valence band and the bottom of the conduction band are small in raspite compared to scheelite so the exciton transition in raspite is very weak. That is to say, the raspite exciton is a molecular-type exciton of the  $WO_6$ -anion complex with mainly covalent bonding within the oxo-complex. The electronic band structures of both phases are, as a whole, similar to each other except exciton transition.

## 5.5 Crystal-field splitting and hybridization of the molecular orbital of $\text{WO}_4^{2-}$ tetrahedral group

In Figure 5.2, the schematic diagram of a crystal field splitting and hybridization of the molecular orbitals of an oxyanion tetrahedral complex is shown.

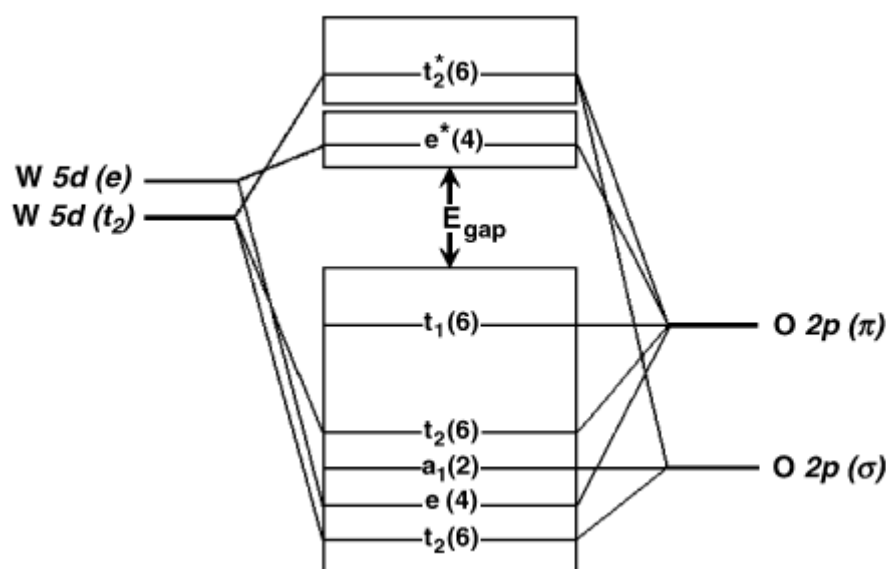


**Figure 5.2** schematic diagram of a crystal field splitting and hybridization  $\text{WO}_4^{2-}$  group [4].

The crystal-field splitting and hybridization of the molecular orbitals of  $\text{WO}_4^{2-}$  tetrahedral are shown in Figure 5.2. The  $\text{W}5d(t_2)$  and  $\text{W}5d(e)$  orbitals are hybridized with the  $\text{O}2p(\sigma)$  and  $\text{O}2p(\pi)$  ligand orbitals to form  $\text{WO}_4^{2-}$  tetrahedra. The four ligand  $2p(\sigma)$  orbitals are compatible with the tetrahedral representation for  $a_1$  and  $t_2$  symmetries and the eight ligand  $2p(\pi)$  orbitals are for  $t_1$ ,  $t_2$  and  $e$  symmetries. The top occupied state has  $t_1$  symmetry formed from  $\text{O}2p(\pi)$  states. The lowest unoccupied state has  $e$  symmetry formed from a combination of the  $\text{W}5d(e)$  and  $\text{O}2p(\pi)$  orbitals to give antibonding (\*). The hybridization between the  $\text{W}5d$  and  $\text{O}2p$  orbitals is specified as covalent bonding between the ions. For ground state

system, all one-electron states below band gap are filled to give a many electron  $^1A_1$  state. At the lowest excited state, there is one hole in  $t_1$  (primarily O 2p( $\pi$ )) state and one electron in  $e$  (primarily W5d) state which give rise to many-electron  $^1T_1$ ,  $^3T_1$ ,  $^1T_2$  and  $^3T_2$  states. Among them, only  $^1T_2 \rightarrow ^1A_1$  transition is electric dipole allow [4, 5]. However, due to the inducement of Jahn–Teller effect [6] and electron–phonon interactions [7], the  $WO_4^{2-}$  complex in many tungstate crystals was slightly distorted from  $T_d$  to  $D_{2d}$  symmetry so that the inhibited transitions of  $WO_4^{2-}$  complex, such as  $^1T_2$ ,  $^1T_1$ ,  $^3T_2$  and  $^3T_1$  to  $^1A_1$ , became partially allowable.

## 5.6 Cerium

The rare earth (RE) ions most commonly used for applications as phosphors, lasers, and amplifiers are the so-called lanthanide ions. The ground state of all the Lanthanide atoms is probably either  $[\text{Xe}] 4f^n 5d^1 6s^2$  or  $[\text{Xe}] 4f^{n+1} 6s^2$ , where the increase in  $n$  from 0 to 14 corresponds to the change from La ( $Z=57$ ) through to Lu ( $Z=71$ ). Rare earth ions have unfilled optically active  $4f$  electrons screened by outer electronic filled shells. Because of these unfilled shells, these kinds of ions are usually called *paramagnetic ions*.

Cerium is the most abundant member of the series of elements known as lanthanides or rare earths. Cerium is the second and most reactive member of the lanthanides series. Cerium is characterized chemically by having two stable valence states one is  $\text{Ce}^{4+}$ , *ceric*, and the other is  $\text{Ce}^{3+}$ , *cerous*. The cerium atom ( $Z=58$ ), which has an outer electronic configuration  $[\text{Xe}]4f^1$  i.e.  $5s^2 5p^6 5d^1 4f^1 6s^2$ . It is very electro-positive and has predominantly ionic chemistry due to the low ionization potential for the removal of the three most weakly bound electrons. These atoms are usually incorporated in crystals as trivalent cations i.e.  $\text{Ce}^{3+}$ .

In trivalent ions  $5d$ ,  $6s$ , and some  $4f$  electrons are removed and so  $(\text{RE})^{3+}$  ions deal with transitions between electronic energy sublevels of the  $4f^n$  electronic configuration. The  $4f^n$  electrons are, in fact, the valence electrons that are responsible for the optical transitions. These valence electrons are shielded by the  $5s$  and  $5p$  outer electrons of the  $5s^2 5p^6$  less energetic configurations. Because of this shielding effect, the valence electrons of  $\text{Ce}^{3+}$  ion are weakly affected by the ligand ions in  $\text{PbWO}_4$  crystals; a situation results the case of a weak crystalline field. For Weak crystalline field:  $H_{\text{CF}} \leq H_{\text{SO}}, H_{\text{ee}}, H_{\text{O}}$ . Consequently, the spin-orbit interaction term of the free  $\text{Ce}^{3+}$  ion Hamiltonian is dominant over the crystalline field Hamiltonian term. In this case, the energy levels of the free  $\text{Ce}^{3+}$  ion are only slightly perturbed (shifted and split) by the crystalline field. This causes the  $^{2S+1}L_J$  states of the  $(\text{RE})^{3+}$

ions to be slightly perturbed when these ions are incorporated in crystals. The effect of the crystal field is to produce a slight shift in the energy of these states and to cause additional level splitting. However, the amount of this shift and the splitting energy are much smaller than the spin-orbit splitting, and thus, the optical spectra of  $(RE)^{3+}$  ions are fairly similar to those expected for free ions. The free ion wavefunction are then used as basis functions to apply perturbation theory,  $H_{CF}$  being the perturbation Hamiltonian over the  $^{2S+1}L_J$  states (where S and L are the spin and orbital angular momenta and  $J = L + S$ ). This approach is generally applied to describe the energy levels of trivalent rare earth ions, since for these ions the 4f valence electrons are screened by the outer  $5s^2 5p^6$  electrons. These electrons partially shield the crystalline field created by the B ions).

## 5.7 Luminescence of PbWO<sub>4</sub> due to Scheelite phase

### 5.7.1 Blue emission

The lowest exciton of PWO is mainly characterized by  $6s^2 \rightarrow 6s6p$  cationic transitions in Pb<sup>2+</sup> ions. It is thus believed that the excitons or electron-hole pairs generated optically on Pb<sup>2+</sup> ions move to the regular WO<sub>4</sub><sup>2-</sup> groups, to emit the blue Luminescence [8].

Scheelite phase of PbWO<sub>4</sub> gives rise to the luminescence blue band at 2.80 eV (440nm) when excitation energy is in exciton band region (4 to 5 eV) (250-300nm). This luminescence has been regarded as being an intrinsic feature of Scheelite phase of PbWO<sub>4</sub>. The 2.80-eV luminescence is ascribed to the radiative decay of self-trapped (localized) excitons in regular WO<sub>4</sub><sup>2-</sup> group. J. A. Groenink and G. Blasse [9] conclude that the blue emission with maximum at 420 nm, is due to transitions in the regular tungsten [WO<sub>4</sub><sup>2-</sup>] group in which the Pb<sup>2+</sup> play a role.

### 5.7.2 Green emission

The origin of green emission of PbWO<sub>4</sub> was reported in many papers. However the defects responsible for the origin of green emission are controversial and still under discussion.

### 5.7.3 Two Green emission bands G(I) and G(II)

The presence of two green emission bands at Room Temperature was reported [10-13].

### 5.7.4 G(I) emission band

The G(I) emission band, observed at low temperatures, located around 2.3–2.4 eV (510-530 nm) and excited around 3.9 eV (310 nm) in undoped crystals is assumed to arise from the [WO<sub>4</sub><sup>2-</sup>] groups located in the crystal regions of lead-deficient structure.

### 5.7.5 G(II) emission band

The G(II) emission band, observed at high temperatures ( $T > 160\text{K}$ ) located at 2.5 eV (495 nm) appears under excitation around 4.07 eV (310nm) observed due to isolated oxygen vacancies in irregular  $\text{WO}_3$  groups also called F-centers [14-19]. Green emission was also connected with raspite inclusions produce due to thermal stress during crystal growth process [20-22]. The green emission was ascribed to the  $\text{MoO}_4^{2-}$  anion groups which is a stable electron trap [23-27]. It was suggested that  $\text{Mo}^{6+}$  ions are present not only in the  $\text{Mo}^{6+}$ -doped crystals but also in undoped crystals. The molybdenum ion is chemically very similar to the tungsten ion it is difficult to separate in the course of raw material preparation. The molybdenum impurity is usually present in  $\text{PbWO}_4$  at the level of  $< 1$  ppm. The presence in the lead-deficient  $\text{PbWO}_4$  crystals of the superstructure of the type of  $\text{Pb}_{7.5}\text{W}_8\text{O}_{32}$  was reported in Ref.[28]. In Ref. [29], this superstructure was assumed to be responsible for the green emission. In Refs.[30], the green emission was connected with defects of the type of  $\{\text{WO}_4 + \text{O}_i\}$ . According to C.Shi. green luminescence is not produced by  $(\text{WO}_3 + \text{F})$  centers lacking oxygen but probably arises from  $(\text{WO}_4 + \text{O}_i)$  centers ( $\text{O}_i$ - Oxygen interstice) with an excess local oxygen.

## 5.8 Effect of Lead Source on PhotoLuminescence of PbWO<sub>4</sub> Phosphor

Sun et al. [31] showed that PL emission of SrWO<sub>4</sub> can be modified by the morphology. According to him different morphologies contribute to the formation of different surface defects that influence in the PL behaviour.

SEM and TEM analysis of undoped as well as Cerium doped PbWO<sub>4</sub> reveals that different Lead sources produce various morphologies of PbWO<sub>4</sub> as shown in below Table 5.1.

**Table 5.1** Summary of Phase produced, Morphologies and Particle size of undoped and Cerium doped PbWO<sub>4</sub> prepared using different Lead sources.

Lead Source	Dopant	Phase	Morphology	Dimension
Pb(CH <sub>3</sub> COO) <sub>2</sub>	-	stolzite	dendrite	1 μm
		stolzite	tetrahedron	500nm
Pb(CH <sub>3</sub> COO) <sub>2</sub>	CeO <sub>2</sub>	raspite	flat nanobelt	5 μm x 1 μm
		stolzite	octahedron microparticles	1.5 μm
Pb(NO <sub>3</sub> ) <sub>2</sub>	-	raspite	flat nanobelt	5 μm x 1 μm
		stolzite	six branched dendrites	2 μm
		stolzite	rhombic particles	500nm
Pb(NO <sub>3</sub> ) <sub>2</sub>	CeO <sub>2</sub>	stolzite	tetrahedron	100nm
PbCl <sub>2</sub>	-	raspite	micro plates	few μm
		stolzite	micro particles	100nm
PbCl <sub>2</sub>	CeO <sub>2</sub>	stolzite	tetrahedron	100nm

### 5.8.1 Lead Acetate and Lead Nitrate as Lead Sources

The effect of different lead sources [ $\text{Pb}(\text{CH}_3\text{COO})_2$ ,  $\text{Pb}(\text{NO}_3)_2$  and  $\text{PbCl}_2$ ] on the formation of  $\text{PbWO}_4$  and  $\text{PbWO}_4:\text{Ce}$  were investigated from Photoluminescence characterization. Photoluminescence property of undoped and Cerium doped  $\text{PbWO}_4$  prepared with different Lead sources at  $100^\circ\text{C}$  is studied and discussed below.

As discussed in the previous chapters, when  $\text{Pb}(\text{CH}_3\text{COO})_2$  was used as the lead source, product with mixture of two phases (stolzite and raspite) were produced. Dendrite and tetrahedron type morphology is produced due to stolzite phase. On doping with Cerium, flat nanobelt due to raspite phase and Octahedron shaped microparticles due to stolzite phase are obtained. Figure 5.3(a) represents the PL spectra of as synthesised products. When  $\text{Pb}(\text{NO}_3)_2$  was used as the lead source, six branched dendrite and rhombic shaped particles of  $\text{PbWO}_4$  are produced due to stolzite phase and flat nanobelt are produced due to raspite phase. Doping of Cerium in  $\text{PbWO}_4$  produces tetrahedron shaped particles due to stolzite phase. PL spectra of as synthesised products are shown in Figure 5.3(b). When  $\text{PbCl}_2$  used as lead source, microparticles of  $\text{PbWO}_4$  are produced due to stolzite phase and flat microbelts are produced due to raspite phase. When Cerium was doped in  $\text{PbWO}_4$ , tetrahedron shaped particles with stolzite phase were produced. Figure 5.3(c) represents the PL spectra of as synthesised products. In general, two phases (stolzite and raspite) are produced in all the samples irrespective of Lead sources and both the phase produces have different morphologies of  $\text{PbWO}_4$  phosphor in micrometer range.

First we will discuss our published result [32] of PL spectra of undoped and cerium-doped  $\text{PbWO}_4$  by using lead acetate and lead nitrate as lead sources. The PL spectra of undoped and cerium-doped  $\text{PbWO}_4$  by using lead chloride as a lead source will be discussed later separately.

The PL spectra of undoped and cerium-doped  $\text{PbWO}_4$  were investigated at room temperature using a 305-nm excitation wavelength. Comparison of PL spectra of two lead sources (Lead Acetate and Lead Nitrate) is shown in Figure 5.3(a). The effect of cerium doping on PL spectra of  $\text{PbWO}_4$  prepared by using lead acetate and lead nitrate is shown in Figure 5.3(b) and Figure 5.3(c), respectively.

Literature survey reveals that the emission spectra of  $\text{PbWO}_4$  consists of two components, a fast blue component around 450 nm which is an intrinsic feature of scheelite phase and a slow green one around 480–520 nm which is an intrinsic feature of rhabdophane phase. The broad blue–green emission band around 450–550 nm is observed in all four samples which is in good agreement with reported values [33]. A broad blue luminescence peak around 450 nm is observed in all samples which originate from tetragonal  $\text{WO}_4^{2-}$  groups [34]. The origin of such complex spectra is already discussed in the beginning of this chapter. Effect of different morphologies on photoluminescence emission of  $\text{PbWO}_4$  and cerium-doped  $\text{PbWO}_4$  is the main motive of this part of our experiment.

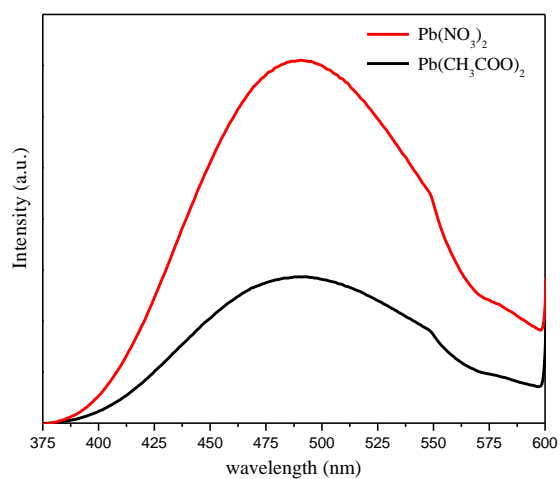


Figure 5.3(a) PL spectra of  $\text{PbWO}_4$  synthesized with different Lead Sources

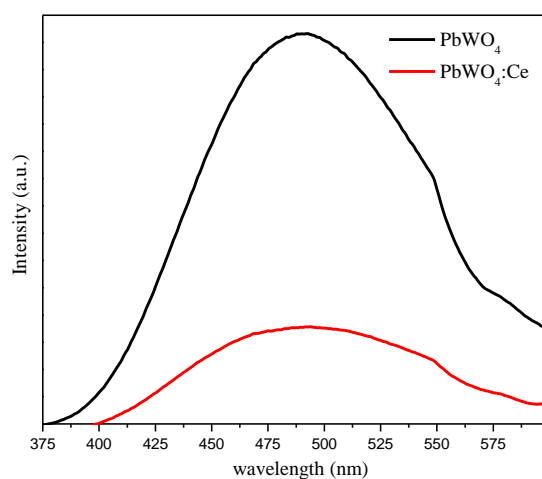


Figure 5.3(b) PL spectra of  $\text{PbWO}_4$  synthesized with Lead Acetate

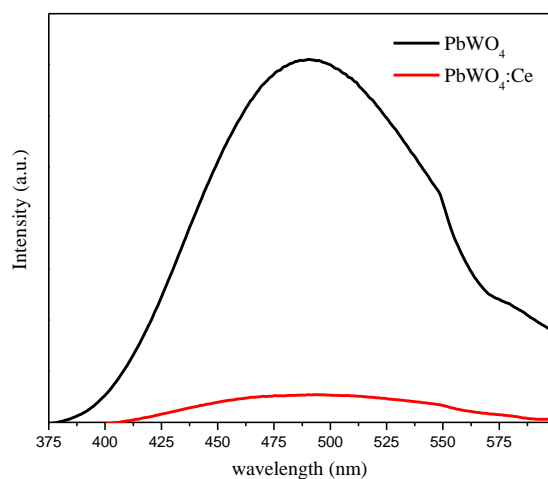


Figure 5.3(c) PL spectra of  $\text{PbWO}_4$  synthesized with Lead Nitrate

Comparison of Photoluminescence spectra of  $\text{PbWO}_4$  microcrystallites clearly shows the variation in PL intensity. The PL intensity is higher for  $\text{PbWO}_4$  prepared with lead nitrate and low for  $\text{PbWO}_4$  prepared with lead acetate as shown in Figure 5.3(a).  $\text{PbWO}_4$  prepared with lead nitrate has mixed morphologies (six branched dendrite + rhombic nanoparticles + nanobelt) and  $\text{PbWO}_4$  prepared with lead acetate also possesses mixed morphologies (single branched dendrite + tetrahedron microparticles). The dendrite with six branched structure has highest surface to volume ratio among all the morphologies produced here [35]. Rhombic shaped nanoparticles and nanobelt also have higher surface area compared to single branched dendrite and tetrahedron microparticles. Higher the surface to volume ratio means higher concentration of surface related defects (particularly oxygen vacancies) and hence high light collection efficiency. These characteristics enhance PL emission in  $\text{PbWO}_4$  prepared with lead nitrate compared to  $\text{PbWO}_4$  prepared with lead acetate.

The intensity of PL is suppressed to a great extent by doping with cerium which is shown in Figure 5.3(b) and Figure 5.3(c). The cerium doped  $\text{PbWO}_4$  shows weaker luminescence intensity than that of undoped  $\text{PbWO}_4$ .  $\text{Ce}^{3+}$  ( $4f^1$ ) is the most simple rare earth ion with one electron case having excited configuration  $5d^1$ . As discussed earlier in  $\text{Ce}^{3+}$  spin orbit interaction is dominant over crystal field interaction, hence energy levels of  $\text{Ce}^{3+}$  ion are not perturbed by  $\text{PbWO}_4$  crystal field. The  $4f^1$  ground state configuration yields two levels:  $^2F_{5/2}$  and  $^2F_{7/2}$  due to spin orbit coupling and the  $5d^1$  configuration is split by the crystal field in 2 to 5 components between the band gap of  $\text{PbWO}_4$ . The emission occurs from the lowest crystal field component of the  $5d^1$  configuration to the two levels of the ground state. Since the  $5d \rightarrow 4f$  transitions are parity allowed and spin selection is not appropriate, the emission transition is a fully allowed one. The reduction in PL intensity is due to these nonradiative  $5d \rightarrow 4f$  transition in the cerium doped  $\text{PbWO}_4$ . Therefore  $\text{Ce}^{3+}$  ions could serve as efficient non-radiative traps in  $\text{PbWO}_4$  crystal lattice [36].

The green emission of undoped crystals was ascribed to the  $\text{WO}_3$  oxygen-deficient complex anion in scheelite phase [37]. This emission was connected with the inclusions of the raspite structure formed due to the thermal stress appearing in the process of crystal growth [38]. PL intensity of  $\text{PbWO}_4:\text{Ce}$  prepared with lead acetate is more compared to  $\text{PbWO}_4:\text{Ce}$  prepared with lead nitrate. Structural investigation of Cerium doped samples shows that  $\text{PbWO}_4:\text{Ce}$  prepared with lead acetate contains more inclusions of raspite phase as compared to  $\text{PbWO}_4:\text{Ce}$  prepared with lead nitrate.

### 5.8.2 Lead Chloride as a Lead Source

According to our literature survey no one has prepared  $\text{PbWO}_4$  by using Lead chloride as a lead source except Changhua An et al. [39]. In his paper he compared the PL spectra of  $\text{PbWO}_4$  prepared with two different lead sources, Lead Nitrate and Lead Chloride. He found that the PL emission of  $\text{PbWO}_4$  prepared with Lead Chloride has highest intensity compared to  $\text{PbWO}_4$  prepared with Lead Nitrate. Enhancement of PL intensity due to Lead Chloride as a lead source to synthesis  $\text{PbWO}_4$  encourage us to do further investigation reported in this thesis.

Figure 5.4 shows room temperature PL emission spectra of  $\text{PbWO}_4$  and Cerium doped  $\text{PbWO}_4$  prepared using  $\text{PbCl}_2$  as lead source with excitation wavelength 254 nm. PL spectra of  $\text{PbWO}_4$  samples prepared with  $\text{PbCl}_2$  are somewhat different than that prepared with Lead acetate and Lead nitrate.

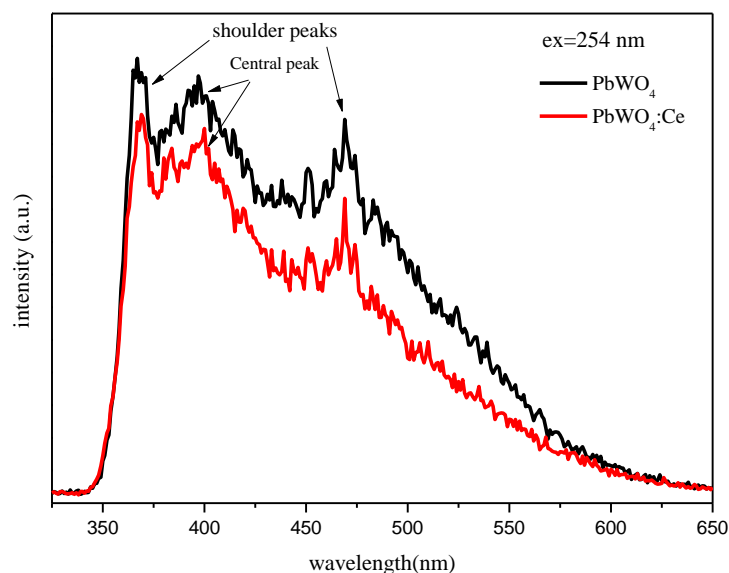


Figure 2. PL spectra of  $\text{PbWO}_4$  prepared with Lead Chloride

**Figure 5.4** PL spectra of  $\text{PbWO}_4$  prepared with Lead Chloride at  $100^\circ\text{C}$

As expected both samples show broad blue-green emission in visible region. The PL spectra has “*spread-eagle-shape*” with a central peak surrounded by two broad shoulder peaks. Emission spectrum reveals that it is composed of several sub-bands which are almost distributed throughout entire 350-550 nm region.

According to morphological studies of these samples shows that when  $\text{PbCl}_2$  used as lead source, microparticles of  $\text{PbWO}_4$  are produced due to stolzite phase and flat microbelts are produced due to raspite phase. When Cerium doped in  $\text{PbWO}_4$ , tetrahedron shaped particles with stolzite phase were produced. The decomposition of PL spectra into individual Gaussian components results four Gaussians to achieve a good agreement with the experimental data. In order to do detailed analysis of luminescence spectra it is fitted with four individual Gaussian components shown in Figure 5.4(a) and Figure 5.4(b) and named Gaussian peak I, II, III and IV respectively. Variation in locations and intensity of strongly overlapped Gaussian components of photoluminescence spectra of  $\text{PbWO}_4$  and  $\text{PbWO}_4:\text{Ce}$  prepared at  $100^\circ\text{C}$  is shown in Table 5.2 and discussed here.

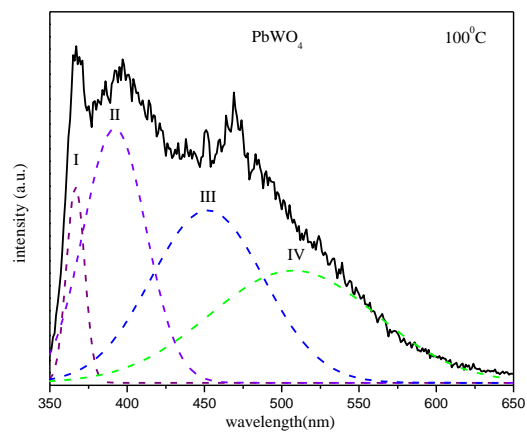


Figure.5.4(a)

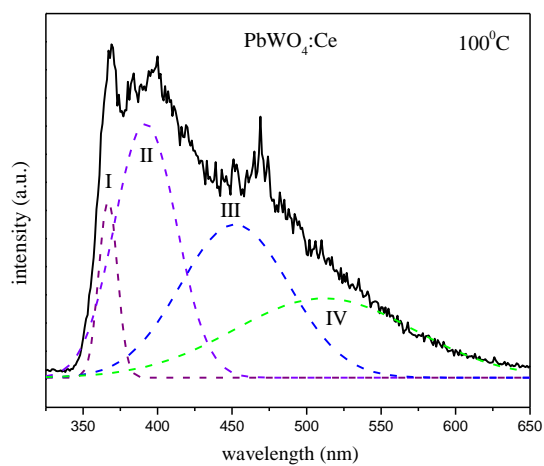


Figure 5.4(b)

**Table 5.2** The locations and Intensity of Gaussian components of PL spectra of  $\text{PbWO}_4$  and  $\text{PbWO}_4:\text{Ce}$  prepared at  $100^\circ\text{C}$ .

Temp. 100 (°C)	Gaussian peak I		Gaussian peak II		Gaussian peak III		Gaussian peak IV	
	wavelength (nm)	intensity (a.u.)	wavelength (nm)	intensity (a.u.)	wavelength (nm)	intensity (a.u.)	wavelength (nm)	intensity (a.u.)
PWO	367	40	392	52	452	35	507	23
PWO:Ce	367	32	392	45	452	27	512	14

Photoluminescence emission spectra shows structured character for both undoped and cerium doped samples. Such type of structural shape invokes presence of four Gaussian components: three peaks fall in blue region and one in green region. The presence of four Gaussian components indicates the excited states of emission center are relaxed and degenerated under the influence by some type of perturbation.

It is already discussed that blue emission is attributed to the radiative recombination of STE localized in regular  $\text{WO}_4^{2-}$  complex of scheelite phase. Isolated  $\text{WO}_4^{2-}$  complex has tetrahedral symmetry  $T_d$  with ground state configuration  $(t_1)^6(e)^0$  [41,42]. Excited configuration  $(t_1)^5(e)^1$  results four electronic states: two singlets and two triplets:  ${}^1T_2 < {}^1T_1 < {}^3T_2 \cong {}^3T_1$  [43]. It is accepted that blue luminescence originates from the  ${}^3T_2 \cong {}^3T_1 \rightarrow {}^1A_1$  [44]. Because of the symmetry lowering from  $T_d$  to  $C_{3v}$  due to the JT effect, the  ${}^3T_1$  state splits into the  ${}^3A_2$  and  ${}^3E$  sublevels, and the  ${}^3T_2$  state into the  ${}^3A_1$  and  ${}^3E$  sublevels [45]. The schematic diagram is shown in Figure 5.5.

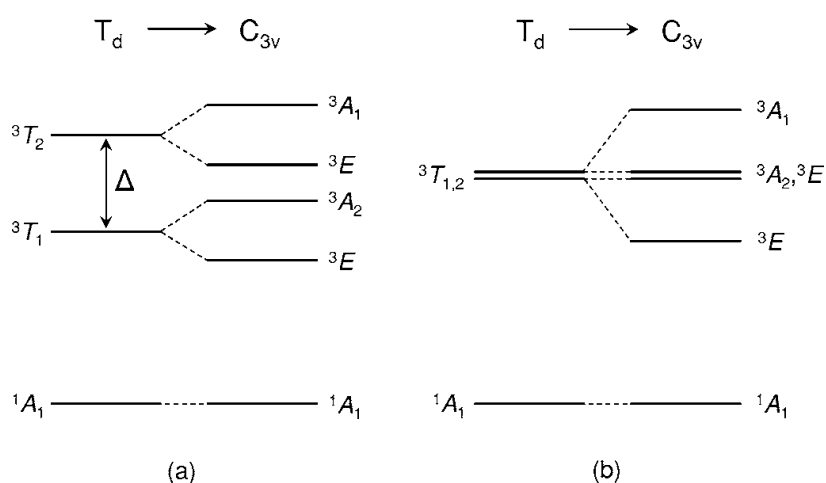


**Figure 5.5** Splitting of Triplet states due to Jahn-Teller effect [45]

Here we proposed that the Gaussian peak I (367 nm), the Gaussian peak II (392 nm) and the Gaussian peak III (452 nm) may correspond to the radiative transitions from  ${}^3A_1 \rightarrow {}^1A_1$ ,  ${}^3A_2 \cong {}^3E \rightarrow {}^1A_1$  and  ${}^3A_2 \rightarrow {}^1A_1$ , respectively. Hence blue emission occurs from the lower lying triplet state split by Jahn-Teller interaction.

The peak position of all the three blue Gaussian components in PL spectra recorded at room temperature is shifted towards the short wavelength side compared to those reported at lower temperatures. This type of blue shift is also reported by M.Itoh which can be explained well by configurational coordinate diagram. Similar blue shift has also been observed in  $\text{CdWO}_4$  [46] and  $\text{CaWO}_4$  [47]. The G(II) band which is dominant at lower temperatures also do major contribution at room temperature.

The Gaussian peak IV (around 510 nm) corresponds to green emission which is assumed to arise from oxygen deficient regular  $\text{WO}_3$  group also called F center. Oxygen vacancies  $V_O$  (or  $F^{++}$ ) can capture one or two electrons from  $[\text{WO}_4^{2-}]$  to form  $F^+$  or F centers and so  $[\text{WO}_4^{2-}]$  is changed into  $\text{WO}_3$ . This crystal defect (lack of oxygen) is related to surface in scheelite phase. This emission as a result of the photo-thermally stimulated disintegration of localized exciton states and subsequent recombination of the produced electron and hole centres near  $\text{WO}_3$  groups. As our sample also contains raspite phase, this emission also ascribed to intrinsic luminescence probably originates from localized exciton in octahedral  $\text{WO}_6^{6-}$  groups in the raspite phase. Raspite-type inclusions which exist in our samples usually crystallize in a scheelite-type structure. The transformation from raspite to scheelite is expected to take place by thermal stress because of the very small volume difference between the two forms. These inclusions probably result from the thermal stress that is unavoidably introduced in  $\text{PbWO}_4$  crystals.

The intensity of four individual Gaussian peaks of Cerium doped  $\text{PbWO}_4$  microcrystallites reduce to different extents compared with that of pure  $\text{PbWO}_4$  samples. According to Kobayashi et al. Cerium doping in  $\text{PbWO}_4$  results low energy shift of absorption spectra due to  $4f \rightarrow 5d$  transitions and hence emission spectra should also shift to lower energy side due to Stokes shift. Similar type of red shift is observed in position of Gaussian peak IV in our case. Furthermore, decrease of light yield (LY) for PWO:Ce sample by a factor 2–3 was observed with respect to undoped PWO. The absence of intrinsic  $\text{Ce}^{3+}$  emission at the room temperature and observed lower Light Yield can be explained by a non-radiative  $5d \rightarrow 4f$  transition to the ground state of excited  $\text{Ce}^{3+}$  ions, i.e.  $\text{Ce}^{3+}$  ions can serve as efficient non-radiative traps in the PWO matrix. Such a conclusion support the observed faster PL decay of PWO: Ce at room temperature (RT) with respect to the undoped sample, which can be explained by selective suppression of the delayed recombination process due to non-radiative recombination of free electrons and holes at the  $\text{Ce}^{3+}$  sites.

PL spectra of all the  $\text{PbWO}_4$  microcrystallites prepared with different lead sources having different morphologies shows very weak size-dependency indicate that the sizes of these structures are so big that they are beyond the border of the quantum confinement regime.

## 5.9 Effect of Synthesis Parameters on Photoluminescence

As discussed in the previous chapters regarding structural studies, different reaction parameters produced different types of crystal structures and morphologies as shown in below Table 5.3.

**Table 5.3** Summary of reaction conditions, phase, morphologies and particle size of undoped and Cerium doped  $\text{PbWO}_4$  prepared using different Lead chloride.

Sample	$\text{PbCl}_2$ conc. (M)	$\text{Na}_2\text{WO}_4$ conc. (M)	Ce conc. (M)	Temp. (°C)	Time (h)	pH	Morphology	Average particle size (nm)
5	0.01	0.01	-	100	4	7	micro plates	few $\mu\text{m}$
							micro particles	100nm
6	0.01	0.01	0.001	100	4	7	tetrahedron	100nm
8	0.01	0.01	-	125	4	7	spherical nanoparticles	20-40 nm
							Hollow nano tubes	12.37 nm (OD) 80-170 nm (L)
9	0.01	0.01	-	125	4	11	nanorods	40nm (OD) 2 $\mu\text{m}$ (L)
13	0.1	0.1	0.001	200	12	7	spherical nanoparticles	50-100 nm

## 5.10 Excitation Spectra

Figure 5.6 represent the excitation spectra of undoped  $\text{PbWO}_4$ . This excitation spectra was collected for a Sample No 8. The excitation spectrum for 400 nm emission has a wide broad band peaking at 250 nm , and a weaker band at 296 nm and a second weaker new band is observed at 615 nm. Excitation spectra of remaining samples also shows similar behavior which are not shown.

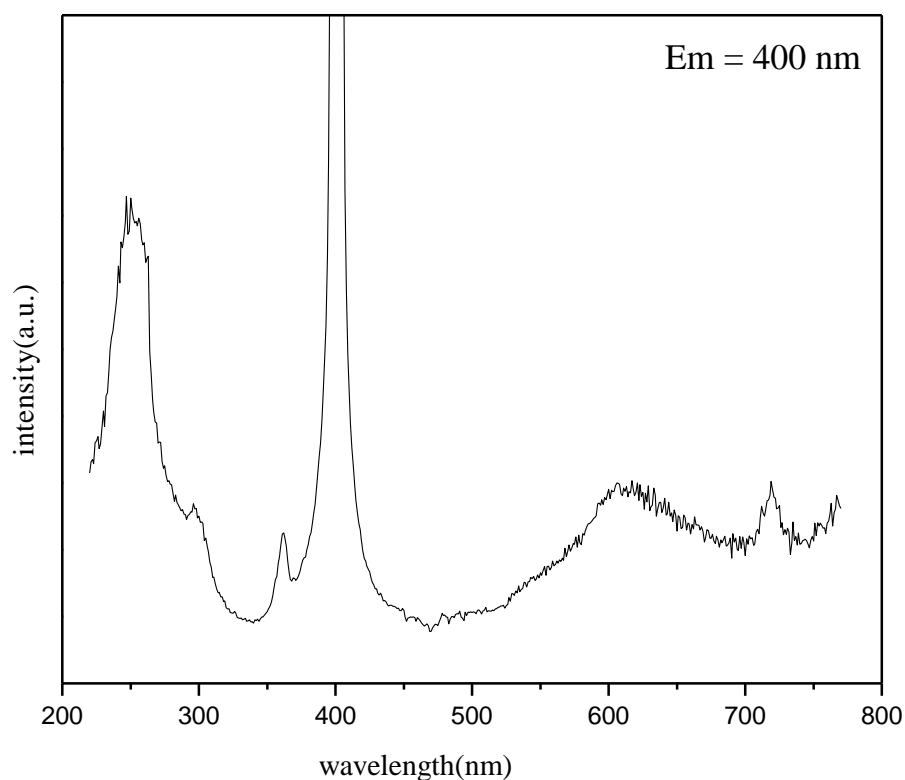


**Figure 5.6** Excitation spectra of  $\text{PbWO}_4$  (sample 8)

## 5.11 Emission Spectra

Figure 5.7 shows combined emission spectra of undoped and cerium doped  $\text{PbWO}_4$  phosphors. This spectra reveals that different reaction parameters have great influence on the photoluminescence which is discussed upcoming sections. Below Table shows summary of the different reaction conditions kept during experiment.

**$\text{PbWO}_4$  prepared at different reaction conditions**

Sample No.	$\text{PbCl}_2$ conc. (M)	$\text{Na}_2\text{WO}_4$ conc. (M)	Ce conc. (M)	Temp. ( $^\circ\text{C}$ )	Time (h)	pH
5	0.01	0.01	-	100	10	7
6	0.01	0.01	0.001	100	10	7
7	0.01	0.01	-	125	10	3
8	0.01	0.01	-	125	10	7
9	0.01	0.01	-	125	10	11
10	0.01	0.01	-	150	10	7
11	0.01	0.01	0.001	150	10	7
12	0.01	0.01	-	200	10	7
13	0.01	0.01	0.001	200	10	7
14	0.01	0.01	0.001	R.T.	10	7

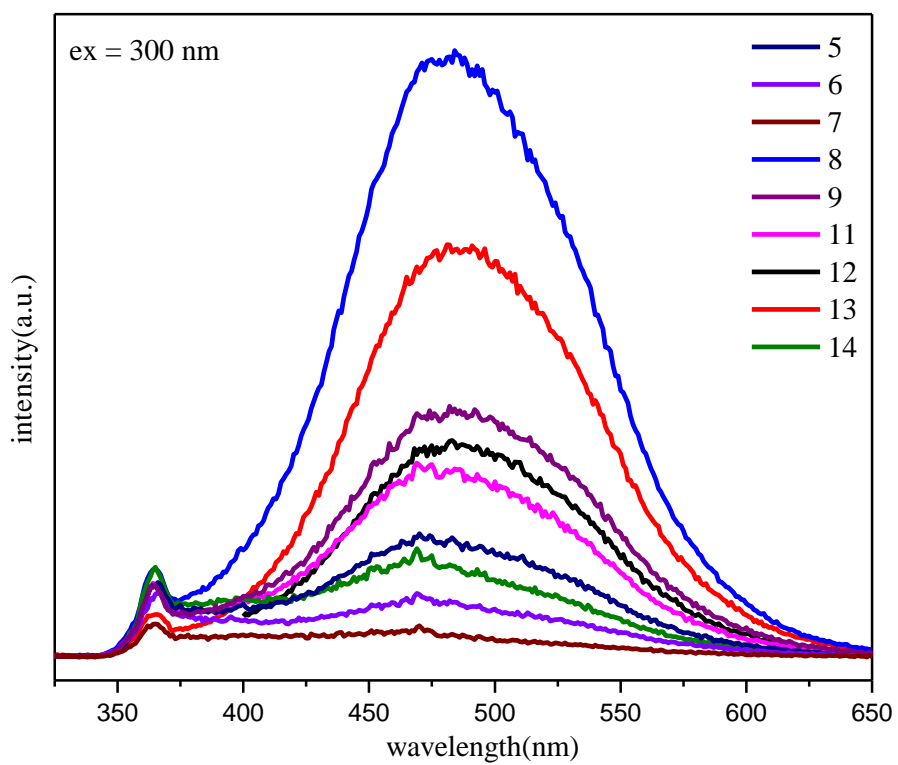


**Figure 5.7** Effect of Synthesis parameters on PhotoLuminescence intensity

## 5.12 PL spectra of undoped and Cerium doped $\text{PbWO}_4$ synthesized at $200^\circ\text{C}$

Figure 5.8 shows room temperature photoluminescence spectra of undoped and Cerium doped  $\text{PbWO}_4$  nanophosphor synthesized  $200^\circ\text{C}$  at excited with 254 nm wavelength. As expected both the samples show broad “spread-eagle-shaped” blue-green with integral luminescence intensity of emission falls in 350-600 visible region.

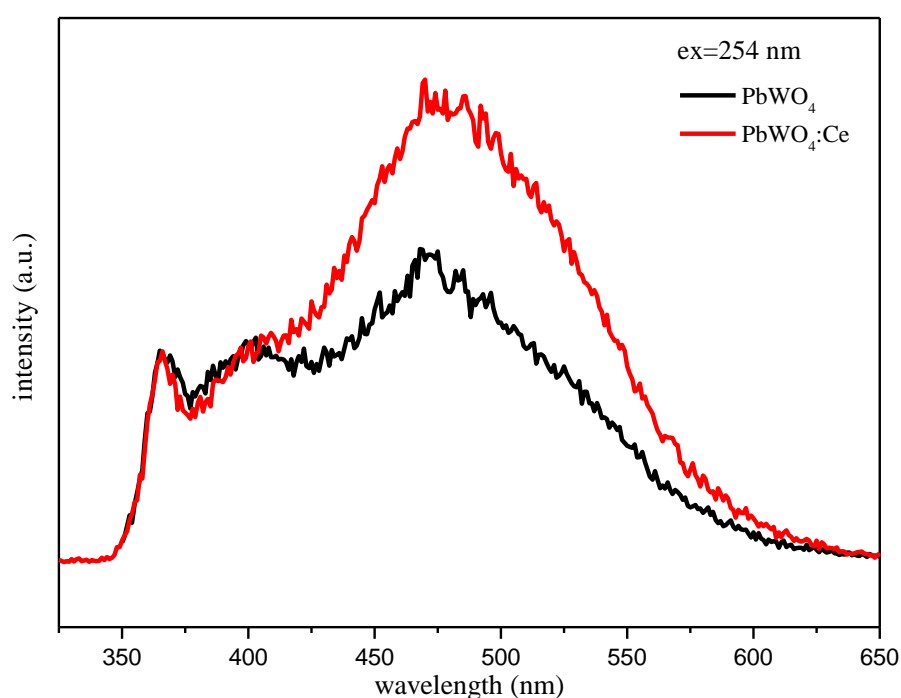


**Figure 5.8** PL spectra of  $\text{PbWO}_4$  synthesized at  $200^\circ\text{C}$

The decomposition of PL spectra into individual Gaussian components results four Gaussians to achieve a good agreement with the experimental data shown in Figure 5.8 (a) and (b). In order to do detailed analysis of luminescence spectra it is fitted with four individual Gaussian components and named Gaussian peak I, II, III and IV respectively. Variation in locations and intensity of strongly overlapped Gaussian components of photoluminescence spectra of  $\text{PbWO}_4$  and  $\text{PbWO}_4:\text{Ce}$  prepared at  $200^\circ\text{C}$  is shown in Table 5.4 and discussed here.

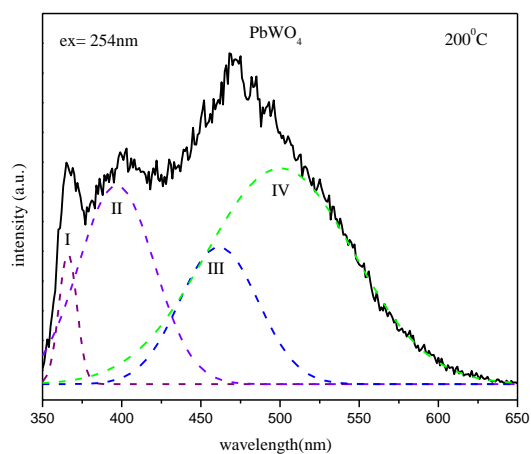


Figure 5.8 (a)

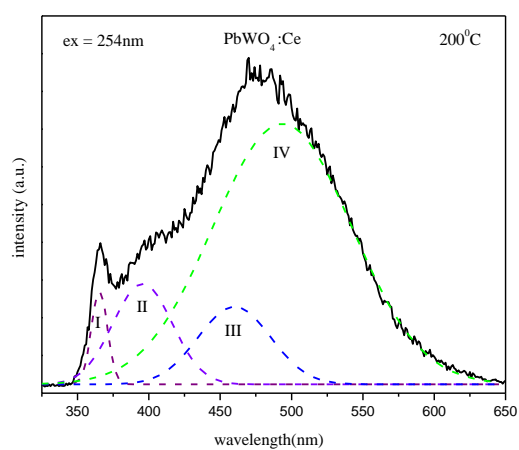


Figure 5.8 (b)

**Table 5.4** The locations and intensity of Gaussian components of PL spectra of  $\text{PbWO}_4$  and  $\text{PbWO}_4:\text{Ce}$  prepared at  $200^\circ\text{C}$ .

Temp. ( $^\circ\text{C}$ )	Gaussian peak I		Gaussian peak II		Gaussian peak III		Gaussian peak IV	
	wavelength (nm)	intensity (a.u.)	wavelength (nm)	intensity (a.u.)	wavelength (nm)	intensity (a.u.)	wavelength (nm)	intensity (a.u.)
PWO	366	25	397	36	461	26	500	39
PWO:Ce	366	27	397	29	461	23	494	71

As already mentioned earlier the Gaussian peak I is observed at 366 nm, the Gaussian peak II at 397 nm and the Gaussian peak III at 461 nm may correspond to the radiative transitions from  ${}^3A_1 \rightarrow {}^1A_1$ ,  ${}^3A_2 \cong {}^3E \rightarrow {}^1A_1$  and  ${}^3A_2 \rightarrow {}^1A_1$ , respectively from the lower lying triplet state split by Jahn-Teller interaction in the regular  $WO_4^{2-}$  complex.

As shown in Figure 5.8(a) intensity of blue component B(II) is comparable to green component G(IV) in undoped  $PbWO_4$ . When  $PbWO_4$  is doped with cerium intensity of blue components is suppressed and green luminescence is remarkably increases as shown in Table 5.4. The contribution of green emission Gaussian component G(IV) in Cerium doped  $PbWO_4$  increase from 50% to 75% of the total light yield. Annealing at a temperature below  $700^\circ C$  suppressed the blue luminescence and enhanced its green components [48]. As both the samples prepared at  $200^\circ C$  contains only stolzite phase, possibility of enhancement of G(IV) component due to presence of raspite inclusions is ruled out. The only possible reason due to which green luminescence is increase is the higher synthesis temperature. In hydrothermal synthesis crystal growth occurs in close vessel called autoclave in the absence of sufficient air atmosphere. TEM images of Ce doped  $PbWO_4$  synthesized at  $200^\circ C$  temperatures shows that they are spherical nanoparticles having size about 50-100 nm. At  $200^\circ C$  temperature during crystal growth of  $PbWO_4:Ce$  oxygen near the surface of spherical nanoparticles get sufficient energy to escape from regular lattice site and creates ( $V_o$ ) oxygen vacancies. At such high temperature oxygen escape from regular  $WO_4^{2-}$  complex and convert it to oxygen deficient  $WO_3$  complex. Higher concentration of oxygen deficient  $WO_3$  complex increase green luminescence. Thus decrease in concentration of  $WO_4^{2-}$  centers responsible for blue emission and increase in concentration of  $WO_3$  centers responsible for green emission increases the contribution of green emission from 50% to 75%.

However, as reported previously, the green emission of  $PbWO_4$  crystals is slower than the blue one in the decay characteristics [49]. Higher synthesise temperature can

enhance the green luminescence and give some contributions to the “slow” decay components which may be negative to the scintillating properties of PWO. Hence we conclude that Cerium doped  $\text{PbWO}_4$  prepared at  $200^\circ\text{C}$  is not preferable to use for scintillation detector purpose.

### 5.13 Effect of pH on Photoluminescence of $\text{PbWO}_4$ nanophosphor

Structural (XRD and TEM) studies of undoped as well as Cerium doped  $\text{PbWO}_4$  phosphor synthesized at different pH shows that the pH of the reaction solution plays an important role and it varies the crystallinity and morphology of the product considerably. In order to study the effect of pH of the reaction solution on luminescence property of  $\text{PbWO}_4$  synthesized at different (3,7 and 11) pH, photoluminescence spectra of undoped  $\text{PbWO}_4$  synthesized at different pH was recorded at two excitation wavelength 300 nm and 254 nm and are shown in Figure 5.9 and Figure 5.10, respectively.

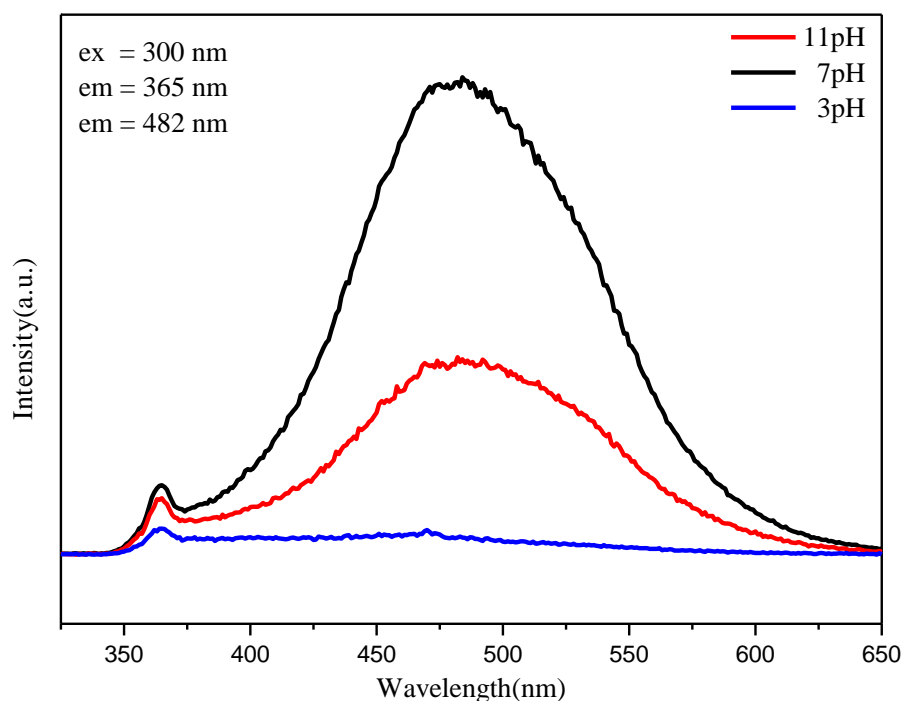


**Figure 5.9** PL emission of  $\text{PbWO}_4$  synthesized at different pH excited with 300nm

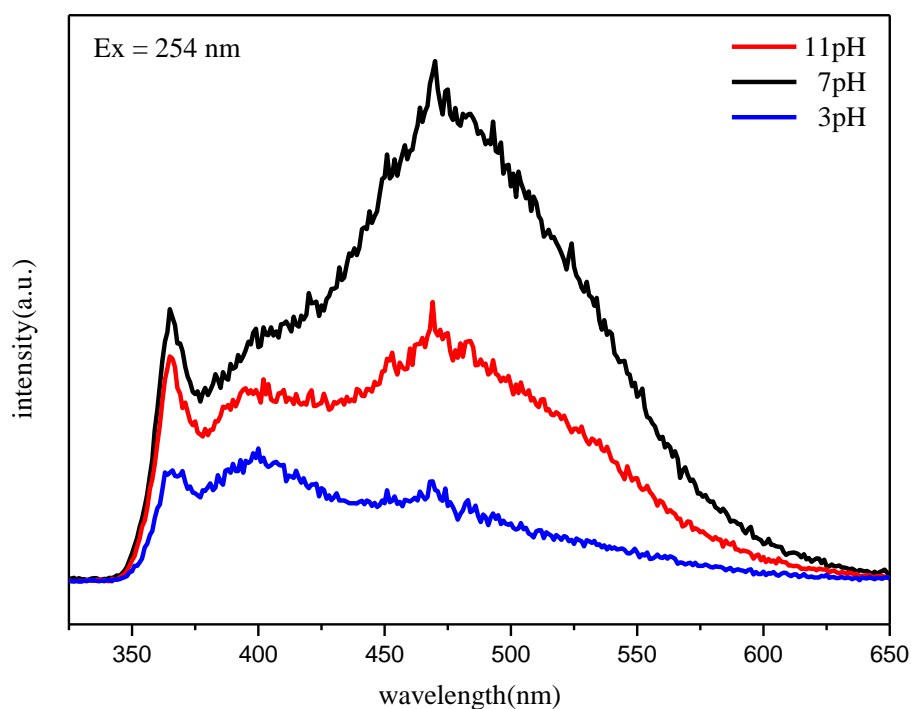


**Figure 5.10** PL emission of PbWO<sub>4</sub> synthesized at different pH excited with 254 nm

Figure 5.10 shows room temperature photoluminescence spectra of nanocrystalline PbWO<sub>4</sub> powders prepared at three different (3, 7 and 11) pH of reaction solution excited with 254 nm wavelength. PbWO<sub>4</sub> shows “spread-eagle-shaped” broad luminescent emissions in blue and green range. As we can see from the PL spectra within the range of pH 3-11, the position of the emission peaks of the product remained almost unchanged for all the samples. In order to further obtain the detailed parameters about the luminescence properties of PbWO<sub>4</sub> microcrystals, we had fitted the emission spectra using four individual Gaussian lines to achieve good agreement with the experimental data which are shown below in Figure 5.10 (a-c). Variation in the location of Gausssian peaks and in their intensity is shown in Table 5.5.

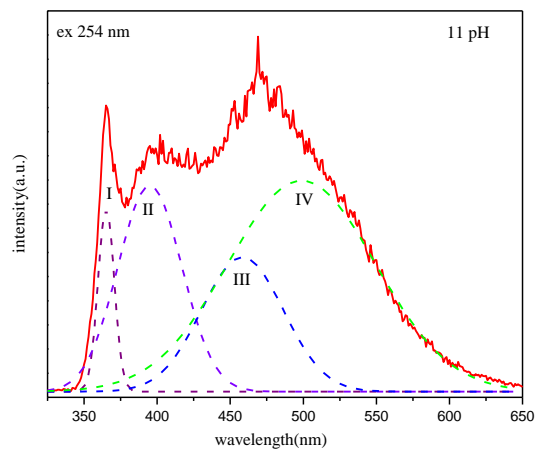


Figure 5.10(a)

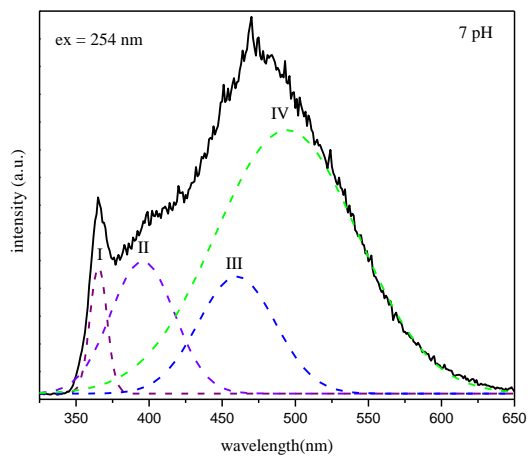


Figure 5.10(b)

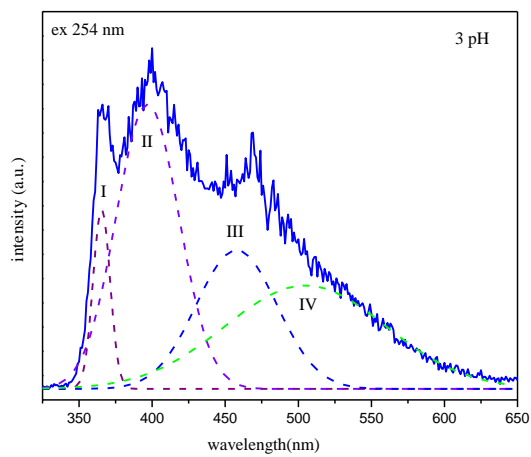


Figure 5.10(c)

**Table 5.5** The locations and intensity of Gaussian components of PL spectra of PbWO<sub>4</sub> samples prepared at different pH

pH	Gaussian peak I		Gaussian peak II		Gaussian peak III		Gaussian peak IV	
	wavelength (nm)	intensity (a.u.)	wavelength (nm)	intensity (a.u.)	wavelength (nm)	intensity (a.u.)	wavelength (nm)	intensity (a.u.)
3	365	20	397	30	458	15	505	12
7	365	48	396	50	460	44	494	97
11	365	39	395	44	458	29	499	45

Obtained PL spectra was fitted with four individual Gaussian peaks having peaks position for peak I (365 nm), peak II (395 nm), peak III(459 nm) and peak IV (500nm) . Here we proposed that the Gaussian peak I, the Gaussian peak II and the Gaussian peak III may correspond to the radiative transitions from  $^3A_1 \rightarrow ^1A_1$ ,  $^3A_2 \cong ^3E \rightarrow ^1A_1$  and  $^3A_2 \rightarrow ^1A_1$ , respectively. Hence blue emission occurs from the lower lying triplet state split by Jahn-Teller interaction. The Gaussian peak IV ascribed to oxygen deficient irregular WO<sub>3</sub> neutral molecule.

According to XRD data, sample prepared with 7pH has highest crystallinity and sample prepared with 3pH has lowest crystallinity. Further increase in pH of the solution (7 to 11) crystallinity again reduced. It indicates that PL spectra of nano-sized PbWO<sub>4</sub> crystallites are strongly relied on their particle size and crystallinity. PL intensity has direct relation with crystallinity. The better crystallinity, the higher PL emission peak is.

PbWO<sub>4</sub> (Nanoparticles and HNTs) obtained at 7pH, display a strong emission peak cantered at about 485 nm at room temperature. However, the absolute luminescence intensity increased with increasing pH, over the range of 3-7 pH, implying that the Nanoparticles and HNTs had much improved luminescence intensity. The very weak PL intensity of the sample obtained for pH 3 due to poor crystallinity.

The PL intensity of blue emission peak is highest for sample prepared at 7pH (HNTs), it is intermediate for sample prepared at 11pH (Nanorods) and lowest for sample prepared at 3pH which indicates that  $\text{PbWO}_4$  HNTs have more regular lattice structure and uniform morphology compared to Nanorods. Sample prepared at 3pH has lowest regular lattice structure.

Similarly, The PL intensity of green emission peak is highest for sample prepared at 7pH (HNTs) intermediate for sample prepared at 11pH (Nanorods) and lowest for sample prepared at 3pH which indicates that  $\text{PbWO}_4$  HNTs have highest defect centres relative to oxygen due to faster 1-D crystal growth compared to Nanorods and sample prepared at 3pH has lowest defect centres relative to oxygen.

Very high size-dependent emission of photoluminescence observed among these three products with different morphologies indicates that the sizes of these structures are so in the quantum confinement regime.

### 5.14 Effect of Synthesis Temperature on Photoluminescence of $\text{PbWO}_4$

Room Temperature Photoluminescence spectra of undoped  $\text{PbWO}_4$  prepared at different temperatures is investigated and it is shown in Figure 5.11 for the 300nm excitation wavelength. The light-emitting property of the lead tungstate crystal is greatly influenced by synthesis temperature. PL spectra of all the samples exhibit emission in blue-green region with same emission peak position at 482 nm.

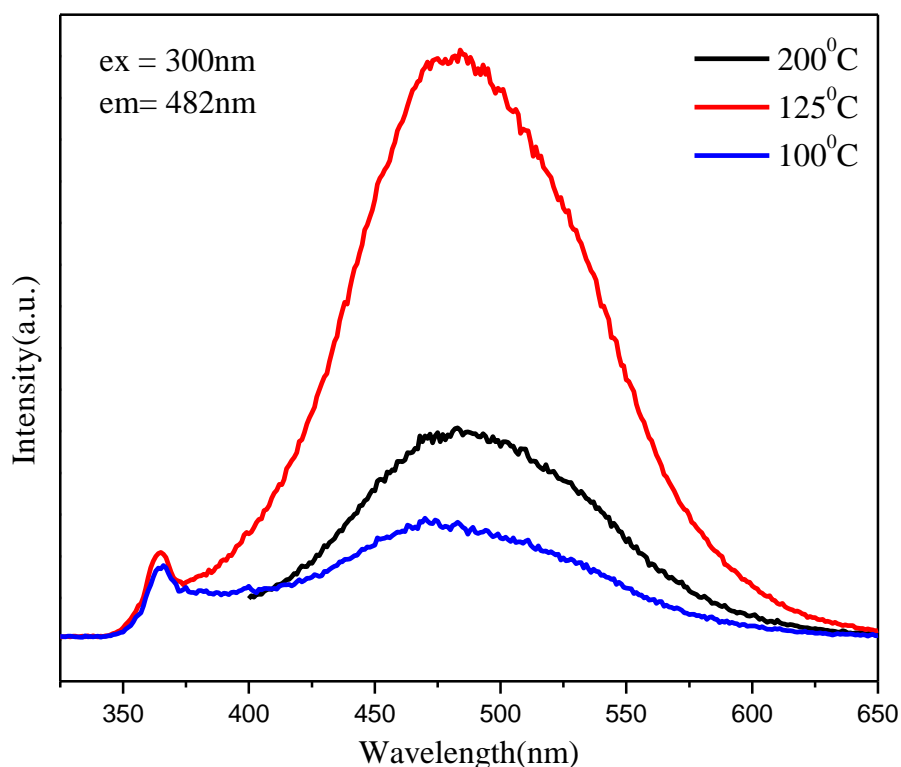


**Figure 5.11** PL spectra of  $\text{PbWO}_4$  synthesized at different temperatures

As we can see from the PL spectra, PL intensity is least for the sample prepared at 100 °C which increases for the sample prepared at 125 °C. PL intensity is again decrease for the sample prepared at 200°C. Apparently, raising the reaction temperature of the hydrothermal process would increase the luminescent intensity up to certain limits and further rise of

temperature lower the PL intensity. From this result, we can conclude that 125°C is the optimum temperature for the good intensity.

According to structural studies of these samples, PbWO<sub>4</sub> obtained at 100 °C are mixture of microparticles (100nm) with stolzite phase and micro plates (few μm) with raspite inclusions which have low crystallinity. Spherical nanoparticles (20-40 nm) and Hollow Nano Tubes (80-170 nm) of PbWO<sub>4</sub> having pure stolzite phase are obtained at 125 °C and they have highest crystallinity. XRD study of PbWO<sub>4</sub> sample prepared at 200°C shows that it has intermediate crystallinity between 125°C and 100°C.

It is well known that PL intensity has direct relation with crystallinity. The better crystallinity, the higher PL emission peak is. Morphologies and sizes also influence the luminescence properties of inorganic materials. Hence among all three samples (HNTs) of PbWO<sub>4</sub> prepared at 125 °C shows strong green luminescence due to its highest crystallinity while (microparticle + microplates ) of PbWO<sub>4</sub> prepared at 100 °C shows weak luminescence due to poor crystallinity.

As already discussed higher crystallinity of Quasi-spherical nanoparticles and Hollow Nano Tubes are main reason to produce high PL intensity compared to low crystalline microparticles and flake like inclusions. It implied that PbWO<sub>4</sub> nanostructure have a better luminescence intensity then microstructure at room temperature.

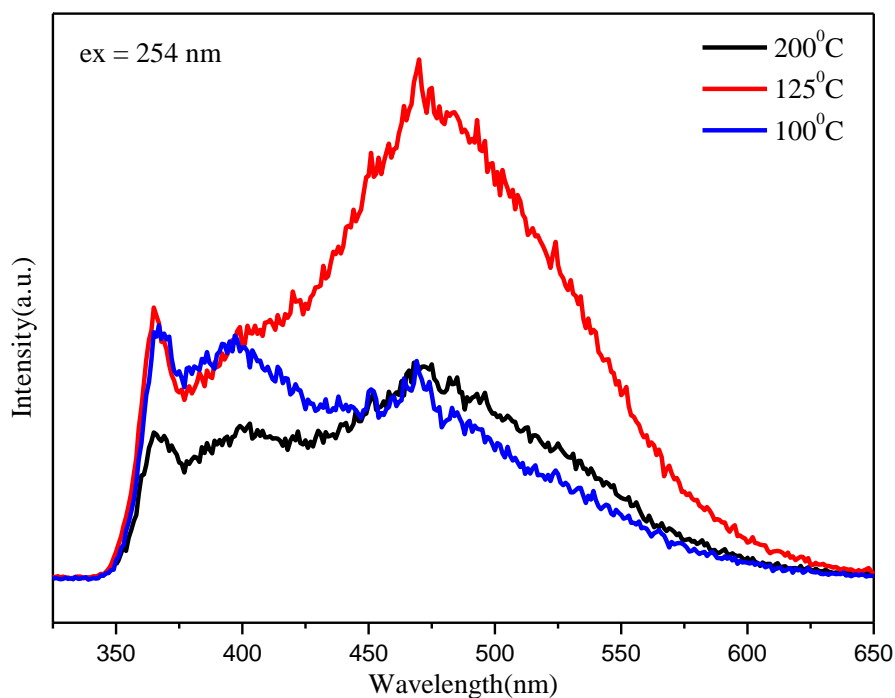


**Figure 5.12** PL spectra of PbWO<sub>4</sub> prepared at different temperatures excited with 254nm

Figure 5.12 shows Room temperature photoluminescence spectra of PbWO<sub>4</sub> phosphor prepared at different temperatures excited with 254 nm wavelength. PbWO<sub>4</sub> shows broad luminescent emissions in blue and green range. In order to further obtain the detailed parameters about the luminescence properties of PbWO<sub>4</sub>, we had decomposed the emission spectra using four individual Gaussian components to achieve good agreement with the experimental data which are shown in Figure 5.12 (a-c). Variation in the location of Gaussian peaks and in their intensity is shown in Table 5.6.

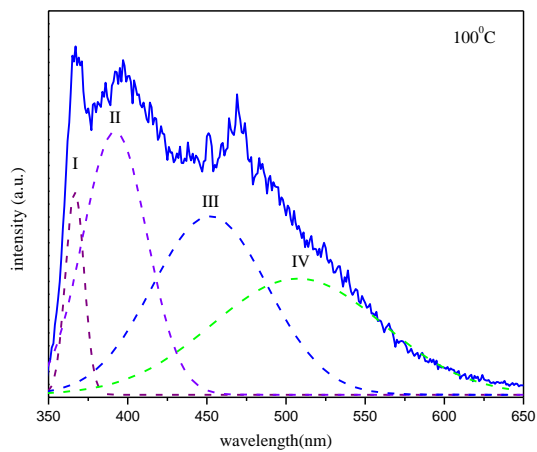


Figure 5.12(a)

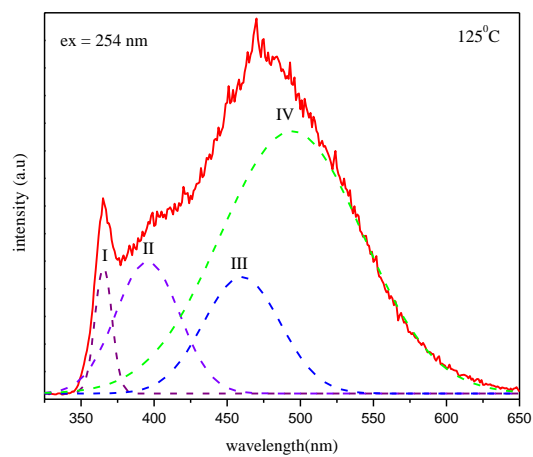


Figure 5.12(b)

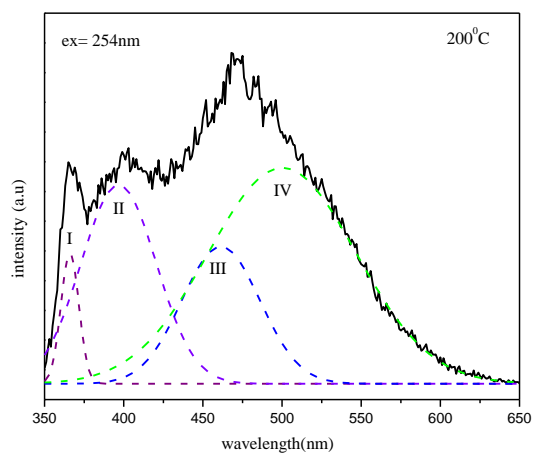


Figure 5.12(c)

**Table 5.6** The locations and Intensity of Gaussian components of PL spectra of PbWO<sub>4</sub> samples prepared at different temperatures.

Temp. (°C)	Gaussian peak I		Gaussian peak II		Gaussian peak III		Gaussian peak IV	
	wavelength (nm)	intensity (a.u.)	wavelength (nm)	intensity (a.u.)	wavelength (nm)	intensity (a.u.)	wavelength (nm)	intensity (a.u.)
100	367	40	392	52	452	35	507	23
125	365	48	396	50	460	44	494	97
200	366	25	397	36	461	26	500	39

As we can see from the Table 5.6 positions of B(I) remain almost constant with temperature. The position of B(II) and B(III) components shift to lower energy side and the position of G(IV) component shift towards higher energy side first and then towards lower energy side. As already mentioned earlier the Gaussian peak I is observed around 365 nm, the Gaussian peak II at 396 nm and the Gaussian peak III at 460 nm may correspond to the radiative transitions from  $^3A_1 \rightarrow ^1A_1$ ,  $^3A_2 \cong ^3E \rightarrow ^1A_1$  and  $^3A_2 \rightarrow ^1A_1$ , respectively from the lower lying triplet state split by Jahn-Teller interaction in the regular  $WO_4^{2-}$  complex. The Gaussian peak IV corresponds to oxygen deficient  $WO_3$  irregular complex in scheelite phase.

PbWO<sub>4</sub> microcrystallites prepared at 100°C contains mixed phase and microcrystals and microplates like morphologies. PbWO<sub>4</sub> prepared at 125°C has hollow nano tubes with pure stolzite phase structure while that prepared at 200°C has unknown morphology and pure stolzite phase confirmed from xrd spectra. Luminescence spectra of individual case are already discussed. Intensity of blue components B(I), B(II) and B(III) is higher at low temperatures and low at higher temperature. As we know that regular lattice group  $WO_4^{2-}$  is responsible for blue emission, higher intensity of blue emission at low temperature shows that samples prepared at low temperature has higher concentration of  $WO_4^{2-}$ . At higher reaction temperature lattice regularity breaks and also decrease the

concentration of blue emission center. Enhancement of Green emission of the sample prepared at 125°C is due to presence of larger amount of surface defect is also discussed.

### 5.15 Effect of Synthesis Temperature on Photoluminescence of $\text{PbWO}_4:\text{Ce}$

Similar to PL study of undoped  $\text{PbWO}_4$  prepared at different temperatures, PL spectra of Cerium doped  $\text{PbWO}_4$  prepared at different temperatures also investigated and it is shown in Figure 5.13 and Figure 5.14.

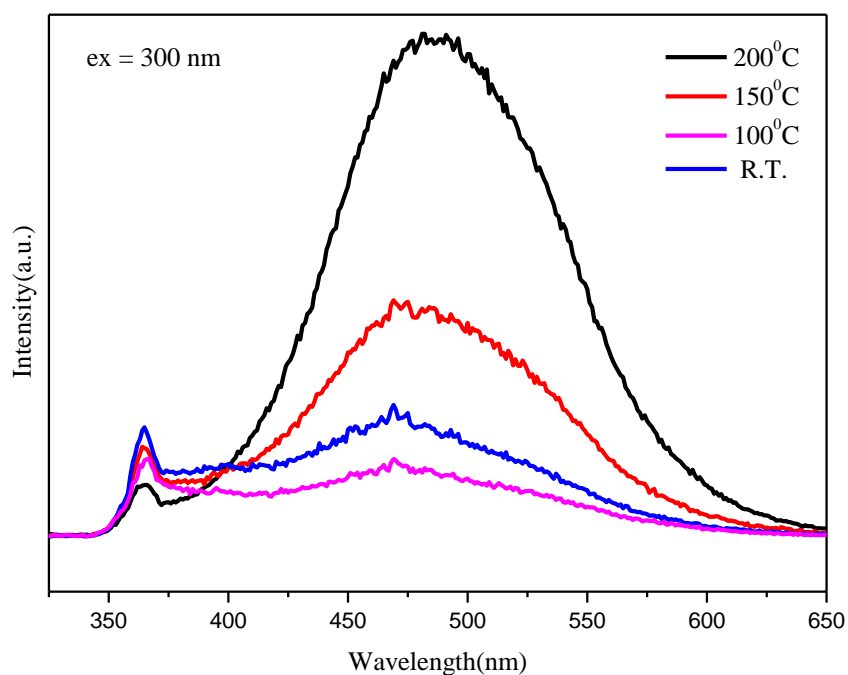


**Figure 5.13** PL spectra of  $\text{PbWO}_4:\text{Ce}$  prepared at different temperatures excited with 300nm. The light-emitting property of the Cerium doped lead tungstate crystal is greatly influenced by synthesis temperature. PL spectra of all the samples exhibit emission in blue-green region. Peak position of PL emission at room temperature is similar to that of undoped samples i.e. 482 nm but peak position is shifted to higher energy side for the samples prepared at higher temperatures i.e. 470 nm.

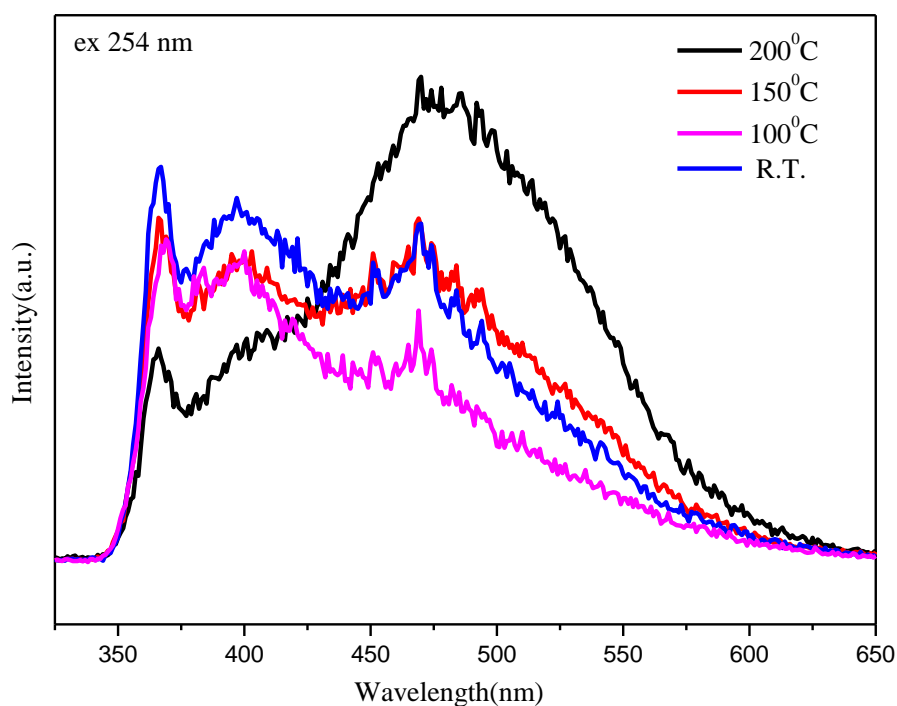


**Figure 5.14** PL spectra of PbWO<sub>4</sub>: Ce prepared at different temperatures excited with 254nm

Figure 5.14 shows room temperature photoluminescence spectra of nanocrystalline PbWO<sub>4</sub>: Ce powders prepared at different temperatures excited with 254 nm wavelength. PbWO<sub>4</sub> shows broad luminescent emissions in blue and green range. In order to further obtain the detailed parameters about the luminescence properties of PbWO<sub>4</sub> microcrystals, we had fitted the emission spectra using four individual Gaussian lines to achieve good agreement with the experimental data which are shown below Figures 5.14 (a-d). Variation in the location of Gaussian peaks and in their intensity is shown in Table 5.7.

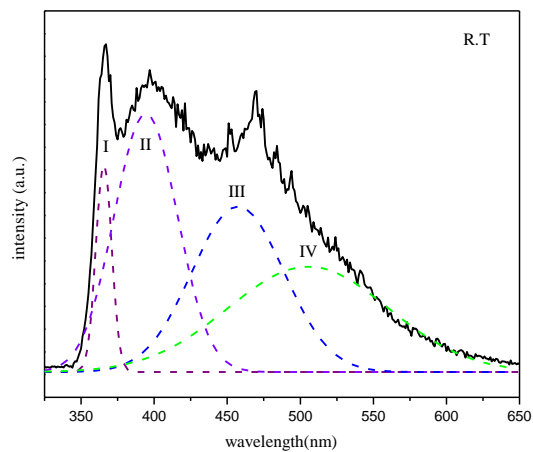


Figure 5.14(a)

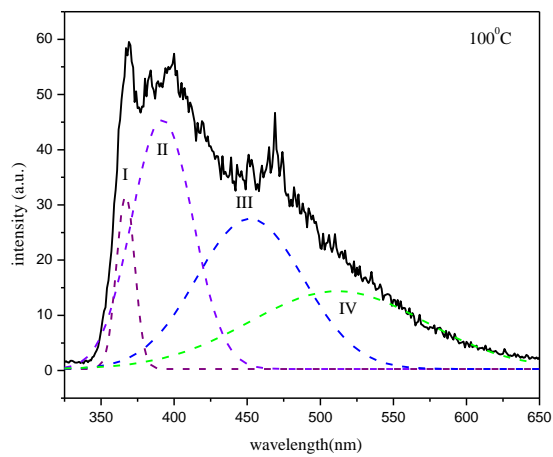


Figure 5.14(b)

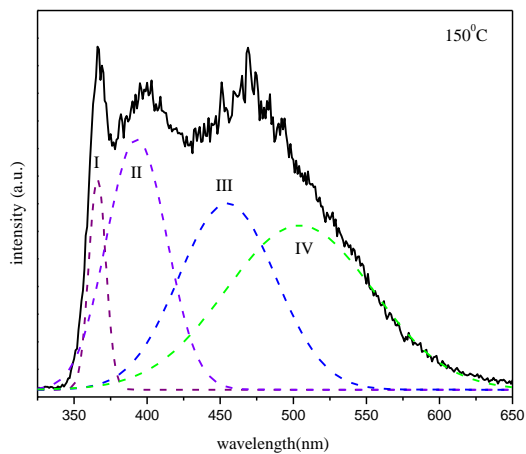


Figure 5.14(c)

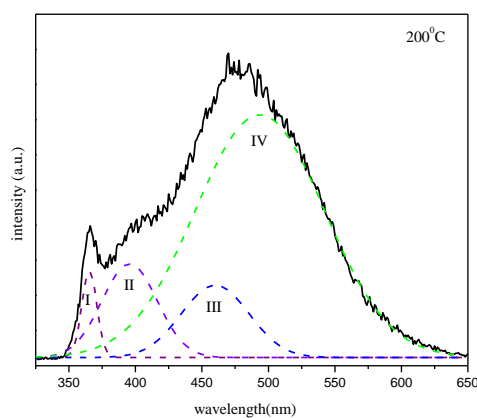


Figure 5.14(d)

**Table 5.7** The locations and intensity of Gaussian components of PL spectra of  $\text{PbWO}_4 : \text{Ce}$  samples prepared at different temperatures.

Temp. (°C)	Gaussian peak I		Gaussian peak II		Gaussian peak III		Gaussian peak IV	
	Wavelength (nm)	Intensity (a.u.)	Wavelength (nm)	Intensity (a.u.)	Wavelength (nm)	Intensity (a.u.)	Wavelength (nm)	Intensity (a.u.)
R.T	366	46	394	57	457	37	505	24
100	367	32	392	45	452	27	512	14
150	366	40	393	47	455	35	504	31
200	365	27	396	29	460	23	494	71

As already mentioned earlier the Gaussian peak I is observed at 366 nm, the Gaussian peak II at 397 nm and the Gaussian peak III at 461 nm may correspond to the radiative transitions from  $^3A_1 \rightarrow ^1A_1$ ,  $^3A_2 \cong ^3E \rightarrow ^1A_1$  and  $^3A_2 \rightarrow ^1A_1$ , respectively from the lower lying triplet state split by Jahn-Teller interaction in the regular  $\text{WO}_4^{2-}$  complex. The Gaussian peak IV corresponds to oxygen deficient  $\text{WO}_3$  irregular complex in scheelite phase.

As we can see from the Table 5.7 positions of B(I) remain almost constant with temperature. The position of B(II) and B(III) components shift to lower energy side and the position of G(IV) component shift towards higher energy side. Intensity of blue components B(I), B(II) and B(III) is higher at low temperatures and low at higher temperature. The

reason for enhancement of green emission for  $\text{PbWO}_4$  sample prepared at  $200^\circ\text{C}$  is already discussed in the respective section.

## 5.16 Up Conversion emission (anti-Stokes emission) in $\text{PbWO}_4$

Phosphors that are capable of absorbing photons of a certain energy  $E_1$  and emitting photons with another energy  $E_2$ , such that  $E_2 > E_1$ . Thus it is also possible to obtain luminescence at photon energies higher than the absorbed photon energy. This is called *anti-Stokes or up-conversion luminescence* and it occurs for multilevel systems. As  $\text{PbWO}_4$  contains various types of luminescent centers at different energy levels, it is possible to obtain up-conversion luminescence in our system.

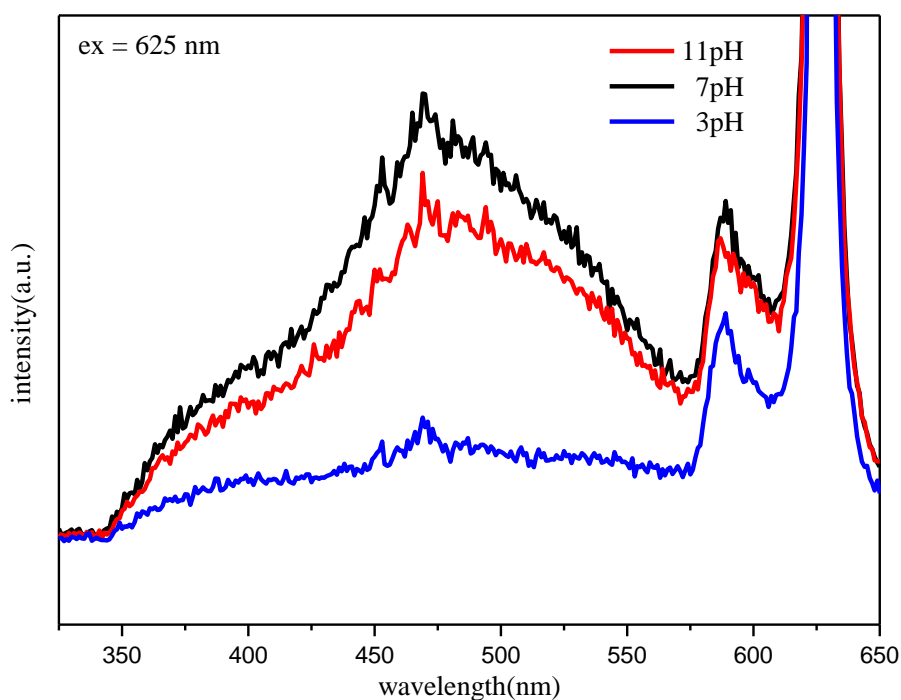


**Figure 5.15** Up-conversion luminescence in  $\text{PbWO}_4$  synthesized at different pH

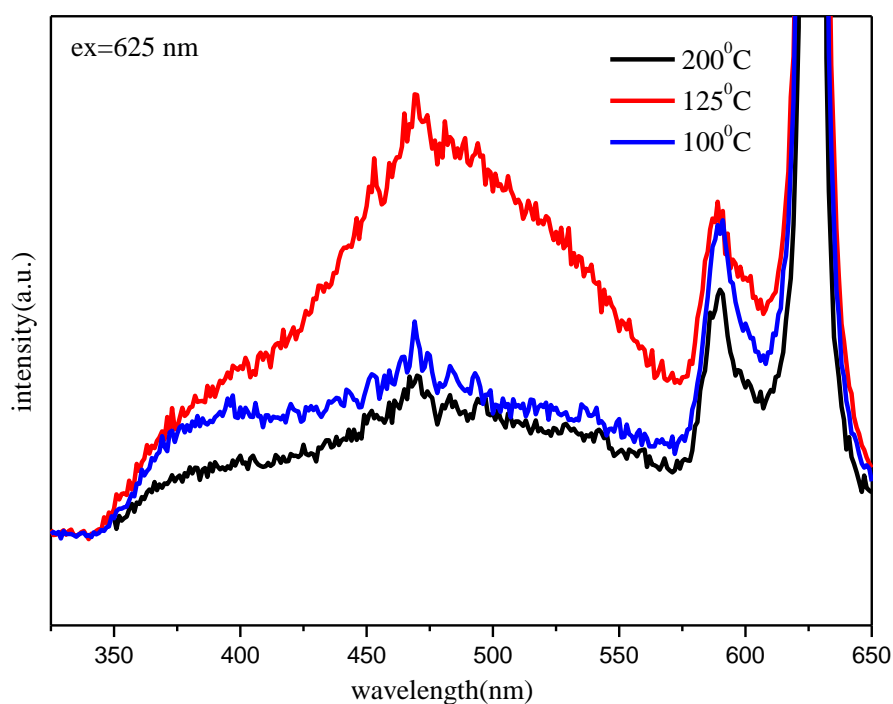


**Figure 5.16** Up-conversion luminescence in  $\text{PbWO}_4$  synthesized at different temperature

Figure 5.15 and Figure 5.16 shows the up-conversion emission of undoped  $\text{PbWO}_4$  synthesized with different pH and temperatures excited with 625 nm wavelength, respectively. In both cases, the same profile of complex emission was observed; and broad blue-green up-conversion emission bands were in the 450–550 nm region ( ${}^3\text{A}_1 \rightarrow {}^1\text{A}_1$ ,  ${}^3\text{A}_2 \cong {}^3\text{E} \rightarrow {}^1\text{A}_1$ ,  ${}^3\text{A}_2 \rightarrow {}^1\text{A}_1$  and oxygen deficient  $\text{WO}_3$  complex) and in the 600 nm region (corresponding to the color center). As shown in both Figures, the intensity of up-conversion luminescence is highest for  $\text{PbWO}_4$  sample prepared at 7pH or 125°C, intermediate for 11pH and lowest for 3pH. Up-conversion luminescence intensity is also least for sample prepared at 100°C and 200°C.

### 5.16.1 Red emission center

There is another luminescent centre in  $\text{PbWO}_4$  crystals associated with the red (600nm) luminescence. In Ref. [50, 51] this luminescence is associated with a centre which is caused by the incorporation of the  $\text{Pb}^{3+}$  centre in  $\text{PbWO}_4$  crystals. The trivalent lead ion is stabilized in  $\text{PbWO}_4$  crystals by a Frenkel defect (the oxygen ion is shifted to an inter-site position with simultaneous creation of  $V_O$ ) [52]. Owing to the structure of the valence band the  $\text{Pb}^{3+}$  -ion does not create a localized hole-type centre. The Frenkel defect in turn lowers the local symmetry of the created  $\text{WO}_3$  tungsten complex towards a  $C_3$ , local symmetry or even lower, thus creating the shift and splitting of the original excited energy terms. Such a distorted tungsten anionic complex is responsible for the red luminescence in  $\text{PbWO}_4$  crystals.

## References

- [1] M.Nikl, presented at the CCC meeting, May 1995, CERN, W. Van Loo, Phys. Stat. Sol. a. 27, 1979, 565, W. Van Loo, Phys. Stat. Sol. a. 28, 1979, 227.
- [2] J.A. Groenink and G. Blasse, J. Sol. Stat. Chem. 32,1980, 9.
- [3] P. Lecoq, I. Dafinei, E. Auffray, M. Schneegans, V. Korzhik, O.V. Missevitch, V.B. Pavlenko, A.A. Fedorov, A.N. Annenkov, V.L. Kostylev, Nucl. Instrum. Meth.A 365, 1995, 291.
- [4] Y. Zhang, N.A.W. Holzwarth, R.T. Williams, Phys. Rev. B 57, 1998, 12738–12750.
- [5] M.J. Treadaway, R.C. Powell, J. Chem. Phys. 61, 1974, 4003–4011.
- [6] Y. Toyozawa, M. Inoue, J. Phys. Soc. Jpn. 21, 1966, 1663.
- [7] M. Nikl, P. Bohacek, E. Mihokove, M. Kobayashi, M. Ishii, Y. Usuki, V. Babin, A. Stolovich, S. Zazubovich, M. Bacci, J. Lumin. 87–89, 2000, 1136.
- [8] M. Nikl, Phys. Status Solidi A 178, 2000, 595.
- [9] J. A. Groenink and G. Blasse, Journal of solid state chemistry, 32, 1980, 9-20.
- [10] P. Lecoq, I. Dafinei, E. Auffray, M. Schneegans, M.V. Korzhik, O.V. Missevitch, V.B. Pavlenko, A.A. Fedorov, A.N. Annenkov, V.L. Kostylev, V.D. Ligun, Nucl. Instr. and Meth. A 365,1995, 291.
- [11] M.V. Korzhik, V.B. Pavlenko, T.N. Timoschenko, V.A. Katchanov, A.V. Singovskii, A.N. Annenkov, V.A. Ligun, I.M. Solskii, J.-P. Peigneux, Phys. Status Solidi A, 154, 1996, 779.
- [12] A. Annenkov, E. Auffray, M. Korzhik, P. Lecoq, J.-P. Peigneux, Phys. Status Solidi A, 1998,170.
- [13] M.V. Korzhik, Zh. Prikl. Spekt. 61,1994, 83.
- [14] J.A. Groenink, G. Blasse, J. Solidi State Chem. 32, 1980,9.
- [15] M.V. Korzhik, V.B. Pavlenko, T.N. Timoschenko, V.A. Katchanov, A.V. Singovskii,

- A.N. Annenkov, V.A. Ligun, I.M. Solskii, J.-P. Peigneux, *Phys. Status Solidi A* 154, 1996, 779.
- [16] A. Annenkov, E. Auffray, M. Korzhik, P. Lecoq, J.-P. Peigneux, *Phys. Status Solidi A* 170, 1998, 47.
- [17] M.V. Korzhik, V.B. Pavlenko, T.N. Timoschenko, V.A. Katchanov, A.V. Singovskii, A.N. Annenkov, V.A. Ligun, I.M. Solskii, J.-P. Peigneux, *Phys. Status Solidi A* 154, 1996, 779.
- [18] M.V. Korzhik, *Zh. Prikl. Spekr.* 61, 1994, 83.
- [19] M. Itoh, M. Fujita, *Phys. Rev. B* 62, 2000, 12825.
- [20] M. Itoh, D.L. Alov, M. Fujita, *J. Lumin.* 87–89, 2000, 1243.
- [21] D.L. Alov, N.V. Klassen, N.N. Kolesnikov, S.Z. Shmurak, in: P. Dorenbos, C.W.E. van Eijk (Eds.), *Proceedings of the International Conference on Inorganic Scintillators and their Applications*, Delft University Press, The Netherlands, 1996, p. 267.
- [22] D.L. Alov, S.I. Rybchenco, *Mater. Sci. Forum* 239–241, 1997, 279.
- [23] A.A. Annenkov, M.V. Korzhik, P. Lecoq, *Nucl. Instr. and Meth. A* 490, 2002, 30.
- [24] M. Kobayashi, M. Ishii, K. Harada, Y. Usuki, H. Okuno, H. Shimizu, T. Yazawa, *Nucl. Instr. and Meth. A* 373, 1996, 333.
- [25] R.Y. Zhu, D.A. Ma, H.B. Newman, C.L. Woody, J.A. Kierstead, S.P. Stoll, P.W. Levy, *Nucl. Instr. and Meth. A* 376, 1996, 319.
- [26] M. Bořhm, A.E. Borisevich, G.Yu. Drobychev, A. Hofstaetter, O.V. Kondratiev, M.V. Korzhik, M. Luh, B.K. Meyer, J.-P. Peigneux, A. Scharmann, *Phys. Status Solidi A* 167, 1998, 243.
- [27] A. Hofstaetter, R. Oeder, A. Scharmann, D. Schwabe, B. Vitt, *Phys. Status Solidi B* 89, 1978, 375.
- [28] J.M. Moreau, R.E. Gladyshevskii, Ph. Galez, J.P. Peigneux, M.V. Korzhik, *J. Alloys*

- Compounds 284, 1999, 104.
- [29] M.V. Korzhik, Delft University Press, Delft The Netherlands, 1996, p. 241.
- [30] C. Shi, Y. Wei, X. Yang, D. Zhou, C. Guo, J. Liao, H. Tang, Chem. Phys. Lett. 328, 2000, 1.
- [31] L. Sun, Q. Guo, X. Wu, S. Luo, W. Pan, K. Huang, J. Lu, L. Ren, M. Cao, C. Hu, J. Phys. Chem. C 111, 2007, 532
- [32] D.Tawde,M.Srinivas & K.V.R.Murthy, physics status solidi a, Vol.208, Issue 4, 2011, 803- 807.
- [33] A. Changhua, T. Kaibin, S. Guozhen, W. Chunrui, and Q. Yitai, Mater. Lett. 57, 2002, 565.
- [34] W.Van Loo, Phys. Status Solidi A 27, 1975, 565.
- [35] Biao Liu, Shu-Hong Yu, Linjie Li, Qiao Zhang, Fen Zhang, and Ke Jiang, Angew. Chem., 116, 2004, 4849-4854.
- [36] M. Nikl, V. V. Laguta, and A. Vedda, Phys. Status Solidi B 245, 2008, 1701.
- [37] A. Annenkov, E. Auffray, M. Korzhik, P. Lecoq, and J.-P. Peigneux, Phys. Status Solidi A 170, 47 (1998).
- [38] M. Itoh, D. L. Alov, and M. Fujita, J. Lumin., 87, 2000, 1243.
- [39] Changhua An, Materials Letters 57, 2002, 565- 568.
- [40] M. Nikl, P. Bohacek, E. Mihokove, M. Kobayashi, M. Ishii, Y. Usuki, V. Babin, A. Stolovich, S. Zazubovich, M. Bacci, J. Lumin. 87–89 , 2000, 1136.
- [41] Y. Zhang, N. A. W. Holzwarth, and R. T. Williams, Phys. Rev. B 57, 1998, 12738.
- [42] M. Bacci, S. Porcinai, E. Mihóková, M. Nikl, and K. Polák, Phys. Rev. B 64, 2001, 104302.
- [43] Y. Zhang, N. A. W. Holzwarth, and R. T. Williams, Phys. Rev. B 57, 1998,12738.
- [44] G. Blasse, Struct. Bonding ,Berlin, 42, 1980, 1.

- [45] M. Itoh and T. Sakurai, *Physical Review B* 73, 2006, 235106.
- [46] M. J. J. Lammers, G. Blasse, and D. S. Robertson, *Phys. Status Solidi A* 63, 1981, 569.
- [47] V. B. Mikhailik, H. Kraus, D. Wahl, M. Itoh, M. Koike, and I. K. Bailiff, *Phys. Rev. B* 69, 2004, 205110.
- [48] Yanlin Huang, Xiqi Feng, Wenliang Zhu, Zhenyong Man, *Journal of Crystal Growth* 250, 2003, 431–436.
- [49] Belsky, A. N.; Mikhailin, V. V.; Vasil'ev, A. N.; Dafinei, I.; Lecoq, P.; Pedrini, C.; Chevallier, P.; Dhez, P.; Martin, P. *Chem. Phys. Lett.* 243, 1995, 552.
- [50] P. Lecoq, I. Dafinei, E. Auffray, M. Sneegans, M.V. Korzhik, O.V. Missevitch, V.B. Pavlenko, A.A. Fedorov, A.A. Annenkov, V.L. Kostilev, V.D. Liogun, *Nucl. Instr. and Meth. A* 365 (1995) 291.
- [51] A.A. Annenkov, A.A. Fedorov, Ph. Galez, V.A. Kachanov, M.V. Korzhik, V.B. Pavlenko, V.A. Ligun, T.N. Timochenko, J.-P. Peigneux, B.A. Zadneprovski, *Phys. Stat. Sol. A* 156 (1996) 493.
- [52] A. Fedorov, M. Korzhik, O. Missevitch, et al., *Radiat. Meas.* 26, 1996, 107.

## Summary & Conclusions

Recent development in nanotechnology requires  $\text{PbWO}_4$  material having different morphologies and dimensions suitable for nano dimensional devices. So it is important to study effect of different reaction parameters (Precursor, pH, Concentration, Time and Temperature) on morphology of the final product.

We have prepared undoped as well as Cerium doped  $\text{PbWO}_4$  phosphor with various morphologies using facile Low Temperature Hydrothermal method. Self-designed Teflon Lined Stainless Steel Autoclave having 90 ml capacity was used to prepare all samples. We have divided our experiment into *two parts* to do systematic analysis of structural and optical properties of undoped and Cerium doped Lead Tungstate ( $\text{PbWO}_4$ ) phosphor. In the first part of our experiment undoped as well as Cerium doped  $\text{PbWO}_4$  phosphor were synthesized with different Lead sources (Lead Acetate, Lead Nitrate and Lead Chloride),  $\text{Na}_2\text{WO}_4$  as a metallic cation and distilled water as solvent. In the second part of our experiment  $\text{PbCl}_2$  was kept constant as a Lead source and phosphor were synthesized by varying reaction temperatures and pH of solution. Crystal structure, phase and morphology were characterized by X-ray Diffraction (XRD) Analysis Technique, Scanning Electron Microscopy (SEM), Transmission Electron Microscopy (TEM) and Photoluminescence. Lattice parameters, unit cell volume and average crystallite size were performed with PowderX program.

### Effect of Lead Sources

X-ray spectra of  $\text{PbWO}_4$  and  $\text{PbWO}_4$ : Ce synthesized  $100^\circ\text{C}$  temperature with different Lead sources are polycrystalline in nature and contain mixture of two phases

i.e. stolzite and raspite phase of  $\text{PbWO}_4$ . All X-ray diffraction peaks were indexed to a tetragonal stolzite phase with space group  $I4_1/a$  and monoclinic raspite phase with space group  $P2_1/a$ . The highest relative intensity is obtained for (112) crystallographic plane of tetragonal crystal structure. At  $100^\circ\text{C}$  temperature raspite phase is produced predominantly and with increase in temperature it transforms irreversibly into stolzite phase. Using  $\text{Pb}(\text{CH}_3\text{COO})_2$  as a lead source, large amount of raspite phase was produced compared to  $\text{Pb}(\text{NO}_3)_2$  and  $\text{PbCl}_2$ .  $\text{PbWO}_4$  prepared with Lead Chloride showed highest crystallinity and contained least amount of raspite phase inclusions. Hence *Lead Chloride proved to be better Lead source to produce high crystalline  $\text{PbWO}_4$  crystals over Lead nitrate and Lead acetate.* Range of unit cell volume for stolzite phase is  $359.47\text{-}383.83 \text{ (\AA)}^3$  and that is for raspite phase is  $359.09\text{-}375.32 \text{ (\AA)}^3$ . It is observed in our analysis that volume of unit cell of tetragonal and monoclinic structures are very close to each other; the difference is less than 0.53%. The average crystallite sizes were estimated by the Scherrer's equation using the Full Width at Half Maximum (FWHM) from the most intense peak (1 1 2).

The effect of different Lead sources on the morphology of  $\text{PbWO}_4$  was investigated from TEM and SEM characterization. Many interesting morphologies were produced in our experiments without the use of expensive template or surface directing capping agents. When  $\text{Pb}(\text{CH}_3\text{COO})_2$  was used as the lead source, product with mixture of two phases (stolzite and raspite) were produced.  $\text{PbWO}_4$  prepared with Lead Acetate possesses mixed morphologies of single branched dendrite around  $5\mu\text{m}$  long and tetrahedron microparticles are about  $500 \text{ nm}$  in size. When  $\text{Pb}(\text{NO}_3)_2$  was used as the Lead source, six branched dendrite ( $2.10 \mu\text{m} \times 1.18 \mu\text{m}$ ) and rhombic shaped particle and flat nanobelt ( $5\mu\text{m} \times 1\mu\text{m}$ ) were produced. When  $\text{PbCl}_2$  was used as the Lead source, octahedron shaped microparticles of having size around  $100 \text{ nm}$

were produced and flat nanobelts having width 100-150nm and about few  $\mu\text{m}$  in length were obtained due. We assumed that dendrite, tetrahedron, rhombic and octahedron shaped microparticles are possesses stolzite phase of  $\text{PbWO}_4$ . Similarly nanobelts are possesses raspite phase of  $\text{PbWO}_4$ . As soon as both reactants mixed in supersaturated aqueous solution nanoparticles of  $\text{PbWO}_4$  were formed. Nanoparticles were assembled to form nanorod and nanoflake like structure when such mixture was treated in the autoclave for shorter duration of time. If we increase the reaction time for (12 h), rhombic shaped microparticles were produced which turns into single or multiple branched dendrite or flat microbelts. We can also conclude that at lower temperature raspite phase is produced and with increases in temperature raspite phase turns into stolzite phase. In general, *two phases of  $\text{PbWO}_4$  (stolzite and raspite) are produced irrespective of Lead sources at low temperature ( $100^\circ\text{C}$ ) and both phases produced have different morphologies in micrometer range.* The formation various morphologies of  $\text{PbWO}_4$  is attributed to favourable thermo-dynamic conditions. The formation and evolution processes can be divided into three steps: initial nucleation process in supersaturated solution, self-assembly process (oriented aggregation), and subsequent crystal growth process (Ostwald ripening).

Photoluminescence spectra of  $\text{PbWO}_4$  were investigated at room temperature using a 305-nm excitation wavelength. PL emission spectra of  $\text{PbWO}_4$  consists two components, a fast blue component around 450 nm which is an intrinsic feature of stolzite phase and a slow green one around 480-520 nm which is an intrinsic feature of raspite phase. A broad blue luminescence peak around 450 nm originates from tetragonal  $\text{WO}_4^{2-}$  groups. The dendrite with six branched structure, rhombic shaped nanoparticles and nanobelt have highest surface to volume ratio compared to single branched dendrite and tetrahedron microparticles, hence they

contain higher concentration of surface related defects (particularly oxygen vacancies) which enhance PL emission of  $\text{PbWO}_4$  prepared with Lead Nitrate compared to  $\text{PbWO}_4$  prepared with Lead Acetate. Photoluminescence spectra of  $\text{PbWO}_4$  prepared with Lead Chloride shows higher intensity compared to Lead Acetate and Lead Nitrate. The shape of PL spectra of  $\text{PbWO}_4$  synthesised using  $\text{PbCl}_2$  has “*spread-eagle-shape*” with a central peak surrounded by two broad shoulder peaks. Emission spectrum reveals that it is composed of several sub-bands which are almost distributed throughout entire 350-550 nm region. We proposed that the Gaussian peak I (367 nm), the Gaussian peak II (392 nm) and the Gaussian peak III (452 nm) may correspond to the radiative transitions from  ${}^3\text{A}_1 \rightarrow {}^1\text{A}_1$ ,  ${}^3\text{A}_2 \cong {}^3\text{E} \rightarrow {}^1\text{A}_1$  and  ${}^3\text{A}_2 \rightarrow {}^1\text{A}_1$ , respectively. Hence *blue emission occurs from the lower lying triplet state split by Jahn-Teller interaction. The peak position of all the three blue Gaussian components in PL spectra recorded at room temperature is shifted towards the short wavelength side compared to those reported at lower temperatures.*

### Effect of Cerium doping on $\text{PbWO}_4$

XRD reflection spectra confirm that Cerium doping in  $\text{PbWO}_4$  does not distort its characteristic shape. *Cerium doping in  $\text{PbWO}_4$  prepared with different Lead sources does not change the crystal structure or induce a new phase.* Cerium doping reduces lattice parameters of all  $\text{PbWO}_4$  samples prepared with different Lead sources.  $\text{Ce}^{3+}$  substitute well  $\text{Pb}^{2+}$  in  $\text{PbWO}_4$  lattice and induce  $\text{Pb}^{2+}$  vacancy in order to keep the charge neutral. The  $\text{Ce}^{3+}$  ions are likely to enter  $\text{PbWO}_4$  crystal lattice to substitute  $\text{Pb}^{2+}$  sites considering that the ion radius of  $\text{Ce}^{3+}$  (0.103 nm) is similar to that of  $\text{Pb}^{2+}$  (0.120 nm). Cerium suppresses the intensity of XRD peaks representing raspite phase. Hence we conclude that *Cerium act as catalyst and helps raspite phase to convert into*

*stolzite phase when Lead Chloride was used as Lead source.* Effect of  $\text{Ce}^{3+}$  doping on crystal structure of  $\text{PbWO}_4$  at different temperatures is not reported till date and first time we have done this type of study. It is also inferred from the XRD spectra that with Cerium doping, intensity of peaks representing raspite phase decreases and intensity of peaks representing stolzite phase increases. This behaviour is observed in all the samples for all the temperatures. Thus we can conclude that along with temperature, cerium also plays an important role to decrease the amount of raspite phase and increase the amount of stolzite phase with increase in temperature. The cell parameters, unit cell volume and average crystallite size of Cerium doped  $\text{PbWO}_4$  crystals at  $100^\circ\text{C}$ ,  $150^\circ\text{C}$  and  $200^\circ\text{C}$  temperatures were investigated. It is found that lattice parameters and unit cell volume decreased with doping of Cerium at all temperatures. *Cerium increases the average crystallite size for more than 50% at all temperatures.*

Cerium doping in  $\text{PbWO}_4$  synthesized with Lead Acetate changes morphology to nanobelts ( $5\mu\text{m} \times 1\mu\text{m}$ ) having bamboo-leaf- like morphology. Growth mechanism of  $\text{PbWO}_4$  microbelt explained. Cerium will not play any direct role in the production of belt like structure. These nanobelts are produced at comparatively low ( $100^\circ\text{C}$ ) temperatures for short (12h) reaction time at 7pH. It shows that  *$\text{PbWO}_4$  nanobelts can be produced at lower temperature without using any surfactant/capping agent or composite salt by hydrothermal method.* Preparation of Cerium doped  $\text{PbWO}_4$  using Lead Nitrate as a Lead source is not reported yet by any other method except us with hydrothermal method. Cerium doping in  $\text{PbWO}_4$  synthesized with Lead Nitrate as well as Lead Chloride produces tetrahedron shaped  $\text{PbWO}_4$  nanoparticles having 100nm in size. Cerium doping in  $\text{PbWO}_4$ , tetrahedron shaped microparticles with stolzite phase is dominantly produced over raspite phase.

Thus Cerium plays an important role in controlling the morphology of  $\text{PbWO}_4$  prepared with Lead Nitrate and Lead Chloride. So we proposed that *Cerium plays the role of surfactant or capping agent by regulating crystal growth direction. This is a very interesting phenomenon and it should be investigated for other types of rare earth elements also.*

The intensity of PL is suppressed to a great extent by doping with cerium. The cerium doped  $\text{PbWO}_4$  shows weaker luminescence intensity than that of undoped  $\text{PbWO}_4$ . Green emission of  $\text{PbWO}_4:\text{Ce}$  prepared with Lead Acetate is more compared to  $\text{PbWO}_4:\text{Ce}$  prepared with Lead Nitrate which is assumed to related with respite inclusions. Photoluminescence emission spectra shows structured character for both undoped and cerium doped samples. Such type of structural shape invokes presence of four Gaussian components: three peaks fall in blue region and one in green region. The presence of four Gaussian components indicates the excited states of emission center are relaxed and degenerated under the influence by perturbation. According to Kobayashi et al. Cerium doping in  $\text{PbWO}_4$  results low energy shift of absorption spectra due to  $4f \rightarrow 5d$  transitions and hence emission spectra should also shift to lower energy side due to Stokes shift. Similar type of red shift is observed in position of Gaussian peak IV in our case. Furthermore, decrease of light yield (LY) for  $\text{PWO}:\text{Ce}$  sample by a factor 2–3 was observed with respect to undoped PWO. The absence of intrinsic  $\text{Ce}^{3+}$  emission at the room temperature and observed lower Light Yield can be explained by a non-radiative  $5d \rightarrow 4f$  transition to the ground state of excited  $\text{Ce}^{3+}$  ions, i.e.  $\text{Ce}^{3+}$  ions can serve as efficient non-radiative traps in the PWO matrix. Such a conclusion support the observed faster PL decay of  $\text{PWO}:\text{Ce}$  at room temperature (RT) with respect to the undoped sample, which can be explained by

selective suppression of the delayed recombination process due to non-radiative recombination of free electrons and holes at the  $\text{Ce}^{3+}$  sites.

### Effect of pH of reaction solution on $\text{PbWO}_4$

To study the effect of pH of solvent on structural and optical properties of  $\text{PbWO}_4$ , three samples were selected which are prepared at 3pH, 7pH and 11pH.  $\text{PbWO}_4$  synthesized at different pH of reaction solution are single phase. X-ray diffraction analysis of these samples shows that all three samples are highly crystallized and completely indexed to a pure tetragonal stolzite phase of  $\text{PbWO}_4$  with space group  $I4_1/a$ . This result shows that the *different pH promotes the formation of crystalline  $\text{PbWO}_4$  powders at low synthesis temperature and reduced processing time than the other conventional methods.*

In order to analyze morphology of these samples with TEM, two samples (samples prepared at 7pH and 11pH) were chosen based on their excellent photoluminescence spectra.  $\text{PbWO}_4$  prepared at 7pH and 11pH show better crystallization than the one made at 3pH. Our result shows that  *$\text{PbWO}_4$  nanomaterials with good crystallinity can be formed even at 11pH and optimal pH range for  $\text{PbWO}_4$  is 3-11 pH.* TEM images shows that Quasi-spherical hollow nanoparticles (HNPs) with an average diameter of about 20-40 nm and hollow nanotubes (HNTs) having outer diameter approximately 12.37 nm and length around 80-170 nm were produced at 7 pH. Upon rising pH to 11, solid nanorods were produced with increased length from 80-170 nm to 2 $\mu\text{m}$  with 40 nm outer diameter. Formation of hollow nanoparticles (HNPs) and hollow nanotubes (HNTs) explained on the basis of Kirkendall counter diffusion effect. *Formation of  $\text{PbWO}_4$  Hollow Nano Tubes (HNTs) have not been reported yet, hence we are first to synthesis it. XRD and TEM analysis*

*shows that in the 7-11pH range highly crystallized 1-Dimensional PbWO<sub>4</sub> nanorods with pure stolzite phase obtained.* From the present work, it is found that the pH value of reaction system has great influence on the morphologies of the obtained samples, when the other conditions were the same. Regarding to the formation mechanism of the PbWO<sub>4</sub> nanorods through hydrothermal approach, it is clear that the growth process is not surfactant-assisted or template-directed, because no surfactants or templates are introduced into the reaction system. It can be noted from our result that *with increase in pH, size of PbWO<sub>4</sub> nanoparticles and length of the PbWO<sub>4</sub> increases and morphology changes from HNTs to nanorods.*

In order to study the effect of pH of the reaction solution on luminescence property, PL spectra of PbWO<sub>4</sub> synthesized at different pH was recorded at two excitation wavelengths 300 nm and 254 nm. PbWO<sub>4</sub> shows “spread-eagle-shaped” broad luminescent emissions in blue and green range. PbWO<sub>4</sub> (Nanoparticles and HNTs) obtained at 7pH, display a strong emission peak cantered at about 485 nm at room temperature. However, the absolute luminescence intensity increased with increasing pH, over the range of 3-7 pH, implying that the hollow nanoparticles (HNPs) and hollow nanotubes (HNTs) had much improved luminescence intensity. Very weak PL intensity of the sample obtained for 3pH due to poor crystallinity. Obtained PL spectra was fitted with four individual Gaussian peaks having peaks position for peak I (365 nm), peak II (395 nm), peak III (459 nm) and peak IV (500nm). Gaussian peak I, the Gaussian peak II and the Gaussian peak III may correspond to the radiative transitions from  $^3A_1 \rightarrow ^1A_1$ ,  $^3A_2 \cong ^3E \rightarrow ^1A_1$  and  $^3A_2 \rightarrow ^1A_1$ , respectively. The Gaussian peak IV ascribed to oxygen deficient irregular WO<sub>3</sub> neutral molecule. The PL intensity of blue and green emission peak is highest for sample prepared at 7pH (HNTs), it is intermediate for sample prepared at 11pH

(Nanorods) and lowest for sample prepared at 3pH which indicates that  $PbWO_4$  HNTs have more regular lattice structure, uniform morphology and highest defect centres relative to oxygen (due to faster 1-D crystal growth) compared to Nanorods. Sample prepared at 3pH has lowest regular lattice structure and lowest defect centres relative to oxygen.

### Effect of synthesis Temperature on $PbWO_4$

In order to study the effect of reaction temperature samples synthesized at four different temperatures: 100°C, 125°C, 150°C and 200°C were selected.  $PbWO_4$  prepared at 100°C temperature contains highest amount of raspite phase compared to those prepared at 150°C and 200°C temperatures. With increase in temperature from 100°C to 200°C percentage of raspite phase of  $PbWO_4$  decreases. Among all samples, pure stolzite phase produced only at 125°C with highest crystallinity. However, on comparing the XRD peaks of the products, we found that the relative intensity of the peaks varied significantly, indicate that at different temperature  $PbWO_4$  with different crystallinity forms. Thus different reaction temperature in our experiment would bring about significant changes in the crystallization of stolzite phase of  $PbWO_4$ . Lattice parameter (a, b) is highest for sample prepared at 100 °C which decreases with increase in temperature up to 150 °C and again increase for sample prepared at 200°C. While lattice parameter (c) remains constant for sample prepared at 100 °C to 125 °C and increase and become maximum for 150 °C then again decrease for sample prepared at 200°C. Unit cell volume is highest for sample prepared at 100 °C which decreases with increase in temperature up to 125 °C and again increase for sample prepared at 150°C. Unit cell volume then remains constant up to 200 °C. While

average crystallite size is highest for sample prepared 125 °C and decrease for 150 °C then again increase for sample prepared at 200°C. From our results we can conclude that *unit cell volume is inversely proportional to average crystallite size.*

To investigate the effect of temperature on morphology of undoped PbWO<sub>4</sub>, TEM images of samples prepared at two different reaction temperatures i.e 100°C and 125°C were selected. TEM photographs of product obtained at 100°C temperature shows mixture of microparticles of octahedral shape having size around 100 nm as well as aggregation of nanoflakes like structure having width 100-150nm and about few μm in length. When the temperature rose to 125 °C, Quasi-spherical hollow nanoparticles (HNPs) having average diameter of about 20-40 nm and Hollow Nano Tubes (HNTs) having outer diameter 12.37 nm and around 80-170 nm in length with uniform and smooth surface were obtained. These HNPs and HNTs are highly crystalline compared to product obtained at 100 °C. Octahedraon microparticles and nanoflakes obtained at 100°C contains mix phases of stolzite and raspite structures, while Hollow nanoparticles and HNTs produced at 125 °C are of pure stolzite phase with high crystallinity. *Comparison of these products shows that at low temperature (around 100 °C), PbWO<sub>4</sub> microstructures containing mix morphologies influenced by raspite as well as stolzite phase will obtained. As we go from low temperature to high temperature raspite phase is diminished and nanostructures with lower dimensions having pure stolzite phase is obtained.*

Room temperature photoluminescence spectra of PbWO<sub>4</sub> nanophosphor prepared at different temperatures (100°C, 125°C and 200°C) were recorded with 254 nm and 300 nm excitation wavelengths. It is well known that PL intensity has direct relation with crystallinity. The better crystallinity, the higher PL emission peak is. Hence among all three samples (HNTs) of PbWO<sub>4</sub> prepared at 125 °C shows strong

green luminescence due to its highest crystallinity while (microparticle + microplates) of  $\text{PbWO}_4$  prepared at  $100^\circ\text{C}$  shows weak luminescence due to poor crystallinity. Higher crystallinity of Quasi-spherical nanoparticles and Hollow Nano Tubes are main reason to produce high PL intensity compared to low crystalline microparticles and flake like inclusions. It implied that *PbWO<sub>4</sub> nanostructure have a better luminescence intensity then microstructure at room temperature. Higher intensity of blue emission at low temperature* shows that samples prepared at low temperature has higher concentration of  $\text{WO}_4^{2-}$ . At higher reaction temperature lattice regularity breaks and also decreases the concentration of blue emission center. Enhancement of Green emission of the sample prepared at  $125^\circ\text{C}$  is due to presence of larger amount of surface defect is also discussed.

## Up Conversion emission

Up-conversion emission was observed in undoped  $\text{PbWO}_4$  synthesized with different pH and temperatures excited with 625 nm wavelength, respectively. Intensity of up-conversion luminescence is highest for  $\text{PbWO}_4$  sample prepared at 7pH or  $125^\circ\text{C}$ , intermediate for 11pH and lowest for 3pH. Up-conversion luminescence intensity is also least for sample prepared at  $100^\circ\text{C}$  and  $200^\circ\text{C}$ .

Large single crystals of  $\text{PbWO}_4$  are produced either via Czochralski or Bridgman method which require highly expensive and specially designed equipments. These methods produce  $\text{PbO}$  and  $\text{WO}_3$  harmful gases during crystal growth due to higher synthesis temperature (i.e.  $1125^\circ\text{C}$ ). Products obtained by these methods are in bulk size which cannot be used for devices based on nano dimensions. These limitations lower the applicability of these methods for large scale production of  $\text{PbWO}_4$  crystals. Shortcomings of high temperature synthesis techniques such as:

inhomogeneity, production of harmful gases, impurity contamination and powders with different sizes and non-uniform distribution of  $\text{PbWO}_4$  can be resolved by Low temperature Hydrothermal method. Thus *Hydrothermal process is proved to be effective, facile and green route for the synthesis of  $\text{PbWO}_4$  nanostructures having low-cost, high efficiency and good potential for high-quantity production.* Unlike many advanced methods that can prepare a large variety of forms, the respective costs for instrumentation, energy and precursors are far less for Hydrothermal method. *Lead Tungstates synthesized at room temperature by Hydrothermal method do not contain Schottky defects usually present in similar materials prepared at high temperatures which results in improved luminescent properties.* This facile method does not need any seed, catalyst, harmful and expensive surfactant or template thus it is promising for large-scale and low-cost production with high-quality  $\text{PbWO}_4$  nanophosphor with various morphologies.

## Applications

On passing current through low-pressure Hg discharge, UV light having wavelength 254 nm is generated. This light is invisible and harmful and has to be converted into visible light. This can be done by the application of  $\text{PbWO}_4$  spherical hollow nanoparticles (HNPs) which are produced at 125°C temperature because they show strong absorption at 254 nm and convert this into visible light very efficiently. Cerium doped  $\text{PbWO}_4$  can be used for *green emitting Lamp phosphor*. The application of Oxidic inorganic nano particles doped by lanthanides is thus an Interesting alternative to the use of organic fluorophores and quantum dots for many application areas, e.g., in medical diagnostics, in biological sensors, and in fluorescence marking of biological probes for high throughput screening. Hollow Nano tubes of  $\text{PbWO}_4$  can be

used or *nano fluidic application* in biomedical science. Early up-conversion lasers were demonstrated with bulk crystals, which often had to be cooled to very low temperatures, making the systems impractical. Nowadays, most *up-conversion lasers* are based on nano fibers, where high pump intensities can be maintained over long lengths, so that the laser threshold can be reached even under otherwise difficult conditions. 1-dimensional HNTs shows strong up-conversion at 625 nm wavelength which can be used for such application. Though our assumptions are primitive further research required for practical application of  $\text{PbWO}_4$  nano phosphor in above proposed areas.

### **Future Work**

Our future planning is to prepare  $\text{PbWO}_4$  using  $\text{PbCl}_2$  with different Cerium concentration and do optimization of its Photoluminescence intensity.

## RESEARCH OUTPUT

### In Journals

1. *Effect of Lead source and Cerium(III) doping on structural and photoluminescence properties of PbWO<sub>4</sub> microcrystallites synthesized by hydrothermal method*,  
**D. Tawde**, M. Srinivas and K. V. R. Murthy, Phys. Status Solidi A, Vol.208, Issue 4, page 803- 807, 2011.
2. *Effect of Temperature and Doping of Cerium on PbWO<sub>4</sub> nano Phosphor*,  
**D.Tawde**, Dhaval Modi, M.Srinivas and K.V.R. Murthy, manuscript accepted to be published in International Journal of Luminescence and its Applications, 2012.

### In Conference Proceedings

1. *Optical and Structural characterization of rare earth doped PbWO<sub>4</sub> nanocrystallites*,  
**D.Tawde**, Dhaval Modi, M.Srinivas, K.V.R.Murthy, Proceedings of 1<sup>st</sup> National Conference On Recent Trends of Physics in Technology & Life Sciences August 19, 2011, Indore
2. *Hydrothermal preparation and Photoluminescence of bundle-like structure of CdWO<sub>4</sub> nanorods*,  
Dhaval Modi, **D. Tawde** and M. Srinivas, UGC Sponsored Seminar on Current Trend in Physics and its Applications, 5Jan, 2011, Dabhoi.
3. *Structural , Dielectric and Optical characterization of Pb<sub>0.3</sub>(Zn<sub>0.35</sub>W<sub>0.35</sub>)O<sub>3</sub>*  
Dhaval Modi, **D. Tawde** and M. Srinivas, 54<sup>rd</sup> Proceeding of DAE-SSPS, 869-870(2009), The M.S.University of Baroda.
4. *Structural and Optical study of PbWO<sub>4</sub> nano crystals prepared by Micro-emulsion Hydrothermal method*  
**D.Tawde**, M. Srinivas and Sunil Shah, 54<sup>rd</sup> Proceeding of DAE-SSPS,337-338 (2009), The M.S.University of Baroda.
5. *Photoluminescence of PbWO<sub>4</sub> Nanocrystallites Using Hydrothermal Preparation*.  
**D. Tawde** and M. Srinivas, Proceedings of the National Conference on Luminescence and its Application, 24-25 (2009), Kolkata.
6. *Structural , Optical and Dielectric properties of (Pb,Sr)WO<sub>3</sub>*,  
**D.Tawde** and M.Srinivas, 53<sup>rd</sup> Proceeding of DAE-SSPS, 211-212(2008) at BARC.